UNIVERSITY OF CALIFORNIA

Los Angeles

Search for Rare Decays of the B Meson at 1.8 TeV pp̄ Collisions at CDF

A dissertation submitted in partial satisfaction of the

requirements for the degree Doctor of Philosophy

in Physics

by

Carol E. Anway-Wiese

1995

The dissertation of Carol E. Anway-Wiese is approved.

D. Buchanan

D. Cline

J. Hauser

E. Hoffman

T. Müller, Committee Chair

University of California, Los Angeles

1995

█████████████████

████████████████████████

Contents

List of Figures

List of Tables

ACKNOWLEDGEMENTS

███████████   ███████████

1986   Elected to Phi Beta Kappa

1987   B. A., Physics and Mathematics
                                   Hamline University
                                   St. Paul, Minnesota

1989   M. S., Physics
                                   University of California, Los Angeles
                                   Los Angeles, California

PUBLICATIONS AND PRESENTATIONS

C. Anway *et al.*, The SDC Collaboration. GEANT simulations with shell and module geometry code and scintillating fiber central tracking. SDC-91-00073, (1991). Fermilab Library Only.

C. Anway-Wiese. Offline muon matching cuts. Technical Report CDF/ANAL/MUON/CDFR/1986, Fermilab, (1993).

C. Anway-Wiese. Calculating branching ratio limits when comparing related decay modes. Technical Report CDF/ANAL/BOTTOM/CDFR/2496, Fermilab, (1994).

C. Anway-Wiese. Rare B decays. Technical Report CDF/ANAL/BOTTOM/CDFR/2701, Fermilab, (1994).

C. Anway-Wiese *et al.*, The CDF Collaboration. Limit on the rare decay $B \rightarrow \mu^+\mu^- K^\pm$. FERMILAB-CONF-94-145-E, (1994). Presented at 27th International Conference on High Energy Physics (ICHEP), Glasgow, Scotland, 20-27 July 1994.

C. Anway-Wiese *et al.*, The CDF Collaboration. Rare B decays $B \rightarrow \mu^+\mu^- K^{\pm}$ and $B \rightarrow \mu^+\mu^- K^{*0}$. FERMILAB-CONF-94-210-E, (1994). Presented at Eighth Meeting of DPF of APS (DPF'94), University of New Mexico, Albuquerque, NM, 2-6 August, 1994.

C. Anway-Wiese *et al.*, The CDF Collaboration. Rare B decays $B \rightarrow \mu^+\mu^- K^{\pm}$ and $B \rightarrow \mu^+\mu^- K^{*0}$. FERMILAB-CONF-94-210-E, (1995). In *International Symposium on Vector Boson Self-Interactions*, University of California, Los Angeles, February 1-3, 1995.

ABSTRACT OF THE DISSERTATION

Search for Rare Decays of the B Meson at 1.8 TeV $p\bar{p}$ Collisions at CDF

by

Carol E. Anway-Wiese

Doctor of Philosophy in Physics

University of California, Los Angeles, 1995

Professor T. Müller, Chair

With the observation of a clear B hadron signal in the exclusive decay channels $B \to \psi K^{\pm}$ and $B \to \psi K^{*0}$ in 1.8 TeV $p\bar{p}$ collisions at CDF, it is feasible to look for the non-resonant decays $B \to \mu^+\mu^- K^{\pm}$ and $B \to \mu^+\mu^- K^{*0}$, which have not been seen. In the standard model these decay modes are very rare; higher rates would signal physics beyond our present understanding. This thesis reports on a search for flavor-changing neutral current decays of B mesons using data obtained in the Collider Detector at Fermilab (CDF) 1992-1993 data taking run. To reduce the amount of background in the data I use precise tracking information from the CDF silicon vertex detector to pinpoint the location of the decay vertex of the B candidate, and accept only events which have a large decay time. I compare this data to B meson signals obtained in a similar fashion, but where the muon pairs originate from ψ decays, and calculate the relative branching ratios. The relative branching ratio calcu-

lations cancel experimental and theoretical uncertainties. In the absence of any indication of flavor-changing neutral current decays, I set upper limits of $\text{BR}(B \to \mu^+\mu^- K^{\pm}) < 1.1 \times 10^{-5}$ and $\text{BR}(B \to \mu^+\mu^- K^{*0}) < 1.6 \times 10^{-5}$ at 90% confidence level, which are consistent with Standard Model expectations but leave little room for non-standard physics.

Chapter 1

Introduction

At Fermilab and many other accelerators around the world, particle physicists endeavor to study the most fundamental level of matter, a level at which matter and energy mix, and forces not normally encountered in everyday life are dominant. We see the universe through the framework of the standard model, the current most accurate theory of "the way things work." In this model, the familiar electrons are fundamental, but protons and neutrons are made up of three quarks each. Forces act on all particles in some way, so we can make these quarks come apart and recombine in different arrangements. We can also produce all six quarks in the standard model from the energy of collisions in facilities such as the collider at Fermilab. It is the properties of these forces and new particles that are particularly fascinating. Knowing how they interact with one another helps us define the concept of mass and stretch the limits of our knowledge.

The three parts of an experimental physicist's work are forces, particles and

detectors. Particles are the basic building blocks of matter, forces make the particles move, and detectors help us understand the process. Our knowledge is limited by the precision of our equipment. All three are required to extend our understanding.

1.1   Forces

There are four fundamental forces in nature: Gravity, Electromagnetism, the weak nuclear force and the strong nuclear force. Gravity causes stars to form and planets to rotate around them. Gravity limits our motion and causes weather. Though it is a long-range force, it is the weakest of the forces, weaker by far than the nuclear weak force. We experience the cumulative effects of the many many particles inside the earth acting together on our bodies. Suns affect planets because they are both composites of a huge number of small, massive particles. In the laboratory, elementary particle physicists work with the tiniest of all particles, so light that we ignore any effect of this great force.

Electromagnetism illuminates our lives with candles and bulbs; any sort of light is electromagnetic. It forms the basis for the chemical bonds which hold our bodies together. Plants, animals, even atoms couldn't exist without it. The same way gravity acts between objects which have mass, the electromagnetic force acts between particles which have electric charge. Unlike gravity, electric charge comes in two varieties, positive and negative charges. Massive particles are attracted to massive particles, but positively charged particles are attracted to negatively charged particles and repelled by posi-

tively charged particles. The electromagnetic force is also a long-range force; we can study stars and galaxies throughout the universe by examining their electromagnetic radiation.

Within its short range, the strong force is the strongest of all the forces. It acts between "colored" objects, the quarks. Instead of two electric charges, the particles which take part in the strong force may have one of three strong charges. These charges are called color, since that is another convenient and familiar three-fold symmetry. Quarks carry one color and gluons have a color and an anticolor. This strong force, which is always attractive, binds quarks together to make protons and neutrons. Furthermore, it binds the neutrons and protons together to make atomic nuclei. Without the strong force, we would not have the atoms with all their various valuable properties. Since we don't see colored objects occuring naturally (or in the laboratory either), all composites of quarks must be neutral, or white. Mesons have two quarks, one with color and one with anti-color. For example one red u quark plus one anti-red $\bar{d}$ quark make a π^+ meson. Baryons have three quarks, one of each color, red, yellow and blue.

The weak force fuels the sun with nuclear beta decay and allows us to perform carbon-14 dating. There isn't a name for the "weak charge," though some physicists claim that the charge is flavor (*e. g. s* quarks have strange flavor). However, the W isn't consistent in its conservation of flavor; leptonic decays conserve flavor but quark decays may not. Flavor is modified mathematically to account for this behaviour and there is no name for this new

"weak charge." The signature of the decay is that the weak force changes the fundamental quantum numbers of particles. That is, it changes one particle into another. The weak force is short-range. Without the weak force, there would be many more naturally occuring particles, all the lightest particles of each family. Instead, these particles change families in a weak decay and then decay to lighter members of the new family. The decays examined in this thesis are weak decays.

1.2 Particles

According to the standard model, there are six quarks, six leptons, their twelve corresponding antiparticles, plus twelve gauge bosons which cause interactions between the particles and antiparticles. The quarks and leptons are arranged in three families as follows, where the charge indicated is the electric charge of the particle relative to the charge of a proton.

Quarks:	u	c	t	charge = +2/3
	d	s	b	charge = -1/3
Leptons:	ν_e	ν_μ	ν_τ	charge = 0
	e	μ	τ	charge = -1

The masses of the quarks range from 5 MeV/c^2 to 176 GeV/c^2. Neutrinos are massless, but the other leptons have masses which range between 0.5 MeV/c^2 and 1.8 GeV/c^2. Neutrinos interact weakly. The other leptons interact

4

electromagnetically and weakly. Quarks interact strongly, electromagnetically and weakly.

Gauge bosons mediate the forces between the other particles. This important discovery has fueled the revolution in high energy physics in the last century. The electromagnetic force is transmitted via the photon, the strong force by gluons (eight of them), and the weak force by $W^{\pm}$ and Z^0 bosons. A particle with electric charge exchanges a photon with another particle with electric charge. When the other particle catches the photon, it changes its direction or energy. Any charged particle, lepton, quark, or charged gauge boson can emit or absorb photons to interact electromagnetically.

Force	Mediator	Charge Type
Gravity	Graviton	Mass
Electromagnetism	Photon (γ)	Electric Charge
Strong	Gluons (g)	Color
Weak	$W^{\pm}, Z^0$	Weak Charge

Strong interactions are modeled as gluons passed between colored objects. The only particles with color are the quarks, so when quarks and electrons interact with each other, they do so electromagnetically, not strongly. Gluons carry color and anti color (unlike photons which don't have charge, gluons have two), so that after an interaction the composite quark objects are still colorless.

$W^{\pm}$ and Z^0 bosons mediate weak interactions. Unlike gluons and photons, these bosons are amazingly heavy. They only exist for a short time, but they can interact with every other particle except gluons.

These particles are found in many places. Some occur naturally. Cosmic rays, which consist of pions, muons and neutrinos with a smattering of rarer particles, hit the earth all the time. Pions are made of quarks and they are absorbed at high altitudes. Muons penetrate to the earth's surface and bombard us all the time. Neutrinos are abundantly produced by stars (including our own sun, of course) through nuclear beta decay ($n \rightarrow p + e + \bar{\nu}$). Particle physicists have used these sources to good effect, and also use particle accelerators. Particle accelerators start with a beam of electrons, protons, or nuclei, accelerate it to high energy using electric fields, and smash it against a fixed target or against another beam of particles to produce many secondary particles. Heavier particles require higher powered acclerators.

1.3 Detectors

Detectors *see* the particles indirectly. They look at the ionization trail left by a charged particle in a medium, light emitted from charged particles, or many particles showering from either a charged or a neutral particle. Without precise detectors, we would have little understanding of the forces and particles above.

When the charged particle passes through the medium it kicks electrons off atoms. This slows the particle down a tiny bit, but more importantly, it

tells the detector the location of the track [4]. Early bubble chamber photos showed the ionization trails produced by charged particles in huge chambers of liquified gas. Cycling bubble chambers were timed to keep the liquid just under its boiling point until immediately after the particles passed through. Then the piston would be released slightly, which caused bubbles to form all along the ionization trail. These were photographed and then erased by pushing on the piston again. No detectors today can take such precise pictures of events as these bubble chambers, but new detectors analyze events electronically much faster and over a much larger area than the early bubble chambers could.

If we put an electric field across an ionization trail, the electrons can't recombine with the ions. If the electric field is quite small (500 V/cm), the electrons drift with relatively constant velocity toward a positive cathode. They can travel coherently for a meter or more if there is a magnetic field in drift direction to make the electrons spiral about their axis of motion. Chambers of this sort are called time projection chambers.

Some wire chambers take advantage of the fact that in a magnetic field charged tracks curve in a helical path. We can calculate the momentum of the particle with the formula $r = \frac{pc}{qB}$, where r is the radius of the track, p the momentum, c the speed of light, q the charge, and B the magnetic field. When measurements are taken at intervals along the path, the computer can trace it and calculate the momentum.

At a slightly higher electric field (10^4 to 10^5 V/cm), the electrons accelerate rapidly, causing secondary ionizations. These secondary particles do the same

until an avalanche of electrons hits the cathode (and the slower ions hit the anode). If the electric field isn't so high that all avalanches look the same, the number of electrons is proportional to the number of original ionizations, hence proportional to the voltage drop on the cathode. This is called a proportional wire chamber. Notice that proportional wire chambers are generally smaller than time projection chambers because the electric field needs to be so large that it would require a prohibitively expensive and massive chamber.

At the highest electric fields, above the limited proportionality region mentioned previously, we reach the Geiger-Mueller mode or trigger mode. At this level, the ionizing track causes a huge increase in the number of ultraviolet photons in the avalanche. Where previously they had a relatively insignificant effect on the shape of the avalanche, here they propagate in all directions creating photoelectrons in the whole volume and walls of the counter, which leads to a complete discharge of the detector. Every ionizing track through the chamber discharges the same way, regardless of the velocity or charge of the track. The detector is self-quenching; the voltage drop in the circuit produced by the charge particles reduces the electric field, releasing the ions and electrons to recombine and resetting the chamber. Geiger-Mueller chambers are cylindrical in shape with the anode in the middle and the outside walls as the cathode. The same principle (and voltage) applied to a parallel plate chamber causes a visible spark to occur in the region of the ionization trail. This detector is called a spark chamber.

Scintillating fibers and plates are rapidly becoming the dominant tool for

particle detection. They require little or no maintenance, have a rapid rise time, and allow tremendous flexibility in design. A plastic or glass fiber is doped with a scintillating material which releases light of a known wavelength when it is hit with ionizing radiation. The light would be immediately re-absorbed by the dopant except that its wavelength is shifted to a longer one by a second dopant, the waveshifter. In a well-engineered system, this longer wavelength lies outside the absorbtion spectrum of the fiber, so the light travels unmolested to a phototube or silicon photo-sensitive chip to be read out. No information other than the digital hit is available. This is different from proportional wire chambers, which give information on the number of charged particles which hit a wire and the time the charges drifted. However, wire chambers are limited to straight lines and shorter lengths than fibers are.

Çerenkov chambers are the odd ones in this list. Instead of relying on the ionization trail left by a charged particle, these chambers look for the light cone emitted by a charged particle slowing down. The chambers are made by lining a clear medium with photomultiplier tubes. When a fast charged particle enters the medium, its speed is momentarily greater than the speed of light in the medium, so it slows down and emits light. The cone of light hits photomultiplier tubes, leaving a ring-shaped signature in the chamber. If the chamber is filled with gas, its pressure can be tuned to respond only to particles of particular masses or speeds.

All of the above detectors sense only charged particles. Neutral particles can only be seen if they decay or are made to decay to charged particles in

a dense medium. The incoming particles strike a metal plate and produce a shower consisting of particles from the metal plate and by-products of the decaying particle. On the other side of the metal plate is a scintillating plate, which emits light proportional to the number of charged particles crossing through it. This light is collected and measured, and the signal is proportional to the energy of the incoming particle. This is called a sampling calorimeter.

A homogeneous calorimeter is a large block of scintillating material. Lead glass and Sodium Iodide crystals are common choices. Particles entering the crystal shower decay into a collection of charged and neutral decay products which in turn decay. Light from recombination of ions in the scintillating crystal travels to a phototube. The energy of the original particle is proportional to the voltage pulse from the phototube.

These detectors enable researchers to make precision measurements of particles and the forces between them. At Fermilab and many other accelerators around the world particle physicists help develop an understanding of the way energy and matter mix. Who is to say where this knowledge will lead us?

Chapter 2

The Standard Model

The accelerators and detectors around the world, as well as the many cosmic ray experiments, have aided physicists in forming a theoretical understanding of the way particles interact. This understanding, called the standard model, describes these three fundamental forces of nature: the electromagnetic force, the (nuclear) weak force and the (nuclear) strong force. Gravity is not included in the standard model.

The mathematical framework of the standard model is quantum field theory [5], a sophisticated combination of quantum mechanics and special relativity. Quantum mechanics describes physical systems in terms of the quantum state of the system, where initial conditions help to determine probabilities for various final states but not guaranteed answers. The theory of relativity allows the calculation of properties of things that are traveling close to the speed of light, and it accounts for the behaviour of particles that have no mass, such as photons, gluons and neutrinos. Calculations with quantum

field theory use a set of particles and one or more of these force laws: QED (Quantum Electrodynamics), electroweak theory, or QCD (Quantum Chromodynamics). Scattering distributions, decay rates, bound state interactions and fragmentation are all calculations of interest to physicists.

The standard model has 18 parameters:

- The six quark masses,

- the three lepton masses,

- four of the nine Kobayashi-Maskawa matrix elements which describe mixing between quark families,

- α, the electromagnetic coupling constant,

- Λ_{QCD}, the QCD scale factor,

- $\sin^2 \theta_W$, the electroweak mixing parameter,

- $m(W)$, the mass of the W boson,

- $m(H)$, the mass of the Higgs boson.

2.1 Quantum Field Theory

Quantum field theory assigns each particle a distribution function, or field, which is promoted to the status of an operator. If a field $\psi(x)$ represents a particle, then $\mid \psi(x) \mid^2$ is the probability of finding the particle in a given state described by the variable x. $\psi(x)$ must satisfy an equation of motion.

In non-relativistic quantum mechanics, the field of a particle must satisfy the Schrödinger equation. Relativistic particles without spin satisfy the Klein-Gordon equation, spin $\frac{1}{2}$ particles satisfy the Dirac equation, and spin 1 particles satisfy the Procca equation [5]. Solutions of these equations give the following essential results:

- Quantum field theory requires the existence of both particles and antiparticles.

- Particles can be created and destroyed.

- Mass and energy are related by $m^2c^4 = E^2 - p^2$.

At a practical level, the quantities we need for laboratory work are calculated using the Feynman rules and Fermi's *Golden Rule* [5]. Feynman rules govern the transition from fundamental field theory (Lagrangians) to its application in scattering and decay experiments. Fermi's Golden Rule states

$$\text{(transition rate)} = \frac{2\pi}{\hbar} \, |M|^2 \times \text{(phase space factors)}$$

where the transition rate, $d\Gamma$ or $d\sigma$, is the decay rate or the cross section, and M is the matrix element determined from the Feynman rules. This way we calculate the cross section σ for a scattering experiment, or the decay rate Γ for a particle and then the lifetime using $\tau = \frac{1}{\Gamma_{tot}}$.

2.2 Quantum Electrodynamics

Quantum electrodynamics (QED), the first and simplest of the gauge theories, can be traced to Maxwell's work a hundred years ago, when he joined the electrical and magnetic forces in one mathematical framework. Though consistent with special relativity, Maxwell's theory required modification to account for the quantum nature of particles. Quantum Electrodynamics was invented in the 1940's by Feynman, Schwinger, Tomonaga and others [5]. QED is the model on which all the other dynamical theories are based. It describes the way that electrically charged particles interact with each other through exchange of a gauge boson, the photon.
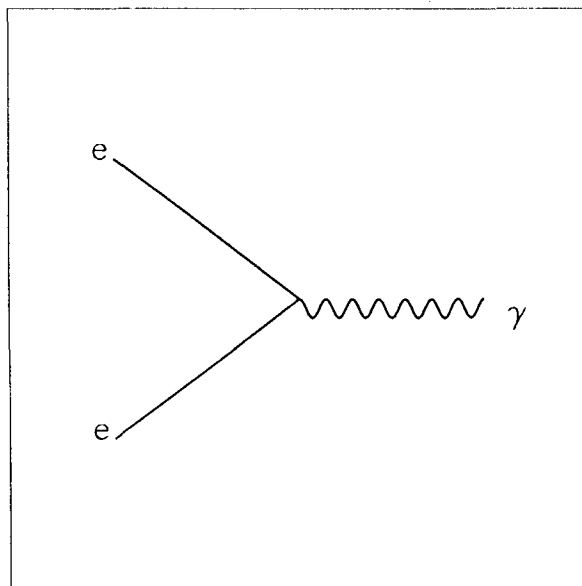
Figure 2.1: Fundamental process for QED interactions.

The fundamental process of QED is this: charged particles, such as electrons or quarks, interact with each other by emitting or absorbing a photon.

Feynman describes the fundamental process in a diagram as in figure 2.1, where momentum and energy are conserved at the vertex. The fundamental process is always connected to another vertex. The lowest order QED interation is shown schematically in figure 2.2. The fundamental process cannot happen alone; that is forbidden by momentum and energy conservation rules. If it were to happen by itself, then $e \rightarrow e + \gamma$ in the initial e's reference frame would send out a moving e and a γ opposite. The energy of the moving e is greater than the energy of the original resting e and energy conservation is violated. Therefore each fundamental vertex is connected to another vertex of some kind. Since Feynman's rules dictate that only the momenta of the outgoing particles needs to be conserved, each individual vertex need not do so.
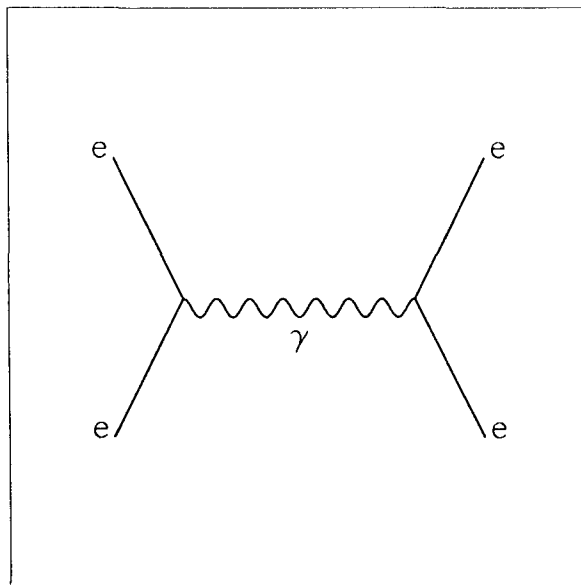
Figure 2.2: Lowest-order QED process.

Calculation of any QED process involves assembling as many of these diagrams as are necessary or desired, in all the possible unique combinations, and performing the integrations that they dictate. If there are several diagrams to account for a process, the contributions are summed to get the correct value for the amplitude. Then Fermi's Golden Rule gives the decay rate or scattering cross section of the process. More complicated processes have a smaller integral because each vertex added to the diagram introduces a factor of α = 1/137, the coupling constant for QED. Thus complicated processes have a small effect on the result and need not be calculated.

It is important to note that internal lines in the diagrams represent virtual particles that may have a different mass than the measured mass. The mass of these *off mass shell* particles approaches the true mass as the lifetime of the particle increases.

2.3   Weak Interactions

In nuclear beta decay, a nucleus becomes a slightly lighter nucleus by emitting an electron, apparently alone. Conservation of energy requires that if the electron is the sole decay product, the energy of the electron in the center of mass from must be the same from experiment to experiment. This is not at all what the experimenters saw. They saw that the electrons in the experiments were emitted within a range of energies, consistent with two-body decay. In 1930, Pauli proposed a new particle, the neutrino (little neutral one). Fermi applied the theory to beta decay and met with great success. Later the theory was

applied to muon decay with success, but in all cases the neutrino interacts so weakly that the direct experimental observation was missing. At the Savannah River nuclear reactor in South Carolina in the mid 1950's, Cowan and Reines [5] saw the inverse beta-decay reaction $\bar{\nu} + p^+ \rightarrow n + e^+$ in a large tank of water, direct evidence for the neutrino.

This work motivated the theory of weak interactions. The mediators of the weak force are the $W^\pm$ and Z^0 bosons. Figure 2.3 shows examples of the fundamental vertices (which must be connected to others, as in QED). The W (non-abelian) bosons can interact with the Z and with the photon, so new vertices come about. Further, through emission of a W, quarks can change family (flavor) grouping, as in $b \rightarrow cW^-$.

Kobayashi and Maskawa modeled the family mixing using the matrix which bears their names and contains the experimental information governing the rates at which these decays can cross familial boundaries in the quark systems. Glashow, Weinberg and Salam combined QED and weak theory into electroweak theory. The Higgs mechanism describes the masses of the W and Z particles and shows how it is the difference in mass between the weak mediators and the photon which accounts for the difference in strength of the interactions [5].

2.4 Quantum Chromodynamics

The mathematics to describe the strong force is QCD (Quantum Chromodynamics). As long ago as 1934, Yukawa proposed that these nucleons inter-
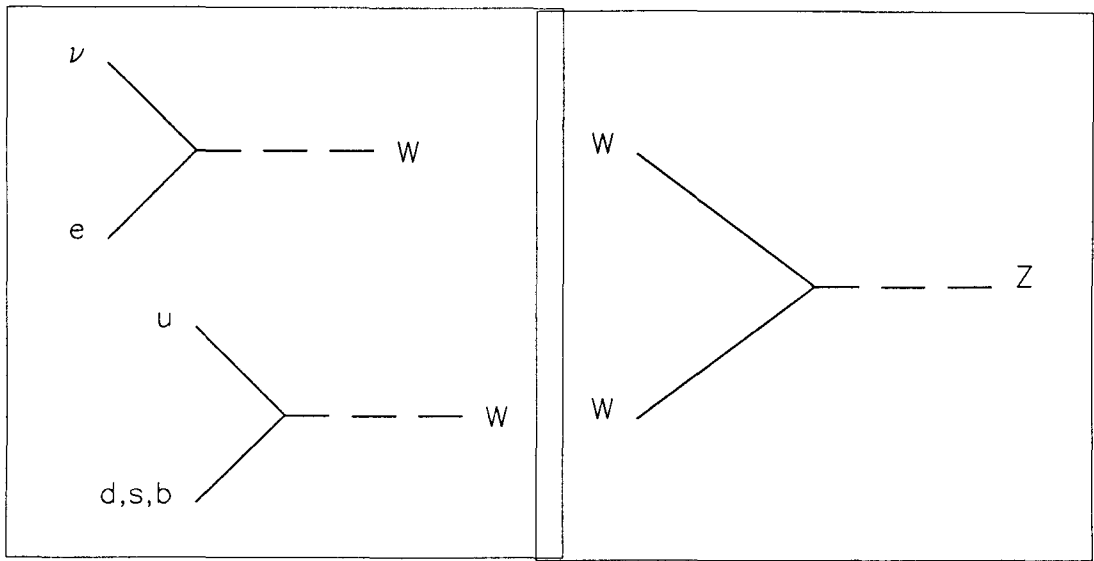
Figure 2.3: Fundamental process for weak interactions.

acted with some sort of field between them, and that the quantum for that field could be π mesons in the same way that the photon is the quantum for the electromagnetic force. While compelling, this wasn't quite correct. The whole picture wouldn't become clear until Gell-Mann and Zweig proposed the quark model (Gell-Mann invented the word) in 1964 to explain the puzzling behaviour of mesons, baryons and strange matter. They proposed (correctly) that mesons have two quarks, baryons three, and that strange matter has a strange quark combined with ordinary up and down quarks. Now, with the addition of the full QCD (Quantum Chromodynamics) theory in place, QCD models the strong force between protons and neutrons as a complicated system of quark-quark QCD interactions.

QCD assigns each of the quarks in a meson or baryon a color (red, yellow or blue), arranged in such a way as to leave the object colorless. This triangular mathematical metaphor (with color a convenient model) effectively explains

18

an apparent paradox. The Pauli exclusion principle requires that spin 1/2 particles must not occupy the same space at the same time. Yet, one of the baryons discovered in 1964 was the Ω baryon, which is composed of three s quarks. Physicists had already discovered the Δ^{++} (uuu) and Δ^- (ddd) baryons. If the three quarks in these baryons are really identical fermions, they shouldn't be allowed to exist in the same bound state. In 1964, O. W. Greenberg speculated that if there were some additional quantum number not yet discovered, these three quarks might not be identical. He assigned the colors red, blue and green to the quarks and asserted the axiom that all naturally occurring particles are colorless. There are two ways that naturally occurring particles might be colorless; baryons have one quark of each of the three colors, and mesons have a quark of one color and an antiquark of the opposite color.

This theory cured a problem that other theories of the day had in computing the production rates of hadrons from e^+ e^- collisions. They predicted the rates to be a factor of three lower than the rates actually seen. With the tri-fold symmetry in the new theory, the rates were calculated exactly.

Physicists remained unconvinced until the "November Revolution," when the J/ψ ($c\bar{c}$) was discovered at SLAC (Richter) and at Brookhaven (Ting). This particle had been predicted pretty closely by Bjorken and Glashow, as well as by Glashow, Iliopoulos and Maiani. It was the first evidence of the predicted but unseen quark, c or charm quark. After the charmed mesons and baryons appeared, then the τ lepton, the b (bottom) quark, and in 1994, the

t (top) quark were discovered.

QCD is similar to QED except that the one photon is replaced with eight gluons (8 fields). This is a result of the tri-fold symmetry again. In this case, color plays the role of charge, so the fundamental reaction, $u \rightarrow u + g$, must include color, $u(red) \rightarrow u(green) + g(red + antigreen)$. See figure 2.4. In addition to this vertex, the interactions $g \rightarrow g + g$ and $g + g \rightarrow g + g$ are allowed, as opposed to the equivalent photon-photon QED interactions, so the mathematics of calculating interaction rates is much more complicated.
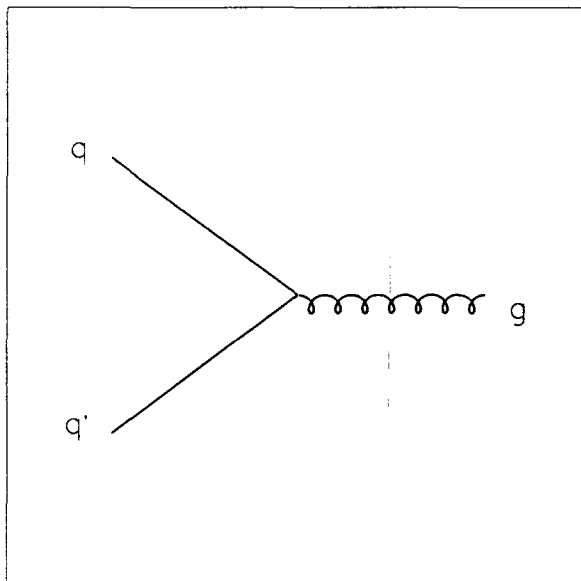
Figure 2.4: Fundamental process for QCD interactions.

These gauge field self interactions affect α_s, the coupling constant which represents the strength of the interaction vertex. In QED, higher-order corrections to the fundamental vertex screen the effects the charges have on each other in the interaction, and thus decrease the effect of the force at large dis-

tances (small energy scales). In QCD, the gluon self-interactions have the opposite effect. Experimentally we see that α_s grows larger the farther apart the quarks go. Within the proton the quarks are essentially free but the farther apart the gluons go, the stronger the coupling is. From the energy put into the system to pull the quarks apart, it is economical for a pair to appear out of the vacuum to bind to the separated quarks. This is called fragmentation. (UCLA professor J. Schwinger laid the foundation for this concept by calculating spontaneous e^+e^- production in strong electromagnetic fields.) So, unlike QED, where many free particles carry charge, we see no free particles with net color. This experimental evidence led to the axiom that all particle states are color neutral or color singlets, and that quarks are always bound up in composite particles.

It is hard to extract meaningful predictions using QCD at low energies since α_s is large. The perturbative methods which work so effectively in QED are extremely difficult to apply in studying the strong interactions. However, where α_s is small at high energies of the interactions, such as the high energy scale at Fermilab, production rates are modeled adequately.

2.5   Flavor-Changing Neutral Currents

Flavor-changing neutral currents appear in electroweak decays at low rates. These are decays where a quark decays into another quark of the same charge but a different family, plus decay products. To first order they are forbidden in the standard model. For example, the decay $s \rightarrow uW^-$ is allowed by

the standard model, but the decay $s \rightarrow dZ^0$ is not. Flavor-changing neutral currents appear only at low levels because they proceed in loop-order or higher diagrams like in figure 2.5.
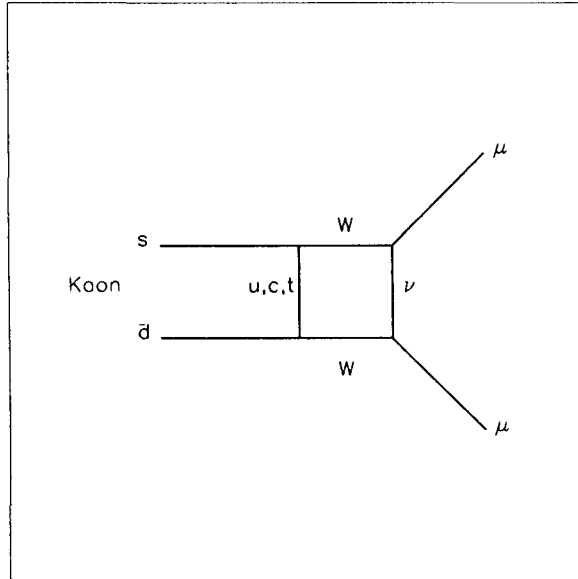
Figure 2.5: Lowest-order FCNC process.

The mathematics which represents these physical observations is contained in the KM matrix, which records the rates at which the W decays can happen and leaves the Z decays at zero rate. A very interesting thing happens when the loop diagrams are calculated in the usual fashion. If only the diagrams with u quark in the loop are calculated (as was done before the discovery of the charm quark), the predicted rate is much higher than the experimental measurements. For example, the predicted rate for $K^0 \rightarrow \mu^+\mu^-$ (using the Feynman diagram in 2.5) was high before the discovery of the charm quark, but experiments did not see the decay. The reason is that the three different

families of u-type quarks should appear in the loop. Since the KM matrix is unitary, the integrals for the different diagrams add destructively, almost entirely cancelling each other out. The sum of the KM matrix elements is weighted by terms involving the mass of the quark in the loop. Therefore, a small rate is allowed because the masses of the u, c, and t quarks are different. It was this feature of the calculation that led Glashow, Iliopoulos and Maiani to propose the charm quark in 1970 (the GIM mechanism), and allows the rare B decays discussed in this thesis.

Chapter 3

Literature Review

This study of rare B decays follows the major developments in the field from the first experiments, which showed that the top quark must exist, to very precise calculations of the polarization of the decay as a function of dilepton mass. It also includes a summary of the current state of the work. Interesting in its own right, a historical study of rare B decays puts the current state of the field in perspective. The experimental work in the field is by no means finished, so in order to interpret new results it is essential to have a sense of the theoretical expectations. In order to put the results in perspective, it is good to have a sense of how those theoretical expectations have changed with time.

In general, each paper has the same form. The authors choose a Lagrangian which represents the physics they model, and from which they derive Feynman diagrams, calculate the effective Lagrangian (amplitude), sandwich it between the initial and final states and calculate the matrix element. They make various

approximations about masses and momenta of particles, square the matrix element, integrate over the phase space, then use Fermi's Golden Rule to get the rate. The standard model Lagrangians and Feynman diagrams are common to all such calculations. The interesting changes between the papers are the choice of Lagrangian, Feynman diagrams, the approximations used, and the introduction of new models for non-standard model physics.

There are several physics sources of differences from the basic electroweak standard model diagrams. Short distance QCD effects add Feynman diagrams with gluons in them to the calculation. Exclusive decays (QCD effects involving mesons rather than quarks) add long distance interactions between the quarks in the mesons. The standard model makes no direct predictions for these form factors, so authors speculate on the details of the binding of quarks inside mesons. Most authors calculate their branching ratio predictions for a range of values for the then-unknown top quark mass. In addition, authors calculate effects of a non-standard model physics, fourth generation, two-Higgs models, and anomalies in the couplings of the W boson with other bosons. The first subject here is the calculation of the basic diagrams.

3.1 Early Theoretical Calculations

Before 1982, all flavor-changing neutral current studies were performed on the Kaon system. **Inami and Lim** [6] wrote a comprehensive 1981 work on the calculation of the rates of $K_L \rightarrow \mu\bar{\mu}$, $K^+ \rightarrow \pi\nu\bar{\nu}$ and $K^0 \leftrightarrow \overline{K^0}$, which formed the foundation for calculations covered in this section. With the discovery of

the Υ in 1977 [7] and the B^0 and $B^\pm$ in 1983 [8], B mesons qualified for similar studies.

In 1982, physicists were trying to understand why the top quark hadn't been found at what they considered to be all the likely energies. Further, there was (and still is) no *theoretical* reason why the top quark must exist; only the symmetry of complete pairs argued for its existence. Theories which proposed only five quarks had to be tested. **Kane and Peskin** proposed [9] that studies of B decays into two leptons plus other products could be a test of five-quark models. Kane and Peskin weren't the only authors to do this exercise, but theirs is unique in that the result could be tested easily by experiment. The work was based on the same arguments that successfully predicted the existence of the charm quark. Kane and Peskin considered all the less-extravagant extensions to the standard model which dispensed with the top quark and found that they all allowed high rates of flavor-changing neutral current decays. Though the theories have different mathematical reasons for allowing the flavor-changing neutral currents, Kane and Peskin proved that the rates of even the most exotic still satisfied the inequality

$$\frac{\Gamma(B \to X l^+ l^-)}{\Gamma(B \to X l^+ \nu)} \geq 0.12,$$

where X indicates the rate is a sum over all mesons and baryons, and l is either e or μ. They assumed that the b quark behaves as a weak SU(2) singlet which decays by the exchange of W or Z bosons, the W bosons mediating the semileptonic decays and the Z the dileptonic. Since the B decays somehow, it

must maintain its Cabibbo mixing with d and s, so they treated the dileptonic decay as though it were $d' \to d'Z$ or $s' \to s'Z$. They advocated that the experimental tests be done and specified that the decay products be analyzed carefully so that only the leptons coming from the primary decay of the B would be counted. Since Peskin was at Cornell University, it comes as no surprise that this test was carried out at CLEO a year later, but before those results came out two other relevant and interesting papers were published.
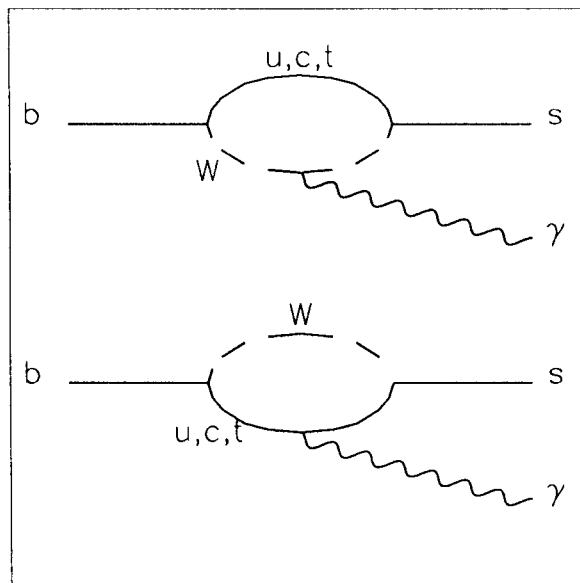
Figure 3.1: Feynman decay diagrams for loop-order flavor changing neutral current decay as calculated by Campbell and O'Donnell.

Campbell and O'Donnell [10] reminded physicists in 1982 that with six quarks, the Kobayashi-Maskawa model is "naturally flavor diagonal," so that in its full six-quark manifestation the process which Kane and Peskin studied above doesn't happen. That is, tree level quark Z-exchange doesn't mix flavors. Flavor-changing neutral current decays can proceed only at loop order. In

this first paper on flavor-changing neutral currents in the b system, Campbell and O'Donnell examined the process $b \to s\gamma$, where the Feynman diagrams of interest are shown in figure 3.1. This calculation brought out several interesting points. The effective Lagrangian is proportional to a weighted sum of the Kobayashi-Maskawa matrix elements. Since the matrix is unitary, that sum would go to zero (a GIM cancellation, for Glashow, Iliopolous and Maiani [11]) except that the weights depend on the mass of the quark in the loop. Since the weights increase with heavier quark mass, the rate depends primarily on the top quark mass rather than the masses of the other quarks, thus the plot of the rate versus top quark mass in the paper is a monotonically increasing function. Campbell and O'Donnell predicted the inclusive branching ratio

$$BR(b \to s\gamma) \sim 2 \times 10^{-4}$$

for top quark mass of 160 GeV/c^2. This was exactly the measured branching ratio which CLEO reported in 1994. More importantly, this work unfortunately established that (with one notable exception) only these two Feynman diagrams would be used for calculations of flavor-changing neutral currents in the b system until 1987. This precedent is all the more surprising in the light of Inami and Lim's [6] important work on loop order Kaon decays, where they calculated the rates of all the diagrams of interest.

The notable exception was work published in 1983 by **Grządkowski and Krawczyk** [12], who used a neutral Higgs particle in the calculation and introduced the other important Feynman diagrams. They calculated the

amplitude for $b + \bar{s} \rightarrow \tau^+ + \tau^-$ (which has the same amplitude as $b \rightarrow s + \tau^+ + \tau^-$), in the case where the Higgs particles in a scalar doublet are much lighter than the W boson. For this reason the paper is of limited value now, except for the introduction of the Z and box diagrams. Grządkowski and Krawczyk modified figure 3.1 by causing the photon, γ, to decay to two leptons, τ's. Since they used a virtual photon in this case, they added a diagram where they replaced the γ with a Z particle. In addition, they added figure 3.2, the two W exchange diagram. This paper went unnoticed. Other authors assumed that the Z and box diagrams would have a small contribution to the overall branching ratio. That assumption would be discredited by Hou, Willey and Soni in 1987, after four more years of incomplete calculations.
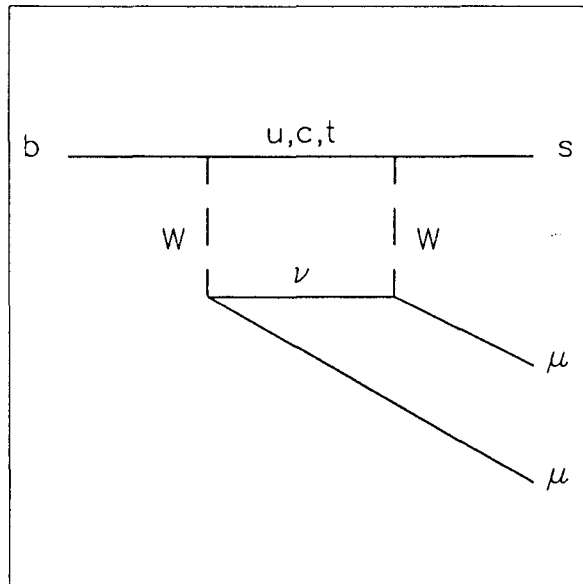
Figure 3.2: Feynman box decay diagram for a loop-order flavor changing neutral current decay as calculated by Grządkowski and Krawczyk.

3.2 First Experimental Searches

CLEO answered Kane and Peskin's question in March of 1983 in publishing its search for B decay anomalies [13]. Using many decay modes, including the b → l^+l^-s mode, the physicists systematically studied exotic models with various properties, including models without top quarks, using data collected from $\Upsilon(4S)$ decays at the Cornell Electron Storage Ring (CESR). CESR is an e^+e^- machine with 10.6 GeV center of mass collisions. Lacking the statistics needed to look for each decay mode individually, they looked at the gross properties of all the events received from $\Upsilon(4S) \to B\overline{B}$ and → B^+B^- decays in their 10.6 pb^{-1} sample in order to rule out classes of models as a whole. Examining the distribution of events with respect to energy of the decay products, they determined that the exotic models without top quarks which they studied were all wrong. Only the standard six-quark model could accurately describe the particle yields and energy fractions.

The **JADE** collaboration at PETRA at DESY published four days later [14, 15], confirming this judgment against exotic models with their search for the decay $b \to \mu^+\mu^-X$. In 30,000 hadron events collected from 35 GeV e^+e^- collisions, they required two muons to be less than 15° apart and muon $p_t > 1.5$ GeV/c, giving them 17% acceptance for events of this sort. If the six-quark model were wrong, they expected to see 18 signal events over 1.5 background events. They saw two events. The JADE Collaboration calculated the limit

$$BR(b \to \mu\mu X) < 7 \times 10^{-3} \text{ at } 95\% \text{ CL},$$

firmly ruling out all but the most pathological five-quark models from consideration.

In October of 1984, **CLEO** looked for the decays $b \to \mu^+\mu^- X$ and $b \to e^+e^- X$ [16]. With a better understanding of their detector and 40.6 pb^{-1} of data with 42,200 B mesons (60% charged and 40% neutral), they had enough data to look for exclusive decays. They applied suitable topological and kinematic cuts to find an inclusive limit of

$$BR(b \to l^+l^- X) < 3.1 \times 10^{-3} \text{ at } 90\% \text{ CL},$$

where the result is averaged over $l = e$ and $l = \mu$, and X indicates the rate is a sum over all decay products. They also calculated the quantity discused by Kane and Peskin,

$$\frac{\Gamma(B \to Xl^+l^-)}{\Gamma(B \to Xl^+\nu)} < 0.029 \text{ at } 90\% \text{ CL}, \quad < 0.046 \text{ at } 99.9\% \text{ CL}.$$

This limit is a factor of four (factor of 2.6 at 99.9% CL) below the limit looked for by Kane and Peskin, and so ended any serious consideration of five-quark models.

3.3 Specific Predictions

With this experimental evidence for the top quark, rare B decays were set aside for a couple of years. By 1986, it was clear that the B meson system

31
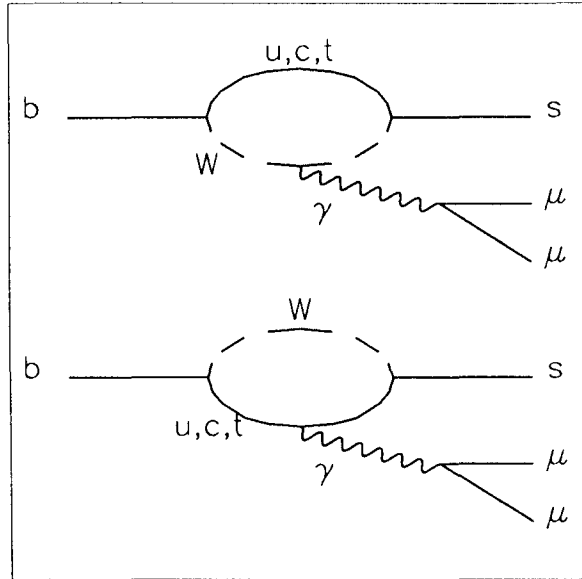
Figure 3.3: Feynman penquin decay diagrams for loop-order flavor changing neutral current decay as calculated by O'Donnell.

would provide insight into CP violation and weak processes, and that it offered various advantages over the Kaon system. The B system probes a different energy region and has a larger phase space than Kaon decays, allowing more decay channels. Loop diagrams allow the B mesons to decay into modes not allowed by first order processes, so they are naturally of interest to physicists. Finally, as the number of laboratories producing a substantial number of B mesons increased, so too did the frequency of published papers on rare B decays increase.

O'Donnell [17] speculated that it was time for specific calculations, so he carefully calculated the branching ratios for several exclusive decays. He used a mass of the top quark in the range 40 to 240 GeV/c^2, but focused on the penguin diagrams alone (see figure 3.3). Although he preferred the $b \rightarrow s\gamma$

decay mode as it had "a very distinctive signature," he recognized that "it might be preferable to look for a final state containing a lepton pair and a strange particle." His calculations used his earlier work on $b \to s\gamma$ with the modification that the photon was a virtual particle which would decay into a pair of leptons as in figure 3.3. The relevant matrix elements for exclusive decays can be expressed in terms of sets of Lorentz-invariant form factors. However, these depend on non-perturbative QCD, and so authors have to introduce assumptions about how quarks are bound into mesons. The choice of form factors varied between authors. Of the various theoretical predictions for branching ratios that O'Donnell calculated, the most interesting for this analysis are at the top quark mass of 160 GeV/c^2. The mode $b \to l^+l^-s$ is for $l = e$ or $l = \mu$, and a sum over all strange mesons and baryons.

$$BR(b \to l^+l^-s) \quad \sim \quad 3.2 \times 10^{-6}$$

$$BR(B \to \mu^+\mu^-K^{*0}) \quad \sim \quad 0.7 \times 10^{-6}$$

$$BR(B \to \mu^+\mu^-K^{\pm}) \quad \sim \quad 2.5 \times 10^{-6}$$

$$\frac{\Gamma(B \to e^+e^-K^{*0})}{\Gamma(B \to \mu^+\mu^-K^{*0})} \quad \sim \quad 3.$$

A month later, **Deshpande, Eilam, Soni and Kane** [18] confirmed O'Donnell's work and additionally derived predictions for sensitivity to CP violation in this system and (at a top quark mass of 160 GeV/c^2) the branching ratios

$$BR(b \to l^+l^-s) \quad \sim \quad 2.9 \times 10^{-6}$$

$$BR(B \to \mu^+ \mu^- K^\pm) \sim 1.5 \times 10^{-6}.$$

These results agree well with those of O'Donnell.

Eilam, Hewett and Rizzo [19] pursued this topic further in November of 1986, extending the calculation to include four generations. New, heavier quarks inflated the above branching ratio predictions (for top quark mass of 80 GeV/c^2) by an order of magnitude, as expected from the dependence of the internal loop quark mass on the decay rate noted by O'Donnell.

In two 1987 papers, **CLEO** [20, 21] analyzed many B decay modes. They drew on the 117 pb^{-1} of data (260,000 B mesons) collected from $\Upsilon(4S)$ decays at the Cornell Electron Storage Ring (CESR), approximately three times the data on which they published their previous results. Analysis of the events with detection efficiencies between 5 and 24% due to kinematic and topological cuts enabled them to discover the resonant decays $B \to \psi K^\pm$ and $B \to \psi K^{*0}$, as well as set limits on the rare decays

$$BR(b \to l^+ l^- s) < 1.2 \times 10^{-3} \text{ at } 90\% \text{ CL}$$

$$BR(B \to \mu^+ \mu^- K^\pm) < 3.2 \times 10^{-4} \text{ at } 90\% \text{ CL}.$$

This was a factor of two improvement over their 1984 limit.
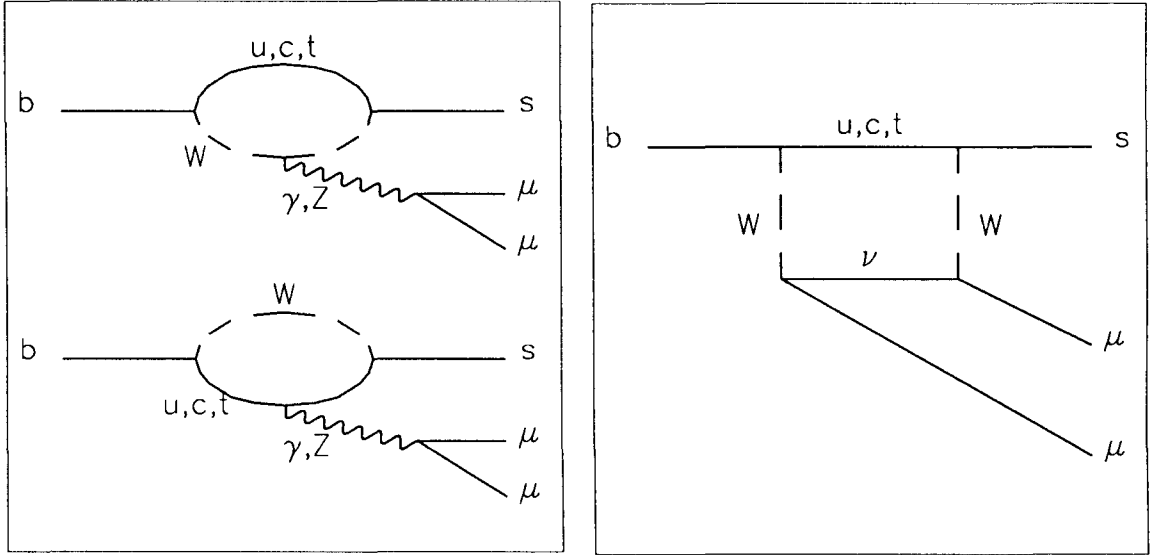
Figure 3.4: Feynman diagrams for the loop-order flavor changing neutral current decay as calculated by Hou, Willey and Soni.

3.4   Z and Box Diagrams

Up to the time of the definitive paper by **Hou, Willey and Soni** [22] in April 1987, only the photon contributions were used in the calculation of the branching ratios. (The one exception is the 1983 paper by Grządkowski and Krawczyk, which was largely ignored by the theory community). Hou, Willey and Soni note the importance of the Z and box diagrams when the mass of the top quark is heavy and use them to calculate the effects of heavy top quark mass and fourth family. See figure 3.4. They calculate the inclusive branching ratio

$$BR(b \rightarrow l^+l^-s) \sim 1.0 \times 10^{-5}$$

at a top quark mass of 150 GeV/c^2. It is a factor of 5 times bigger than the inclusive rates calculated by O'Donnell or Deshpande, Eilam, Soni and

Kane, above. It remains sensitive to the internal loop quark mass and so to a heavy top quark and a fourth generation. They go on to say, "pushing the experimental branching ratio limit down one order of magnitude would set valuable limits on parameters of the 4×4 Kobayashi-Maskawa matrix and/or the fourth generation quark mass." Their standard model calculation is the same as that of Inami and Lim [6], but with the Kaon mass exchanged for that of the B meson. Since they assume $m_t = 50$ GeV/c^2 it is hard to extract meaningful predictions of fourth generation rates for $m_t = 175$ GeV/c^2.

In March of 1988, a full year after their revolutionary work on the full set diagrams, **Hou and Willey** [23] themselves were the first to follow up on the calculations by adding the effect of charged Higgs bosons on the rate. They examined two extensions to the standard model which added another Higgs doublet. Using the limits on the decay modes $b \to s\gamma$, $b \to sl^+l^-$, and $b \to sg^*$ which were available at that time, they could only make mild constraints on the masses of the Higgs particles. Their predictions for the inclusive decay rate vary little between models when they use mass of the top quark as heavy as 120 GeV/c^2.

$$BR(b \to l^+l^-s) \sim 2 \times 10^{-5} \text{ for } m_{H\pm} = 120 \text{ GeV/c}^2$$

$$BR(b \to l^+l^-s) \sim 1 \times 10^{-5} \text{ for } m_{H\pm} = 1000 \text{ GeV/c}^2$$

Later these same authors [24] added the QCD corrections and the inclusive decay modes.

3.5 QCD Corrections

Deshpande and Trampetić [25] did a complete calculation of the decay modes $B \rightarrow l^+l^-K$ for mesons K^* and $K^{\pm}$ and for leptons μ and e. They used the full set of the penguin diagrams and the box diagram as laid out by Inami and Lim [6]. They included the QCD correction for real photon exchange as they had done in an earlier paper [26], but only discussed QCD corrections for the other diagrams. They referred to two types of popular form factors to model the binding of the quarks in the mesons, those of Bauer, Stech and Wirbel [27] and Grinstein, Wise and Isgur [28]. The results from these different functions agreed well with each other (5% different). In addition to their work on a fourth generation, which is used in the last chapter of this thesis, they discovered two items of importance for this work; the K^* rate dominates over the $K^{\pm}$, and the rates of electrons dominate over muons in the K^* case. They estimate the uncertainty in the inclusive branching ratio to be 15 - 20% because of the lack of full QCD corrections, and the uncertainty in the exclusive branching ratios to be 30% from model dependence in the form factors.

$$\frac{\Gamma(B \rightarrow e^+e^-K^{*0})}{\Gamma(B \rightarrow \mu^+\mu^-K^{*0})} = 1.23$$

$$\frac{\Gamma(B \rightarrow e^+e^-K^{\pm})}{\Gamma(B \rightarrow \mu^+\mu^-K^{\pm})} = 1.00.$$

Finally, for mass of the top quark at 150 GeV/c^2, without QCD corrections,

$$BR(b \to l^+ l^- s) = 20 \times 10^{-6}$$

$$BR(B \to \mu^+ \mu^- K^{*0}) = 2.0 \times 10^{-6}$$

$$BR(B \to \mu^+ \mu^- K^\pm) = 0.8 \times 10^{-6}$$

$$\frac{\Gamma(B \to \mu^+ \mu^- K^{*0})}{\Gamma(B \to \mu^+ \mu^- K^\pm)} = 2.5.$$

With partial QCD corrections,

$$BR(b \to l^+ l^- s) = 30 \times 10^{-6}$$

$$BR(B \to \mu^+ \mu^- K^{*0}) = 2.8 \times 10^{-6}$$

$$BR(B \to \mu^+ \mu^- K^\pm) = 0.8 \times 10^{-6}$$

$$\frac{\Gamma(B \to \mu^+ \mu^- K^{*0})}{\Gamma(B \to \mu^+ \mu^- K^\pm)} = 3.5.$$

Grinstein, Savage, and Wise [29] calculated rate as a function of the dielectron mass in the standard model with all the diagrams included and in the extension with a two Higgs doublet. They did QCD corrections using the leading log approximation, different from previous authors. For the standard model, their conclusion was that $BR(B \to e^+ e^- K^\pm) = 6 \times 10^{-8}$ for $m_t = 150$ GeV/c^2 and $m(e^+ e^-) > 3.7$. Using Deshpande and Trampetić's determination that the rates for $K^\pm$ should be the same for both the muons and the electrons,

$m(\mu^+\mu^-) > 3.7$ GeV/c^2, and $m_t = 150$ GeV/c^2, I derive

$$BR(B \to \mu^+\mu^- K^\pm) = 6 \times 10^{-8}.$$

This result shouldn't be compared with the others, since it has a limited $m(\mu^+\mu^-)$ range. However, the authors used the result to compare it to the case of an extension to the standard model with two Higgs doublets. The branching ratio increased slightly. The authors didn't integrate their rates over dimuon mass or explore the relationship with m_H, so their work is of little use here.

Over the course of the following year, **Grigjanis, O'Donnell, Sutherland and Navelet** [29, 30, 31] confirmed this work and went on to calculate the QCD corrections to the form factors for all the diagrams in the decay as well as the QCD radiative corrections. QCD corrections suppress the decay by a factor of 1.4 at $m_t = 160$ GeV/c^2.

3.6 Long Distance Resonances

In February of 1989, **Lim, Morozumi, and Sanda** [32] included the interference of the ψ and ψ' resonances (long-distance QCD effects) with the non-resonant rate for the first time. This work set the stage for all future work on these decays. For the first time, Lim, Morozumi and Sanda calculated the branching ratio as a function of dimuon mass and drew the distinctive spikey spectrum of the resonance effects. They saw the dramatic set of peaks from the ψ and ψ', which was expected, and they also saw the far-reaching

interference effects of these resonances on the shape of the curve, which were not expected. The resonances affected the rate along the entire dimuon mass range. Even cutting with a window 10 MeV/c^2 wide around the ψ and ψ' peaks, the branching ratio with the long-distance effects was over twice as big as that without (at $m_t = 30$ GeV/c^2, less effect for heavy m_t).
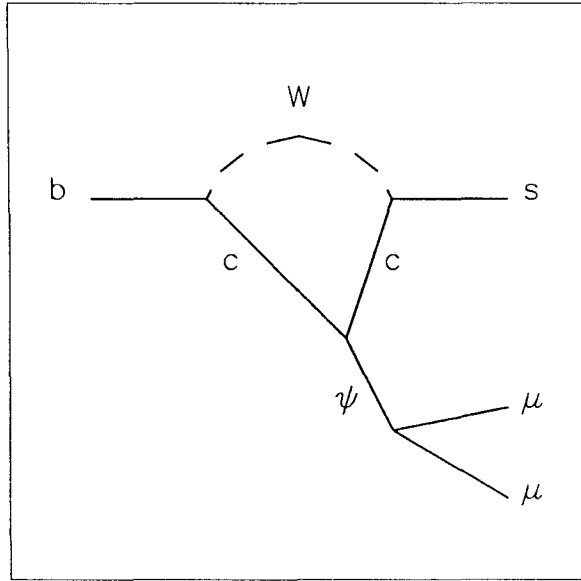
Figure 3.5: Feynman decay diagrams for long distance effects which interfere with the penguin decay diagrams.

The source of the resonance was the $c\bar{c}$ intermediate state in the process $b \rightarrow cW^- \rightarrow c\bar{c}s \rightarrow l^+l^-s$, which came from the QED penguin diagram (γ from c side of loop) when they included nonperturbative QCD effects in the calculation, that is, when they refused to assume that the quarks in the loop were free [33]. See figure 3.5. They included QCD effects according to the proceedure in [34], to present an effective Lagrangian which could be used by future authors. The interference in $b \rightarrow l^+l^-s$ depends crucially on m_t. They

encourage "a detailed experimental check of the invariant mass distribution," as it will "put a stringent limit on physics beyond the standard model – or it may establish the presence of a new effect." Unfortunately, they don't calculate the particular exclusive decays, leaving that for other authors.
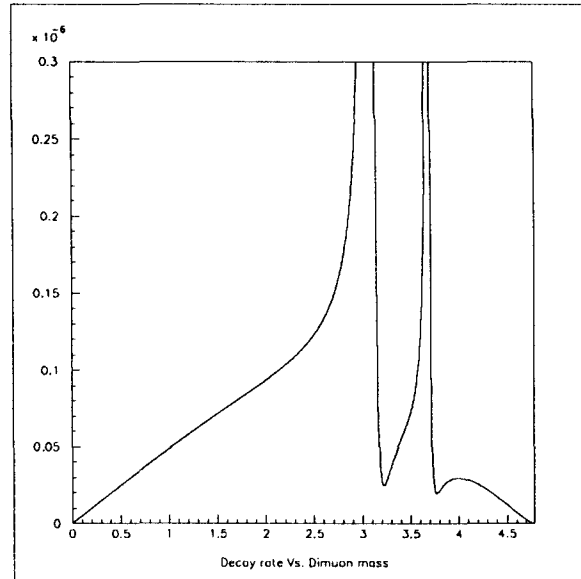
Figure 3.6: Dimuon mass spectrum calculated by Grant Baillie for the exclusive decay $B \to \mu^+\mu^- K^\pm$, based on the work of Lim, Morozumi, Sanda.

Independently and concurrently, **Deshpande, Trampetić and Panose** [35] published their work on the same issue. They found almost identical results as Lim *et al*, except their interference had the opposite sign, resulting in destructive interference below the resonance. They plot the $m(\mu\mu)$ on a log scale and conclude that away from the resonances the differential rate changes very little from the non-resonant case. They recommend a cut to use only events with dimuon mass below 2.9 GeV/c^2, which they claimed would leave about 50% of the non-resonant events (a reduction of 55% for $B \to K^* e^+ e^-$

41

and 50% for $B \rightarrow K^{\pm}e^+e^-$, same for μ). This phase of the interference is an important issue, since the cuts used to isolate non-resonant events and the expected signal from the decays would change dramatically with it. The fight over the phase of the interference would last until 1991, two years of confusion.

The phase difference between the work of Lim, Morozumi and Sanda [32] and that of Deshpande, Trampetić and Panose [35] had bothered theorists for over a year before **O'Donnell and Tung** [36] came out with their determination. They judged in favor of Lim *et al.*, observing that the two methods differed only by a phase, and that any phase different from that of Lim, Morozumi and Sanda violated unitarity. Ali and Mannel [37] confirmed this determination in 1991.

CLEO improved its limits [38] on the branching ratios of $B \rightarrow \mu^+\mu^- K^{*0}$ and $B \rightarrow \mu^+\mu^- K^{\pm}$ in 1989. The analysis was nearly identical to the previous one, but twice the data (212 pb^{-1}, 240,000 $B\overline{B}$ events) helped improved the search.

$$BR(B \rightarrow \mu^+\mu^- K^{*0}) = 1.9 \times 10^{-4}$$
$$BR(B \rightarrow \mu^+\mu^- K^{\pm}) = 1.5 \times 10^{-4}.$$

At the **Mark II** detector at SLAC [39], researchers determined the limit

$$B \rightarrow \mu^+\mu^- K^{\pm} < 6.4 \times 10^{-3}.$$

In 1989, **ARGUS** limits on Rare B decays were [40]

$$BR(B \to \mu^+ \mu^- K^\pm) \quad < \quad 2.2 \times 10^{-4}$$

$$BR(B \to \mu^+ \mu^- K^{0*}) \quad < \quad 3.4 \times 10^{-4}.$$

3.7   Form Factor Calculations

During 1990, a flurry of papers came out to contend for the best solution to the problem of the form factors. This was in addition to the papers already discussed. The form factors model all the unknown binding of the quarks in the mesons as well as the QCD effects. The exact algebraic structure of these factors had long been disputed. They are the major theoretical difference between otherwise identical standard model predictions for the rate. Though some of the authors in this section worked out both the non-resonant decays and the long distance effects, here I only present the non-resonant rates so that it is easier to compare the results.

First, the form factors of **Bauer, Stech and Wirbel** [27] were applied to this decay mode by Deshpande and Trampetić in their 1988 paper [25]. The Bauer, Stech and Wirbel (sometimes called the single pole dominance) results were widely tested and showed reasonably good agreement with semileptonic and hadronic data. Later, Dominguez, Paver and Riazuddin [41] compared it to their own method, and in so doing performed a more complete calculation of the QCD corrections with the Bauer, Stech and Wirbel form factors than

Deshpande and Trampetić had. These new results can be compared to the inclusive $b \to l^+ l^- s$ calculation, which doesn't contain form factors.

$$BR(b \to l^+ l^- s) = 14 \times 10^{-6}$$
$$BR(B \to l^+ l^- K^{*0}) = 1.0 \times 10^{-6}$$
$$BR(B \to l^+ l^- K^{\pm}) = 1.6 \times 10^{-7}$$

Dominguez, Paver and Riazuddin [41] applied the "general vector meson dominance" method and added QCD corrections as done by Grinstein, Savage, and Wise [29] and Grigjanis, O'Donnell Sutherland and Navelet [29, 30, 31]. This vector meson dominance approach was different from those used by the other authors in this section. The branching ratio extimates are 15 to 20% higher than the single pole dominance results at a top quark mass of 150 GeV/c². The vector meson dominance form factors give the following results, where the rate for $b \to l^+ l^- s$ doesn't include form factors.

$$BR(b \to l^+ l^- s) = 14 \times 10^{-6}$$
$$BR(B \to l^+ l^- K^{*0}) = 1.5 \times 10^{-6}$$
$$BR(B \to l^+ l^- K^{\pm}) = 2.6 \times 10^{-7}$$

Jaus and Wyler [42] present their calculations of these rare decays using

hadronic matrix elements by Jaus [43], or the *light-front* formalism. They use the QCD corrections derived by Grinstein, Wise and Savage [29] and Grigjanis, O'Donnell, Sutherland and Navelet [29, 30, 31]. Their full QCD calculation yielded rates a factor of four smaller than Deshpande and Trampetić. They used a top quark mass of 150 GeV/c^2 to calculate their results. At a top quark mass of 180 GeV/c^2, the results are a factor of 1.5 higher than these.

$$BR(B \rightarrow \mu^+\mu^- K^{*0}) = 5.0 \times 10^{-7}$$
$$BR(B \rightarrow \mu^+\mu^- K^{\pm}) = 3.0 \times 10^{-7}.$$

Isgur and Wise developed their form factors for heavy quark effective theory (HQET) in three papers [44, 45, 46], but they left the calculation of the exact rate to Ali and Mannel [47]. Ali and Mannel assumed that the s quark in the final state was heavy enough to apply HQET. They mentioned that this is a bad assumption. The Isgur-Wise function was intended for situations where one quark in the meson is much heavier than the others, and where the heavy quark has a mass much greater than the QCD scale. These conditions are necessary for mesons in both the initial and final states [48]. They'd like to see someone work out the leading order corrections in the effective field theory approach so that they can update the work later. As a check, they calculated the rates for the semileptonic decay $D \rightarrow K l \nu$ to see that the approximation was good to within a factor of two and presumed that the same would be true of the rare decay calculation as well. They used two parameterizations of the Isgur-Wise function, I) a polynomial fraction, and II) an exponential. The

45

results were for top quark mass of 100 GeV/c^2. For top quark mass of 200 GeV/c^2, multiply $BR(B \rightarrow \mu^+\mu^- K^\pm)$ by 3.0 and $BR(B \rightarrow \mu^+\mu^- K^{*0})$ by 2.5. For model I,

$$BR(B \rightarrow \mu^+\mu^- K^{*0}) = 1.2 \times 10^{-6}$$

$$BR(B \rightarrow \mu^+\mu^- K^\pm) = 2.5 \times 10^{-7}.$$

For model II,

$$BR(B \rightarrow \mu^+\mu^- K^{*0}) = 1.0 \times 10^{-6}$$

$$BR(B \rightarrow \mu^+\mu^- K^\pm) = 1.1 \times 10^{-7}.$$

In a 1993 paper, **Baillie** [33] expanded on Ali and Mannel's work to derive the ratio of the branching ratios for the resonant decays and the non-resonant decays in a portion of the dimuon mass spectrum. He uses the same HQET approach to his calculation, though he expresses reservations about using HQET in this case unless calculating a ratio of decay rates due to the light mass of the "heavy" quarks. He defines a resonant ψ to have dimuon mass between 3.08 and 3.12 GeV/c^2, and a non-resonant dimuon pair to have a mass between 3.12 and 3.66 or 3.73 and 4.6 GeV/c^2. For a top quark mass of 175 GeV/c^2,

$$\frac{BR(B \rightarrow \mu^+\mu^- K^{*0})}{BR(B \rightarrow \psi K^*, \psi \rightarrow \mu^+\mu^-)} = 0.002$$

$$\frac{BR(B \rightarrow \mu^+\mu^- K^\pm)}{BR(B \rightarrow \psi K^\pm, \psi \rightarrow \mu^+\mu^-)} = 0.002$$

UA1 presented limits on rare B meson decays in 1991 [49], [50].

$$BR(B \to \mu\mu X) \quad < \quad 5.0 \times 10^{-5} \text{ at } 90\% \text{ CL}$$

$$BR(B \to \mu\mu K^*) \quad < \quad 2.3 \times 10^{-5} \text{ at } 90\% \text{ CL}.$$

With the choices for form factors neatly laid out, physicists turned to more standard model extensions. In their comprehensive 1991 paper, **Sher and Yuan** [51] looked into a neutral Higgs boson extension to the standard model wherein the Higgs boson has small couplings with the quarks. They look at a great many rare decay modes and advocate experimental research on them. They also use the existing research limits to put stringent constraints on non-standard model couplings.

In a recent paper, **Deshpande, Panose and Trampetić** [52] calculated the effect of two different extended Higgs models on the rates of $b \to sl^+l^-$ and the effect that a heavy top quark mass might have on the branching ratio. They find that the branching ratio rises dramatically with most variations in the Higgs models as well as with the top quark mass. They use (then) current experimental limits [49] to rule out portions of the Higgs model theories.

3.8 Asymmetry in Muon Polarization

Once experimental measurements of the branching ratios of $B \to \mu^+\mu^- K^\pm$ and $B \to \mu^+\mu^- K^{*0}$ are made, three papers advocate a study of the polarization of the decay products as a function of dilepton mass. That the polarization is a

function of the lepton mass is about all these authors agree on. **A. Ali, T. Mannel, and T. Morozumi** [37] measure the angle between the positively charged lepton and the B meson in the dilepton center of mass, θ, as **Çakir** [53]. They both use Heavy Quark Effective Theory to do their calculation, however their results are different. Çakir sees the variation of the amplitude as a physics factor times the quantity $(1 - \alpha(s)\cos^2\theta)$, where α is a function of the dimuon invariant mass squared. Ali, Mannel and Morozumi, on the other hand, see terms in $\cos\theta$ which are asymmetric about the origin, vary as a function of dimuon mass, and vary as a function of top quark mass. They find the resonance polarizations to be symmetric. Since Ali, Mannel and Morozumi see this asymmetric component to the polarizations, they propose a counting experiment. In the dilepton center of mass of the system, they expect to see more positively charged muons going in the direction of the B meson than away. This is in the non-resonant dimuon case only, and this effect is modeled in the RareB Monte Carlo, discussed in the next chapter.

Gourdin took a different approach [54]. He concerns himself with the angle between the two leptons in the B center of mass frame. This makes it difficult to compare his results to those of the previous authors. However, he doesn't see a dependence of his polarization asymmetry on the mass of the top quark as Ali does.

After observing the decay $b \rightarrow s\gamma$, **CLEO** went on to establish the most stringent limits on all the rare B decay modes to date in their 1994 article [55].

Using 2.03 fb^{-1}, or 2.17 million $B\overline{B}$ pairs, they place the limits

$$BR(B \to \mu^+\mu^- K^{*0}) \quad < \quad 3.1 \times 10^{-5} \text{ at } 90\% \text{ CL}$$

$$BR(B \to \mu^+\mu^- K^{\pm}) \quad < \quad 0.9 \times 10^{-5} \text{ at } 90\% \text{ CL.}$$

This theory of rare B decays is embodied in the Monte Carlo RareB. It also sets the stage for work with the limits from this analysis. I will use the limits to constrain the charged Higgs theories, anomalous couplings of the W boson, and fourth generation.

Authors	$BR(B \to \mu\mu s)$	$BR(B \to \mu\mu K^{\pm})$	$BR(B \to \mu\mu K^{*0})$
Hou, Willey & Soni	1.0×10^{-5}		
Deshpande & Trampetić	2.0×10^{-5}	2.0×10^{-6}	8.0×10^{-7}
Bauer, Stech & Wirbel	1.4×10^{-5}	1.0×10^{-6}	1.6×10^{-7}
Dominguez, Paver & Riazuddin	1.4×10^{-5}	1.5×10^{-6}	2.6×10^{-7}
Jaus & Wyler		5.0×10^{-6}	3.0×10^{-7}
HQET I (Ali & Mannel)		2.3×10^{-6}	4.4×10^{-7}
HQET II (Ali & Mannel)		1.9×10^{-6}	1.9×10^{-7}

Table 3.1: Summary of theoretical predictions of branching ratios for rare B decays of interest.

Chapter 4

The RareB Monte Carlo

Program

The RareB Monte Carlo models the decays $B \to \mu^+ \mu^- K^\pm$ and $B \to \mu^+ \mu^- K^{*0}$ to make the connection between theoretical calculations and experimental expectations. It produces the momenta for a B meson and its rare decay products according to the most recent, accurate models. G. Baillie wrote subroutines to calculate the amplitude of the decay, $|M|^2$ (not including the phase space factors). I surrounded this work with the kinematic calculations (phase space) and Monte Carlo generation code. Additional input was given by F. DeJongh and S. Vejcik.

None of the existing event generating Monte Carlo programs can calculate the correct distribution of events necessary for this study of rare B decays without modification. Though it is possible to modify ISAJET, for example [50], to produce the non-resonant events, adding the long-distance resonance

effects is impossible without rewriting a large portion of the program, as shown below. Unlike the large packages ISAJET and HERWIG, RareB doesn't produce an underlying event. However, it allows a flexibility with the production model that these packages don't allow, and it is very fast.

4.1   B Production

The RareB Monte Carlo can get its information on b quark production and decay from any outside source. In this analysis, that outside source is a parameterization of Nason, Dawson and Ellis's calculation [56] of the b quark production cross-section combined with Peterson fragmentation [57]. This was programmed by Richard Hughes [58]. He parameterized the calculated cross-section in a histogram of 299 0.2 GeV/c wide p_t bins, and assumed the distribution is flat in rapidity between 0.0 and 1.0. The shape of the cross-section versus p_t curve is shown in figure 4.1.

4.2   B Decay

G. Baillie used Heavy Quark Effective Theory with the form factors of Isgur and Wise to construct the matrix elements used here. Basing his work on that of Ali, Mannel and Morozumi [37], he included the polarization and asymmetry in the polarization, as well as long-distance ψ and ψ' effects (optional). The form factors are defined in a modular fashion so that it is easy to replace them. All of the basic physics constants used are defined in convenient structures so

that they can be adjusted prior to compiling the code. Some parameters can be changed at run-time. In addition to the event type, it is most important to choose whether the events should be generated according to phase space alone and the matrix element weight recorded, or whether the events should be generated with a frequency proportional to matrix element times the phase space factor. In addition to these choices, the following parameters can be changed at run-time:

the random number seed,

the maximum number of iterations for the throw-away method,

the minimum p_t of the b quark,

long distance resonance effects on or off,

mass of the top quark,

Λ_{QCD},

$\Delta\kappa$, the anomalous magnetic moment of the W.

4.3   Specific Technical Details

The method of generating the events is a combination of a *throw-away* (acceptance-rejection) method and an *integration* method. A *throw-away* method is defined as follows: To find the area under a function $f(x)$, generate a random number x between x_{min} and x_{max} and a random number y between y_{min} and

y_{max} (*i. e.* within the bounding box). Calculate $f(x)$. If $y \leq f(x)$, it is a *good* event. Discard bad events.

If N_{good} is the number of events in the set of good events, the area under the function is

$$\int f(x)\,dx = \frac{N_{good}}{N_{good} + N_{bad}} \times (y_{max} - y_{min})(x_{max} - x_{min}).$$

The uncertainty, σ, of $\int f(x)\,dx$ is

$$\sigma = \sqrt{\frac{1}{N_{good}} + \frac{1}{N_{good} + N_{bad}}}$$

This is the simplest example of a throw-away method; it integrates the function $f(x)$. In the same way, if $f(x)$ is a probability distribution function, the set of good events is said to have been generated with a frequency proportional to the the amplitude of the probability distribution function. This method can be used for functions of any number of variables, but is inefficient where the function is spikey. It is best to use this method when the area below the curve is about equal to the area above the curve inside the bounding box.

The *integration* method can be used to generate events with a frequency proportional to the amplitude of a function $f(x)$ if $f(x)$ is integrable;

$$F(x) = \int f(x)\,dx.$$

$F(x)$ is monotonic and increasing between x_{min} and x_{max}, so there exists an inverse, F^{-1}, of the function F such that if $y = F(x)$ then $F^{-1}(y) = x$.

Presuming one can calculate the inverse, choose random numbers y between $F(x_{min})$ and $F(x_{max})$, calculate $x = F^{-1}(y)$, and the set of all values of x are randomly generated events with a frequency proportional to the amplitude of the function $f(x)$. This method is useful only for distribution functions of one variable.

The RareB Monte Carlo uses a combination of these two methods. The decay amplitude depends on eight variables (six in the case of $B \rightarrow \mu^+ \mu^- K^{\pm}$):

1. dimuon invariant mass

2. K^* mass

3. angle between ψ (or K^*) and the direction of the B boost (two angles in the B rest frame).

4. angle between K and the K^* boost (two angles in the K^* rest frame).

5. angle between μ^+ and the ψ boost (two angles in the ψ rest frame).

These variables are each involved in two probability distribution functions which I compute separately and then combine at the end. The two distributions are the $|M|^2$ distribution and the phase space distribution. Together the two distributions contain the results of the calculation of the Feynman diagrams for the decay, as discussed in chapter 3. The $|M|^2$ distribution contains the resonance information and the polarization information which are specific to this particular process. The phase space distribution contains the generic angular distribution information which all three or four body decays have in

common. For each decay mode, the code produces events with a frequency proportional to the amplitude of the phase space distribution times $|M|^2$. The phase space factor is calculated using a throw-away method, and the $|M|^2$ factor is calculated using a combination of an integration and a throw-away process.

To generate events distributed with a frequency proportional to the phase space factors alone, the code chooses a random number between $(2m_\mu)^2$ and $(m_B - m_{K^*})^2$ for the dimuon mass squared. Then it randomly generates the angles of the decay products of the B and transforms them to the B center of mass frame. It calculates the $|M|^2$ as a function of these input values and records it for the user's benefit. No changes or cuts happen as a result of the $|M|^2$ calculation in the RareB program. In addition, the phase space function of the generated variables is compared to a random number and the event thrown away if the random number lies above the phase space function value.

To generate events distributed with a frequency proportional to the phase space factors times $|M|^2$, I perform a fast integration Monte Carlo before using the throw-away technique. This is especially important if the long-distance effects are to be included, as the throw-away method is extremely inefficient in this case. I constructed an enveloping histogram which has variable bin size and lies above the $|M|^2$ curve for all reasonable values of the seven variables of interest (the K^* mass is handled separately). The bin heights come from integrating $|M|^2$ using a Monte Carlo method, and recording the area and the maximum value for each bin. The uncertainty of the bin area for each of the

1000 bins is less than 10%, except in the vicinity of the ψ peak, where it is less than 1%. This proceedure isn't completely efficient; 3% of events have values of $|M|^2$ which are larger than the envelope and are discarded. This small inefficiency is completely offset by the factor of 10^{10} reduction (!) in CPU time required for this combination method compared to the throw-away method. For each event, the code chooses a bin according to the integration method. Within the bin, the code then uses the throw-away method on the funciton of the phase space factors times $|M|^2$.

In addition to the variables enumerated above, the K^* mass width is modeled with a Breit-Wigner corrected for relativisic effects and the four-body phase space effects. Since the mass of this meson has no effect on the $|M|^2$ of the decay, it is generated separately. No other masses are assigned discernable widths.

4.4   Results

The RareB Monte Carlo is both fast and accurate. It is most realistic in terms of the matrix elements used. Figures 4.2 and 4.3 imitate theory curves calculated by G. Baillie. In chapter 7 I use RareB to define cuts and efficiencies for the analysis.
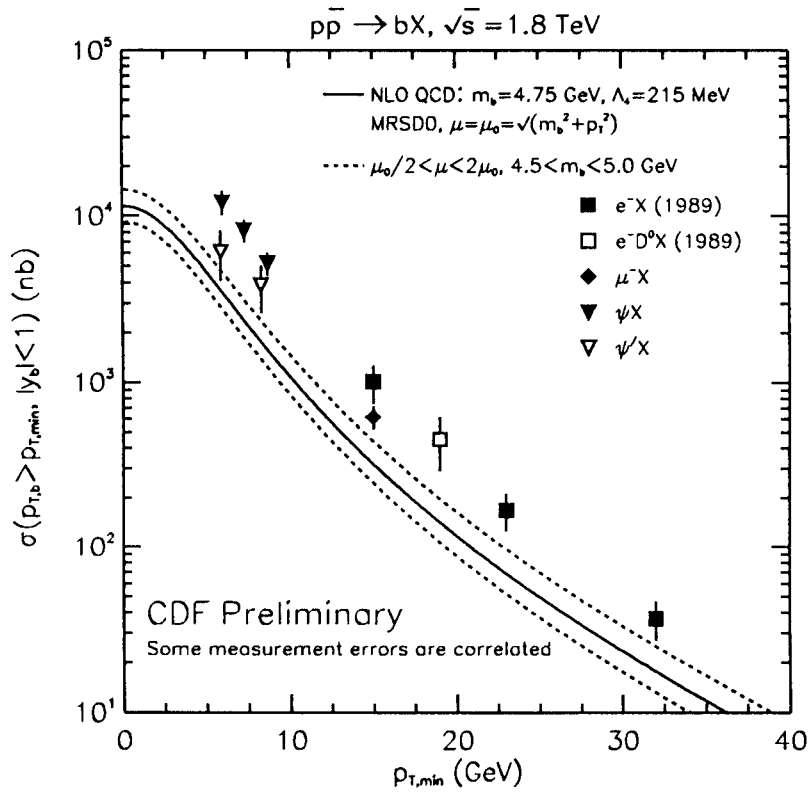
Figure 4.1: Cross-section versus p_t for B production at CDF. Line is theoretical prediction and points are CDF data points for various decay modes as shown.
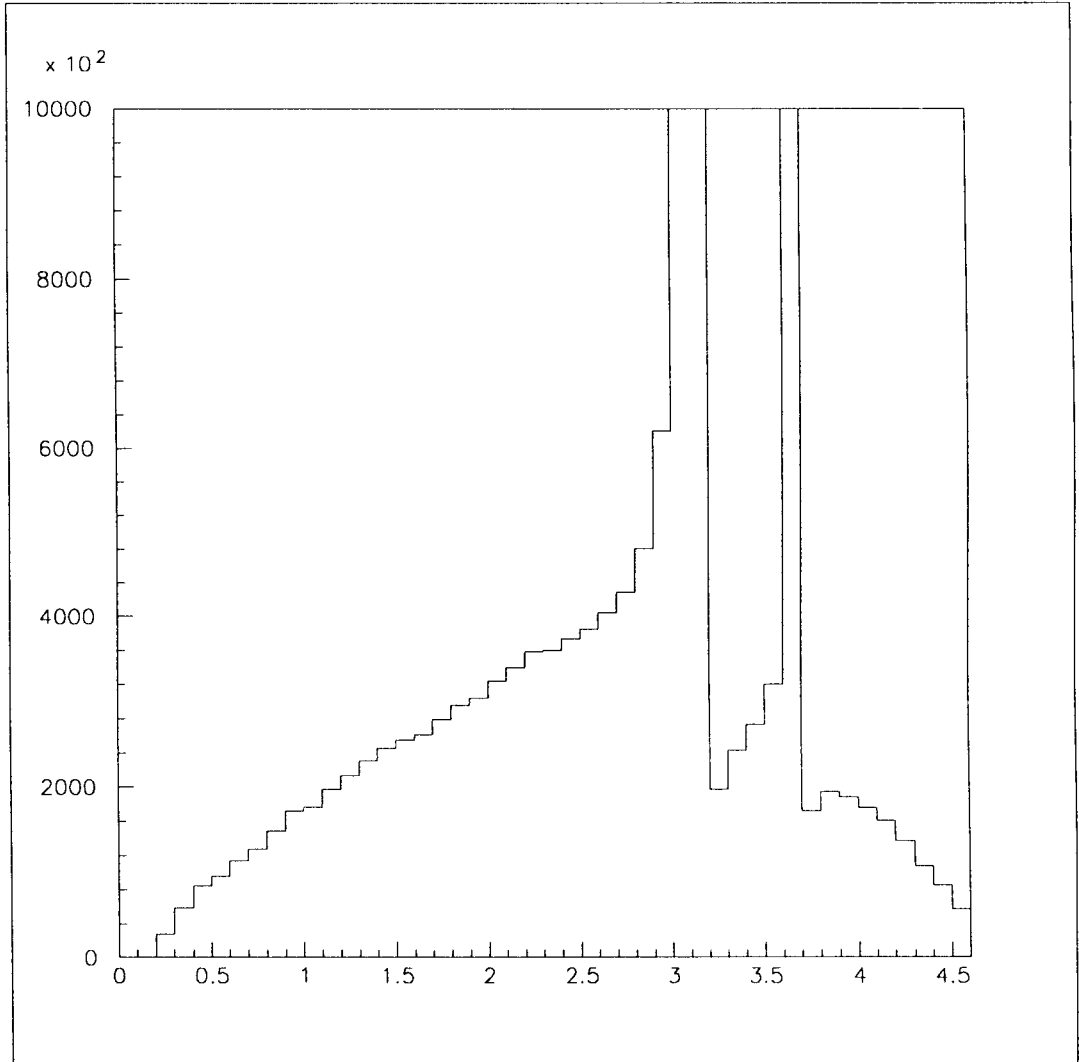
Figure 4.2: Dimuon mass spectrum for the decay $B \rightarrow \mu^+\mu^- K^\pm$, where the long-distance effects are evident ψ and ψ' peaks.
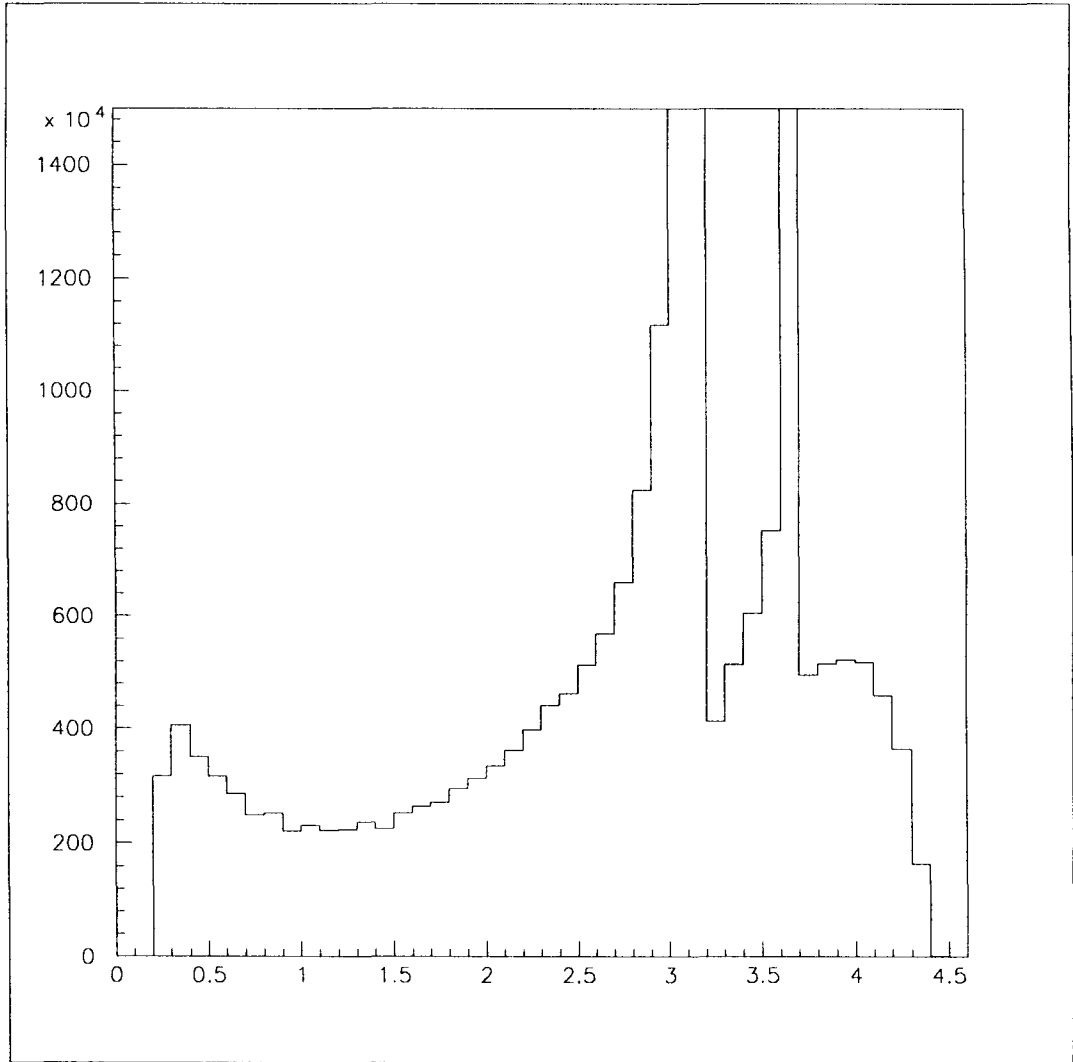
Figure 4.3: Dimuon mass spectrum for the decay $B \to \mu^+\mu^- K^{*0}$, where the long-distance effects are evident ψ and ψ' peaks.

Chapter 5

The Experimental Apparatus

5.1 The Tevatron

Currently, Fermilab houses the highest energy accelerator in the world, colliding protons and antiprotons at a center of mass energy of 1.8 TeV. The facility can be run in fixed target or in colliding beam mode. CDF (The Collider Detector at Fermilab) is a colliding beam experiment.

The beam begins as hydrogen gas. It is negatively ionized (an electron added) and accelerated in a Cockroft-Walton accelerator to 750 keV. Then the two electrons are stripped off and the protons pass through the linac (a linear accelerator) in bunches. The linac accelerates them to 200 MeV and injects them into the small Booster Ring, which accelerates the bunches to 8 GeV so that they can be injected into the Main Ring. The Main Ring accelerates the protons to 150 GeV, and passes them on to the Tevatron which accelerates the protons with superconducting electromagnets to their final energy of 900 GeV
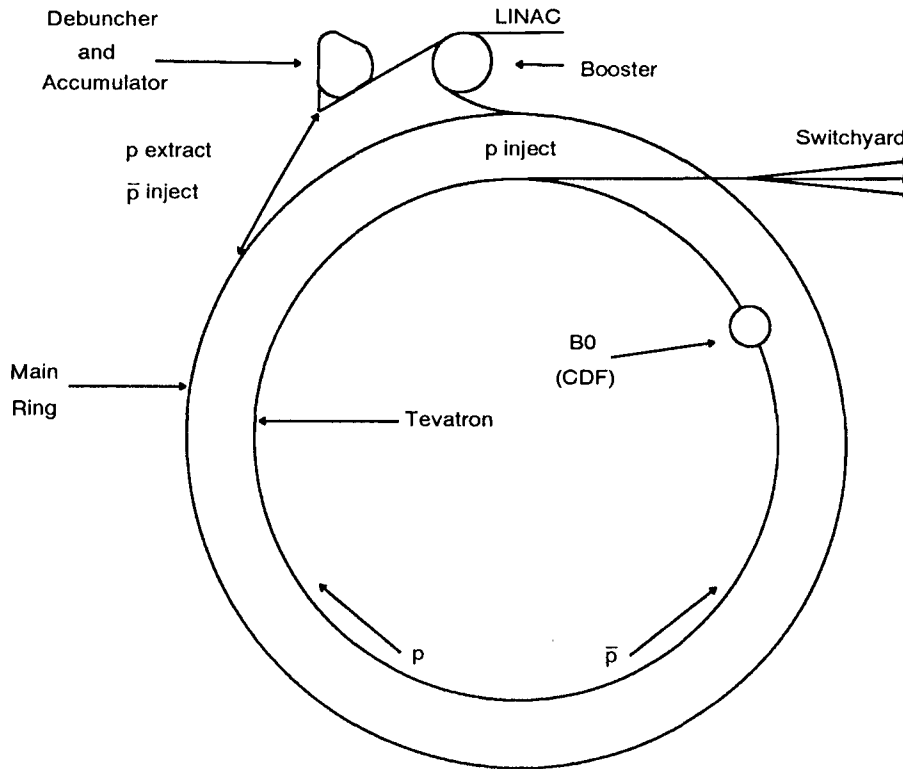
Figure 5.1: Beamlines at Fermilab, including the linac, Booster, Main Ring, and Anti-proton storage ring.

(or 0.9 TeV) at which point they collide with antiprotons of the same energy and opposite direction.

The Cockroft-Walton, linac, and Booster Ring are all located around Wilson Hall. The Main Ring and the Tevatron share a tunnel below the distinctive earth berm four miles in circumference which dominates the Fermilab landscape. The antiproton storage ring, discussed below, is about the same size as the Booster Ring.

The Main Ring has two responsibilities in colliding beam operation. First,

it is used to accelerate the proton bunches to 150 GeV for injection into the Tevatron. Second, it is used to accelerate protons to 120 GeV in order to slam them into a tungsten target to create antiprotons.

Right after the antiprotons come off the tungsten target, they go through a complicated set of steps in a matter of 2 seconds. With an average 8.5 GeV of energy, the antiprotons travel through a lithium lens into a debuncher ring. It cools the beam stochastically and uses bunch rotation techniques to reduce the energy spread and transverse motion of the antiprotons. Then the antiprotons are sent off to the accumulator.

The accumulator stores antiprotons until there are enough collected to start the colliding beam in the Tevatron. It can take eight hours or more to make enough antiprotons for an effective run, that is, for a good sized "stack" of approximately 10^{12} antiprotons. When it is time, the antiprotons are cooled, bunched, and injected into the main ring and then into Tevatron.

First the Main Ring injects six bunches of protons into the Tevatron. Then one at a time, the antiproton accumulator sends six bunches of antiprotons into the main ring, which accelerates them from 8 GeV to 150 GeV and injects them into the superconducting Tevatron. When all twelve bunches are in place in the Tevatron at 150 GeV, they are accelerated to 900 GeV. The high-energy beams are kept in the 1 km radius circle using 4.4 T superconducting magnets.

At 900 GeV, the beam is messy with protons orbiting just outside the acceptable radius, so the errant edges of the bunches are scraped off using collimators. It is monitored during the time it is in the ring to make sure it

remains within the center of the beam pipe and doesn't damage the detector. If for some reason something goes wrong, it is quickly dumped (within 3.1 μs) into the beam dump to avoid problems.

The Main Ring is usually run at the same time as the Tevatron so that "stacking" of antiprotons won't interupt data-taking. In a typical 1991 run, after all the stacking, cooling, injecting and scraping, there were 7×10^{10} antiprotons and 20×10^{10} protons per bunch. Usually the tuning of the beams made a luminosity of 10×10^{30} cm^{-2}s^{-1}, or 50,000 events per second.

5.2   The CDF Detector

The Collider Detector at Fermilab [59] is built to study these 1.8 TeV center of mass energy collisions. It is a general-purpose solenoidal detector azimuthally and forward-backward symmetric about the collision center, finely segmented in both pseudorapidity and ϕ angle around the beampipe. The superconducting solenoid produces a 1.4 Tesla magnetic field useful for determining charge and momentum of charged particles.

It is useful to have in mind the CDF standard coordinate system as we discuss the geometry of the detector. Protons come into the B0 collision hall from the West and antiprotons from the East. It is natural to assign the proton beam as the positive z axis, the vertical as the y axis, and the radial out from the center of the Tevatron as the x axis, as required by a right-handed coordinate system. ϕ is measured from the x axis counterclockwise around the
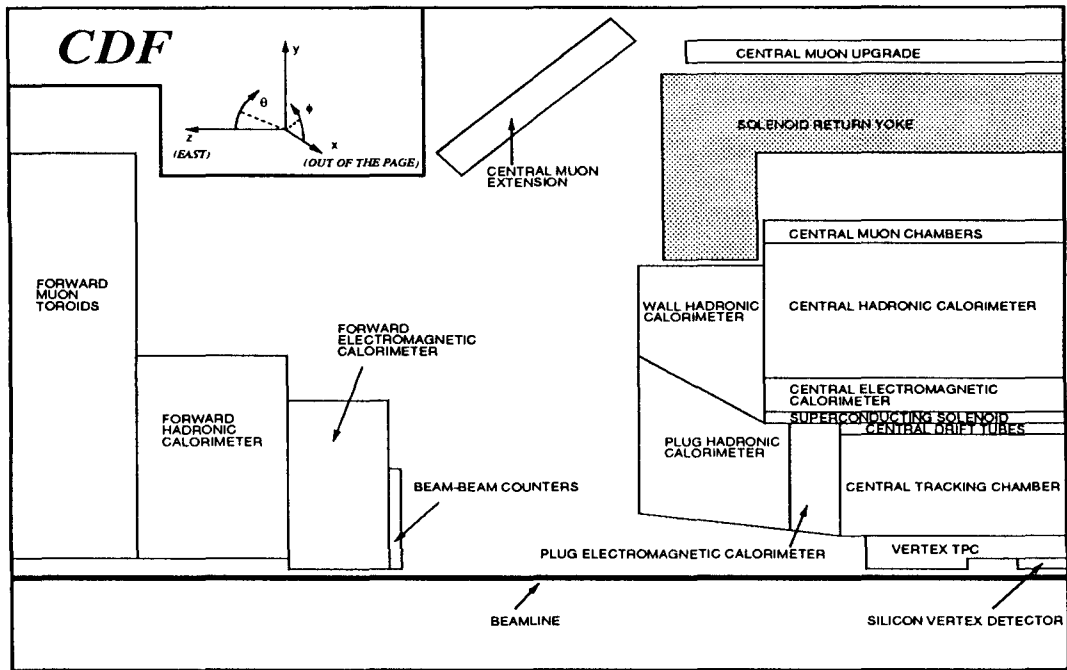
Figure 5.2: r-z crossection view of the CDF detector as it was configured for the 1992 data-taking run.

z axis, and θ from the positive z axis. Pseudorapidity is defined

$$\eta = -\log\left(\tan \frac{\theta}{2}\right).$$

CDF is arranged in three sections, the central section, the plug, and the forward chambers. The forward chambers are fixed in the collision hall, but the central and plug regions, moving as a unit, can be brought into the assembly area for easy access. The tracking chambers are closest to the beampipe to provide information on the single particle level. Further out, calorimetry sums the energy from the particles to show the topology of the energy distribution as a function of solid angle.

64

A particle, say a 4 GeV muon coming from the collision vertex and traveling within the central region (± 0.6 in pseudorapidity), would first enter the Silicon Vertex Chamber (SVX), then pass through the Vertex Tracking Chamber (VTX), the Central Tracking Chamber (CTC), the solenoidal magnet, the Central Electromagnetic Calorimeter (CEM), and would continue through the Central Hadronic Calorimeter (CHA), the Muon Chambers (CMU), through an iron wall, and through the Central Muon Upgrade (CMP).

If the particle is traveling forward of perpendicular ($0.6 < \eta < 1.1$), it would still go through the tracking chambers but would encounter the End-wall Hadronic Calorimeter and then continue to the Central Muon Extension (CMX).

A very forward-going particle ($\eta > 1.1$) is beyond the scope of this analysis. It misses most of the tracking, heading instead for the Plug Electromagnetic and Plug Hadronic Calorimeters (PEM, PHA) or Forward Electromagnetic and Forward Hadronic Calorimeter (FEM, FHA), and the Forward Muon Chamber (FMU). The most forward edge of the forward calorimeter has pseudorapidity 4.2.

Descriptions of particular subsystems follow.

5.2.1 SVX – Silicon Vertex Detector

The SVX is a very small tracking chamber deposited on silicon chips[60]. The strips are p-type deposits in narrow lines very close together. Ionizing particles passing through the silicon bump electrons into the conduction band of the

65
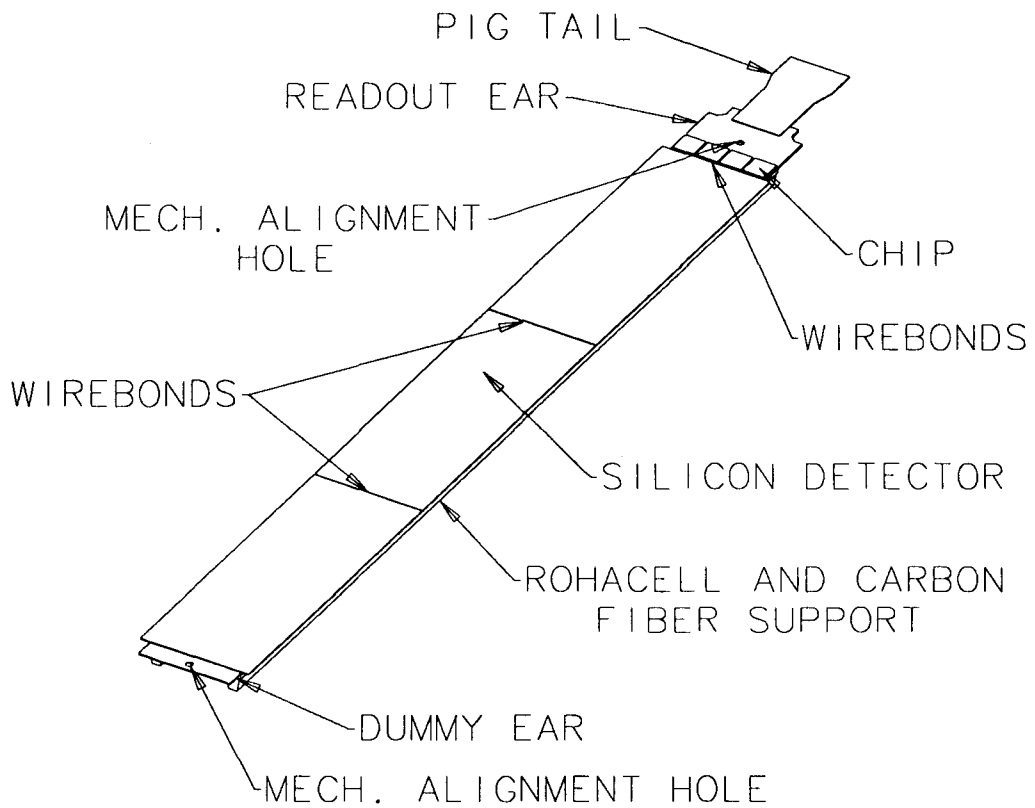
Figure 5.3: A single SVX ladder.

semiconductor, where the high electric field draws them to a strip. The strip suffers a voltage drop proportional to the amount of original ionization. The chamber heats up with the current through the electronic readout, so a good portion of the detector construction was dedicated to cooling the chamber. The detector is 51 cm in length, and so contains about 60% of the collision vertices. The detector is constructed of lightweight materials to reduce as much as possible the number of tracks which decay in the material of the SVX.

The SVX consists of two barrels; each barrel has twelve 30° ϕ slices; each

ϕ slice or *wedge* has four layers called ladders. These ladders are 25.5 cm long and constructed of three silicon detectors wire-bonded together. Each ladder has more conducting strips on it than the ladder inside it. There are 128 strips on each inner ladder, and 768 on each outer ladder. Ladders are attached to composite backing (polyanaciline foam, epoxy and carbon fiber strips), and the ends are attached to beryllium ring bulkheads. The ladders send their signals out through an attached readout chip to level 3 of the trigger to be used for offline analysis.

For events where the primary vertex lay within the fiducial volume of the SVX (± 25.5 cm), the SVX was used to calculate the $x - y$ position of the primary vertex. These coordinates were calculated very precisely by the code using the SVX, with an overall uncertainty of only 40 μm. In figure 5.4, created by Hans Wenzel, CDF, plot 1 is the variation of the primary vertices with respect to the calculated beam position. It reflects the intensity profile of the beam, a Gaussian, circular profile. Plot 2 is a projection of of the first plot in the x direction, fit to a Gaussian. The function is centered at zero and has a σ of 40 μm. Plot 3 shows the distribution of the primary vertex in the beam pipe. The vertical axis of the plot is the detector x axis, and the horizontal axis is the detector z axis. The uncertainty of measuring the beam position of a run is dominated by the beam spread, $\sigma = 36$ to 38 μm. The uncertainty of the measurement of an event vertex has a σ of 15-16 μm. Together these effects account for the 40 μm uncertainty in the primary vertex position [1].
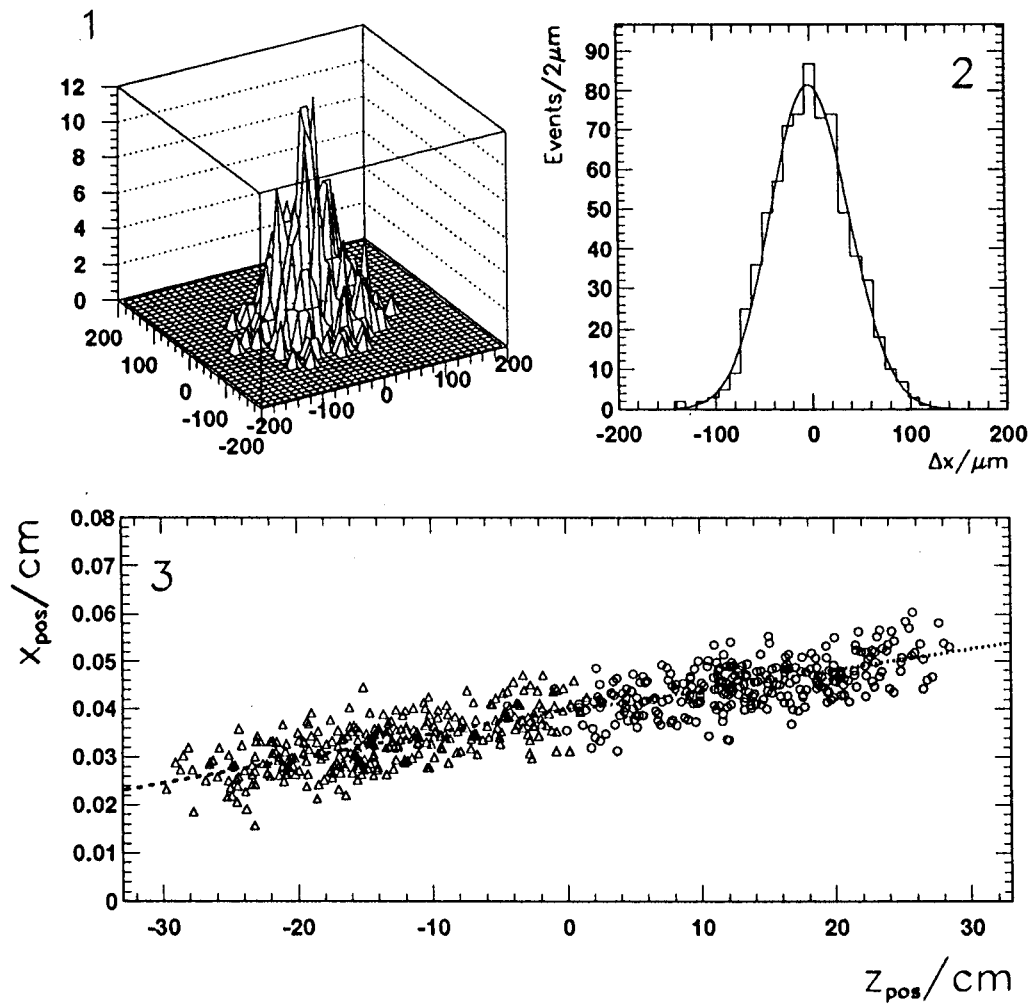
Figure 5.4: Position and resolution of the primary vertex, as calculated from SVX data. Plots by H. Wenzel [1].

5.2.2 VTX – Vertex Tracking Chamber.

The VTX is a traditional proportional wire chamber [61]. The ionization trails of charged tracks are left in a gaseous mixture of 50% argon and 50% ethane bubbled through alcohol at -7° C, which fills the space between the wires and walls of the chambers. This same mixture is used in all the CDF chambers which require gas. The ionization trail is pulled apart in the high voltage (1900 V), and the electrons avalanche at the wires which measure the drop in voltage.

The VTX consists of eight octagonal modules to make a barrel around the SVX. The eight triangular sections of each module have straight wires between the two equilateral sides so that the wires circle the beampipe and form a plane perpendicular to the beam. In this way the detector accurately measures the z position (2 mm resolution) of the primary vertex, complementing the function of the SVX.

5.2.3 CTC – Central Tracking Chamber.

The CTC [62] is the main source of track parameter information at CDF. CDF's main design goals for the CTC were to measure the trajectories of high momentum tracks accurately, to identify and separate two closely spaced tracks inside particle jets, to identify energy directed toward cracks in the calorimetry, to find secondary vertices of the decays of long-lived particles such as K_s and Λ's, and to match tracks to shower centroids measured in the calorimeter.

The CTC surrounds and supports the VTX and SVX, and is housed inside the 1.4 Tesla solenoidal magnet. The barrel of the drift chamber has diameter of 2.76 m and length 3.2 m. (The solenoid is 5 m long.) The 36504 sense and field-shaping wires are each 3.2 meters long so there is no break at the center of the detector. It is a gas chamber using standard argon-ethane mixture.

The wires are arranged in 84 layers, subdivided into 9 superlayers, five axial and four stereo (3° tilt). The axial superlayers each have twelve layers of wires and are alternated with the stereo superlayers each of which have six layers of wires. The wires within a superlayer are grouped in measurement cells that run 45° to the radial (the Lorentz angle of drifting electrons in combined electric and magnetic fields), which keeps avalanche drift trajectories exactly azimuthal (along ϕ), while it introduces a slight charge asymmetry among the lowest energy reconstructed tracks. See figure 5.5. Voltage of the wires was finely tuned so as to have an even response and an even drift electric field of 1350 V/cm.

The resolution of the detector is

$$\frac{\delta p_t}{p_t} \approx 0.0011 \times p_t \tag{5.1}$$

$$\delta(r\phi) = 0.2mm \tag{5.2}$$

$$\delta z = 4mm \tag{5.3}$$

The maximum drift time in the chamber is about 800 ns. However, the drift time from a track to at least one wire in a superlayer is less than 40 nsec, which allows a fast track reconstruction at Level 2 of the trigger, discussed below.
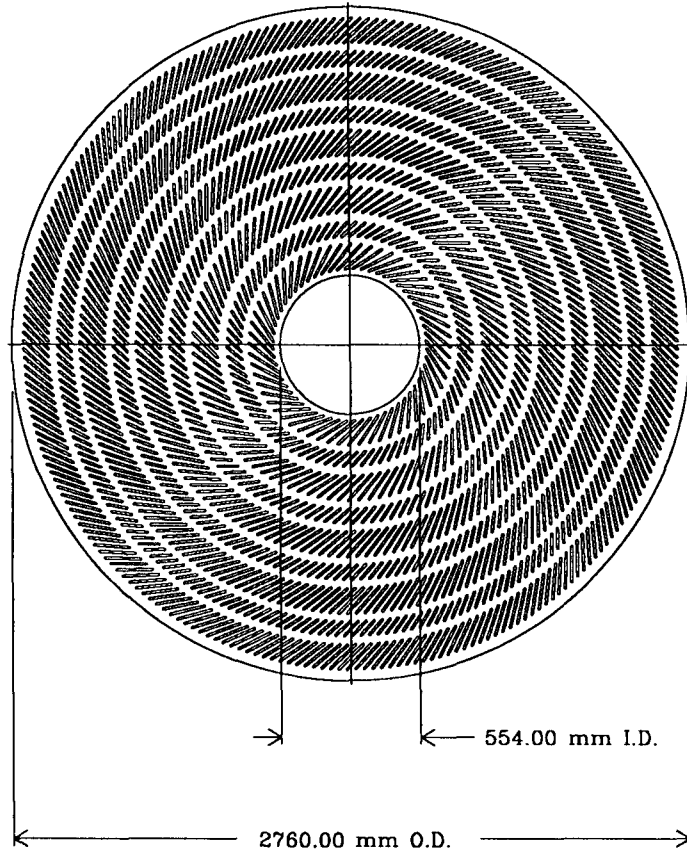
Figure 5.5: Diagram of the CTC endplate showing the layers of wires and the slanted planes of the tracking cells.

5.2.4 Calorimetry

All the calorimetry at CDF is sampling calorimetry [59]. Each detector system consists of layers of absorber material to precipitate showers, and layers of active material to react to the charged particles in the shower by emitting light or a voltage change. Every particle decays into collections of both charged and neutral particles. The energy of this particle (regardless of whether it is charged or neutral) is proportional to the number of charged particles in the shower, hence to the size of the signal. For neutral particles, the only measurement we can make of its energy comes from the calorimeters, though for charged particles the information provided by the CTC serves as a nice cross-check of the calorimetry calibration.

Tracking chambers can be overwhelmed by a large number of tracks in a jet, whereas a calorimeter records the spread and amount of the energy, providing a simple signature for high multiplicity events. Energy resolution in the calorimeters improves as the energy deposition increases, and the arrangement of the calorimeter in projective towers gives us an accurate geometrical picture of the energy patterns at the primary vertex of the event.

CDF has extensive calorimetry in the central, plug and forward regions. In the central region, there are four moveable arches making two barrels split at zero in z and at $\pm\frac{\pi}{2}$ in ϕ. Central calorimetry covers -1.1 to 1.1 in η, or 120° to 30° in θ. The plug calorimetry extends from 1.1 to 2.4 in η, or 36° to 10° in θ. The forward calorimetry runs from 2.2 to 4.2 in η (10° to 2°).

Each calorimeter consists of two parts, electromagnetic and hadronic. Elec-

trons and photons shower early in the calorimeter, so it is important to use thin high-density metal as the absorber and use thin layers for accurate resolution of the shower. Hadrons interact deeper in the calorimeter, so thick layers of absorber material help increase the density and decrease the size of the hadronic calorimeter, with a corresponding decrease in resolution. Calibration of all the calorimeters was done at the test beam, though the shift crew calibrated all of the electronics every eight hours or so throughout the run.

Central Calorimetry The central calorimeter uses scintillating polystyrene as the active material. It reacts to the presence of ionizing radiation by emitting light. This blue light is collected in acrylic doped with waveshifter and piped though clear acrylic lightguides to photomultiplier tubes on the outside of the wedges.

Alternating layers of polystyrene and metal make up the projective towers of 15° wedges, which are arranged in two barrels of twenty-four wedges. The two barrels come together at $z = 0$. They are also split vertically along the beam pipe so that the tracking chambers inside can be accessed for repairs. Each of the 24 wedges covers 15° in ϕ and has ten projective towers in it, each measuring .1 in η, making the central coverage -1.1 to 1.1 in η. The CEM, CHA, and CMU are housed together in each wedge. The central calorimeters also include the endwall calorimeter modules, which are imbedded in the steel supporting the magnet and CTC. See figures 5.2 and 5.7.

The CEM (central electromagnetic calorimeter [63]) is the inside 31 layers

of 0.32 cm thick lead alternated with 0.5 cm thick layers of (polystyrene) scintillating plastic. It is 18 radiation lengths thick and has a resolution of

$$\frac{\sigma_E}{E} = \frac{13.5\%}{\sqrt{E sin\theta}} GeV.$$

The resolution was measured with test beam electrons and pions. The CES (Central Electromagnetic Strip Chamber) is located 6 radiation lengths into CEM. The strip chambers accurately measure the position of the shower using proportional wires orthogonal to cathode strips to get profile views of the shower.

The CHA (Central Hadronic Calorimeter [64]) is the outer layers of the central calorimeter. Hadronic particles make it through the CEM and shower in the CHA. The CHA has 32 layers of 2.5 cm thick steel plates with 1.0 cm of plastic (acrylic) scintillator between them. The light is piped to its own set of photomultiplier tubes. The resolution of the detector is

$$\frac{\sigma_E}{E} = \frac{80\%}{\sqrt{E sin\theta}} GeV$$

as measured with test beam pions.

The endwall hadronic calorimeter covers the range in θ from 30° to 45° and 135° to 150°. The modules plug into cavities in the CDF magnet yoke and serve as part of the flux return path. The support system for the endwall also supports the CTC structurally. The endwall uses the same projective geometry and readout by scintillating plastic guides.

Plug Calorimetry The plug is located just outside the CTC in z, along the beampipe. It fits neatly into the endwall support structure, plugging the CTC sized hole at the end. It has a projective tower design and uses the argon-ethane gas mixture for the active medium. The calorimeter measures gas ionization as particles pass through it by accelerating the ionized particles toward anode wires in a high voltage and causing an avalanche of secondary electrons to do the same. For each primary electron, approximately 10^5 secondaries are produced under normal CDF operating conditions, the ratio of secondaries to primaries being known as the gas-gain.

Each PEM (Plug Electromagnetic [65]) detector is a torus, 2.8 m in diameter and 50 cm deep. It covers the η region from 1.1 to 2.4, or θ from 10° to 36°. It consists of 34 layers of conductive plastic proportional tube arrays interleaved with 2.7 mm thick lead absorber. The cathode readout is pads and strips etched on the printed circuit boards, which makes for a finely segmented projective tower geometry. At the shower maximum (depth in the calorimeter at which the shower is at its widest spread) the pads are much more finely segmented with layers of small drift tubes so that shower profiles can be done accurately as were done in the central region. Test beam studies with 100 GeV electrons determined that the resolution of the PEM and the FEM is

$$\frac{\sigma_E}{E} \sim \frac{28\%}{\sqrt{E}} GeV$$

The PHA (Plug Hadronic Calorimeter) lies just outside the PEM. It is cone-shaped to fit up next to the Endwall detectors. It is made of 20 layers

of proportional tubes alternated with 5.1 cm thickness iron plates. Detector resolutions for PHA and FHA are

$$\frac{\sigma_E}{E} \sim \frac{130\%}{\sqrt{E}} GeV$$

Forward Calorimetry The forward calorimeters close the CDF detector hermetically to $\eta = 4.2$. The FEM (Forward Electromagnetic Calorimeter [66]) is composed 30 layers of proportional tubes alternated with 0.48 cm lead antimony alloy plates. (Total thickness of 25.5 radiation lengths.) They give us good electron/π discrimination and a position resolution between 1 and 4mm and an energy resolution (test beam) of

$$\frac{\sigma_E}{E} \sim \frac{28\%}{\sqrt{E}} GeV$$

The FHA (Forward Hadronic Calorimeter [67]) is comprised 27 proportional tube layers alternated with 5.1 cm iron plates. The energy resolution is

$$\frac{\sigma_E}{E} \sim \frac{130\%}{\sqrt{E}} GeV.$$

5.2.5 CMU – Central Muon Chambers

A high energy (straight) track in CTC with little or no energy in the calorimeter is the first clue that a muon has passed through the detector. We measure the track momentum from the CTC, and match the track to a "stub" found in the Central MUon chamber (CMU) [68]. The central muon detectors

are drift chambers built onto the back of the calorimeter wedges and cover $-0.63 < \eta < 0.63$. Each drift chamber measures 6 cm by 2.7 cm by 2.2 m and has one stainless steel resistive 50 micron sense wire in the middle of it. See figure 5.6. To reach these chambers a particle must have passed through both the CEM and CHA and must have lived long enough to travel the 3.5 meters from the beam line, (4.9 absorption lengths), so a muon must have at least 1.4 GeV energy. The chambers are filled with the standard argon-ethane gas mixture, and we operate them in limited streamer mode. The ionization trail of the muon in the gas avalanches to make anode wire pulses in each of the four chambers the muon traverses. By measuring the time of arrival of each pulse (knowing the drift velocity of an electron within the cell), we can deduce the path of the muon in the r-ϕ plane. A left-right ambiguity as to which side of the wires the muon passed is resolved by offsetting the top two planes of wires relative to the bottom two. The direction in z can be determined by measuring the relative pulse heights at both ends of the anode wires. Cosmic ray tests show the chambers have a resolution of 250 microns in ϕ and 1.2 mm in z.
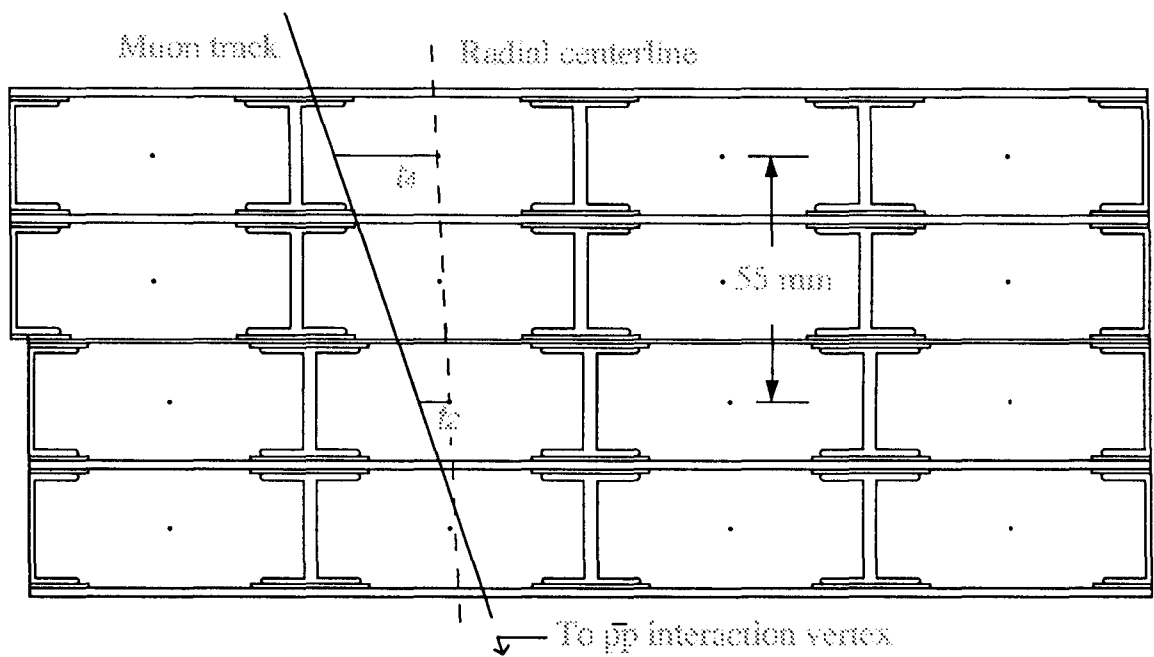
Figure 5.6: Cross sectional view of the central muon chambers [2].

5.2.6 CMX – Central Muon Extension

These exotic-looking detectors see muons which are just outside the central muon detectors in η ($0.6 < \eta < 1.1$). They consist of four layers of proportional wire chambers which read position information about the track, and two layers of scintillating tile which identify the time the track passed through the chambers.

5.2.7 CMP – Central Muon Upgrade

The central muon upgrade fits around the central barrels outside 30 cm thick iron walls. Muons must have over 2.8 GeV to penetrate through so much material. The CMU chambers register hits when jets *punch through* the calorimeter. The additional steel between the CMU and CMP traps enough particles that only 1/167 of $\pi^{\pm}$ or $K^{\pm}$ punch through to the CMP. They are proportional wire chambers in the same style as the CMU and CMX, but there is no scintillator to measure timing information. The chambers are long tubes stretched in the z-direction, so only information about the track in the directions perpendicular to the chambers is available.

5.2.8 FMU – Forward Muon Chambers

Three sets of drift chambers make up the Forward Muon Chambers [69]. They are $\sim$ 1.0 m wide, 7.6 m diameter large steel toroids between $1.9 < \eta < 4.0$ or 17° to 2° in θ. The toriods are cast steel, 395 tons, and produce a 1.4 Tesla field at 2.0 m so that the charged muon tracks bend and the momentum

measured. The FMU is 7.6 m diameter to match the toroids and is segmented in r and ϕ so that a muon momenta can be determined in all three dimensions.

5.2.9 BBC – Beam-Beam Counters

The Beam-Beam Counters are situated just in front of the Forward Calorimetry at 5.8 m from the interaction point and range from from 0.32 to 4.47 degrees in θ. These detectors are small scintillating tile detectors, but despite their dimimutive size, they have a crucial role to play in the experiment. If tracks don't leave a signal in *both* detectors within a window of 15 nanoseconds around the collision time, then the detector isn't read out. By counting the number of collisions where the BBC allowed detector readout, we can calculate the luminosity delivered to the experiment.

CENTRAL DETECTOR

CENTRAL MUON UPGRADE

CENTRAL MUON EXTENSION

FORWARD MAGNETIZED
STEEL TOROIDS

BACKWARD MAGNETIZED
STEEL TOROIDS

BACKWARD ELECTROMAGNETIC AND
HADRONIC CALORIMETERS

SVX

FORWARD ELECTROMAGNET AND
HADRONIC CALORIMETERS

LOW BETA QUADS
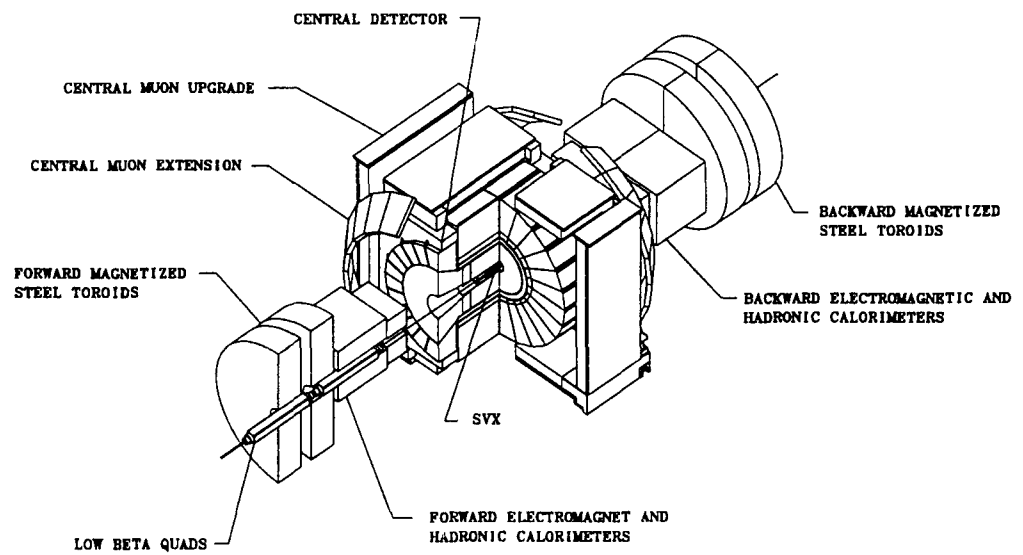
Figure 5.7: Perspective drawing of the CDF Detector with a cutaway section to show the central tracking and magnet.

Chapter 6

Event Selection

Reading the events off the detector and interpreting them is a complicated process. The tremendous number of events appearing in the detector must be filtered to remove events not relevant to this analysis. This chapter describes how the trigger selects interesting events during data-taking and how I select events which are appropriate to this specific analysis from the data on tape.

6.1 Trigger

We have a three-level trigger at CDF [70]. Each successive level has more time and information upon which to determine if an event should be passed to the next higher level. Levels 1 and 2 are hardware triggers, constructed from printed circuit boards and the fastbus control software. Level 3 is a software trigger. It is encoded in FORTRAN and run on a silicon graphics cluster. If the BBC's (Beam Beam Counters) permit it, the *fast-outs*, or analog

impulses from the calorimeter, are summed on hardware boards to find rough patterns of energy in the detector. The trigger also looks for muon stubs, two to four hits in the muon chambers. The trigger determines the momentum of the muon by the slope of the tracks in the muon chambers, and cuts at 3.3 GeV/c. Without the CTC information, this is necessarily a rough estimate of the features of the event, but Level 1 is faster than the 3.5 μs bunch crossing time. The uncertainty in the measurement of angle the track is 5 mrad. The uncertainty in the Level 1 p_t has not been measured, but the dominant effect is the multiple scattering in the calorimeter [71]. The plot of the p_t turn-on for Level 1 muons is shown in figure 6.1, by R. Hans and F. DeJongh [3]. Of the 50,000 events entering the detector per second, only 2% pass Level 1. Events passing Level 1 move on to the next level for a more precise determination of the nature of the event.

Level 2 looks more closely at the fast-out signals, summing them to find jet energy clusters. Some CTC tracking information is available through the CFT, the fast tracking system [72]. The CFT finds the r-ϕ components of the tracks and sorts them according to p_t, with a precision of $\frac{\Delta p_t}{p_t} \sim 0.035\ p_t$. This is a big improvement in accuracy over the measurements made at Level 1. Yet, as it is based only on one prompt hit out of 12 possible in a layer, there is still a sacrifice in the accuracy to the time constraint (3.5 μs). Level 2 extrapolates the tracks out to the muon chambers to determine the momentum of the muons in the event.

The Level 2 dimuon trigger, in particular, requires at least two Level 1

CMU muons, one of which matches to a CFT track; or one CMU muon and one CMX muon, where the CMU muon matches to a CFT track. In the later part of the run, two triggers were added here to complete the set, one CMU and one CMX, the CMX matching to a CFT track; and two CMX muons, one of which matches to a CFT track. This CFT track must have a $p_t > 2.5$ GeV/c. Events move on to Level 3 at about 20 events per second.

Level 3 subjects an event to the scrutiny of the same analysis program that is used offline, though it is simplified somewhat for speed considerations. It uses full tracking reconstruction from the CTC so that the momentum of muons and other tracks can be determined accurately. In particular at Level 3, the dimuon triggers required that both muons have a $p_t > 2.0$ GeV/c, and that they match to CTC tracks within 4σ, and finally, that one muon should have a $p_t > 2.5$ GeV/c. Events are written to magnetic tape at a rate of about 6 events per second.

The roughness of the calculation of the muon momentum at Level 1 and even at Level 2 in the trigger causes the cuts on transverse momentum to be more approximate than desired. Figures 6.1 and 6.2 show the muon p_t *turn-on* for Levels 1 and 2.

The trigger also requires the muons to be separated by a calorimeter tower. This reduces slightly the effect of *punch-through* from high-energy jets which pass completely through the calorimeter to leave tracks in the muon chambers. The luminosity collected in the 1991-1992 run by the dimuon trigger [73] was

$$\mathcal{L} = 19.3 \pm 0.7 \times 10^{30} \text{ cm}^{-2}\text{s}^{-1}.$$

Reading the data from tapes, offline reconstruction sorted dimuon events according to dimuon mass into one of several data sets. These are the data sets I use in this analysis:

Data Set	Dimuon Mass Range
Dimuon 1	0.0 to 2.8 GeV/c²
Dimuon 2	2.8 to 3.2 GeV/c²
Dimuon 3	3.2 to 4.6 GeV/c²

Dimuon 2 contains the $\psi \to \mu^+\mu^-$ resonant events, and dimuon 3 contains the $\psi' \to \mu^+\mu^-$ resonance as well as the nearby non-resonant events. If an event has three muons in it and qualifies for two or more of the datasets, this is recorded so that later one can preferentially choose a version of the event. A few events sneak into the sets which didn't pass any of the dimuon triggers (they pass some other trigger). These *volunteers* are few in number and scattered about the dimuon spectrum, so I accept them for use in this analysis.

There were 2×10^9 B's produced in run 1A and 80-90,000 dimuon pairs in the ψ region. Approximately 20% of these ψ's came from B decays [61]. This analysis selects < 80 of them.

6.2 Muon Reconstruction

This analysis requires the use of all the central muons available from the CMU, CMP and CMX. In each case, the Level 3 trigger projects the muon's CTC

track to the muon chambers, calculates the difference in position between the projected track and the muon stub, corrects for the p_t-dependent effects of multiple scattering and energy loss, and creates the χ^2 matching quantities. (The square root of the χ^2 matching variable has Gaussian distribution with $\sigma = 1$, and is designed to be independent of p_t.) I keep events within 2σ of perfectly matched CTC-muon combinations.

In addition to this matching of tracks, I require that the muon tracks match to SVX tracks. Level 3 analysis determines whether such a match exists.

The *CMP swim* cut requires that if a muon has enough energy and is headed in the direction of the CMP it must have a CMP muon stub. Events which don't are left out.

Both muons must have p_t greater than 2.0 GeV/c, and one must have transverse momentum greater than 2.5 GeV/c. These are the same cuts as are applied at Level 3 of the trigger.

Finally, I group the events into resonant and non-resonant dimuon mass groups. The resonant events have a dimuon mass between 3.062 and 3.132 GeV/c^2, or ± 35 MeV/c^2 around the ψ mass of 3.097 GeV/c^2. The non-resonant region of interest is 0.0 to 2.9, 3.3 to 3.6 and 3.8 to 4.6 GeV/c^2. This cuts away from the ψ and ψ' resonances. See, for example, figure 6.3.

6.3   Track Reconstruction

While overall perfectly reliable, the CTC electronics may output a poor quality track for a particle passing through it due to insensitivity of the detector or due

86

to a closely spaced neighbor track (particularly at the inner layers). This may result in missing hits along the trajectory or a short, partially reconstructed track. It is helpful to make a cut on the number of hits recorded for the track, and customary to require at least two axial layers with five or more hits each, and at least two stereo layers with two or more hits each.

Without particle identification at CDF, we have no information about whether a track is a Kaon or a pion or anything else (except muons). We assume the identity of the particle and use that mass in our calculations. Here, tracks are equally likely to be K's or π's so I have tried all combinations. This *combinatoric* background is the largest background in my analysis. The sophisticated cuts necessary to reduce it are covered later.

If the SVX information is available for these tracks I use it, but it is not required. Notice that if the two muons leave SVX tracks, it is likely that the other tracks pass through the fiducial volume as well.

In the case of $B \to \mu^+\mu^- K^{\pm}$, the Kaon momentum comes directly from the tracking chamber information combined with the Kaon mass. Good Kaons have $p_t > 2.0$ GeV/c. In the case of $B \to \mu^+\mu^- K^{*0}$, the K and π may have any transverse momentum. However, below 400 MeV/c the track curls in the solonoidal field without reaching the outer layer. Since the track reconstruction algorithm starts with the track segments in the outer layer, these tracks are necessarily ignored. The K^* momentum is a vector sum of the Kaon and pion momenta, and good K^*'s have transverse momentum > 2.0 GeV/c. The B momentum is a vector sum of the momenta of the three or four decay products,

and the cut is at 6.0 GeV/c. The K^* mass comes from $m^2 = E^2 - \vec{p}^2$ (having set c = 1). It must be within ± 100 MeV/c^2 of the world average value, 0.896 GeV/c^2. Similarly constructed, the mass of the B candidate is of considerable interest, since evidence of the non-resonant decays would result in a peak in the B mass relative to the sidebands, so I don't cut on it here, but do further analysis.

Cut	Value
μ Matching χ^2	$< 2\sigma$
μ p_t	$> (2.0, 2.5)$ GeV/c
ψ mass width	$\pm$ 0.035 GeV/c^2
$K^\pm$ p_t, $B \to \mu^+\mu^- K^\pm$ only	> 2.0 GeV/c
K^* p_t, $B \to \mu^+\mu^- K^{*0}$ only	> 2.0 GeV/c
K^* mass width	$\pm$ 0.100 GeV/c^2
B p_t	> 6.0 GeV/c

Table 6.1: Cuts to establish data set.
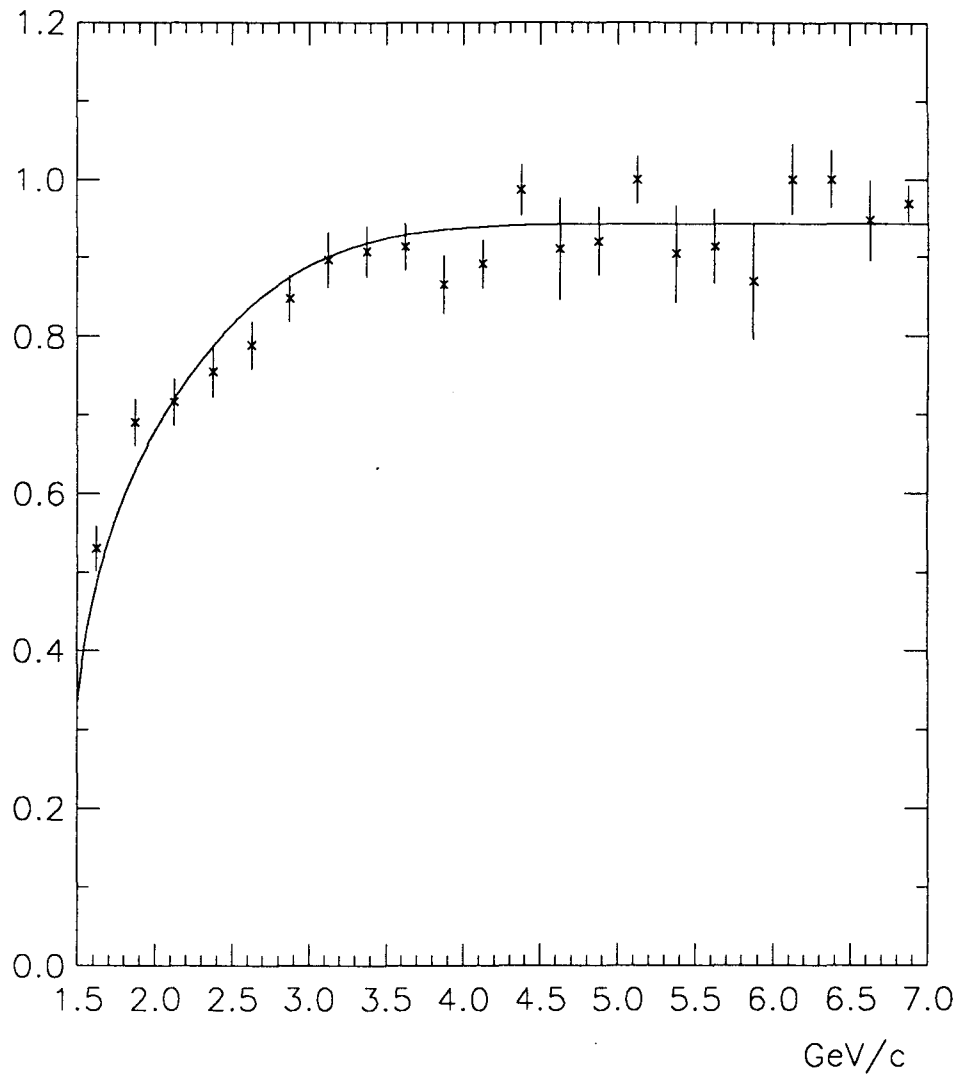
Figure 6.1: Level 1 muon p_t turn-on, efficiency versus p_t [3].
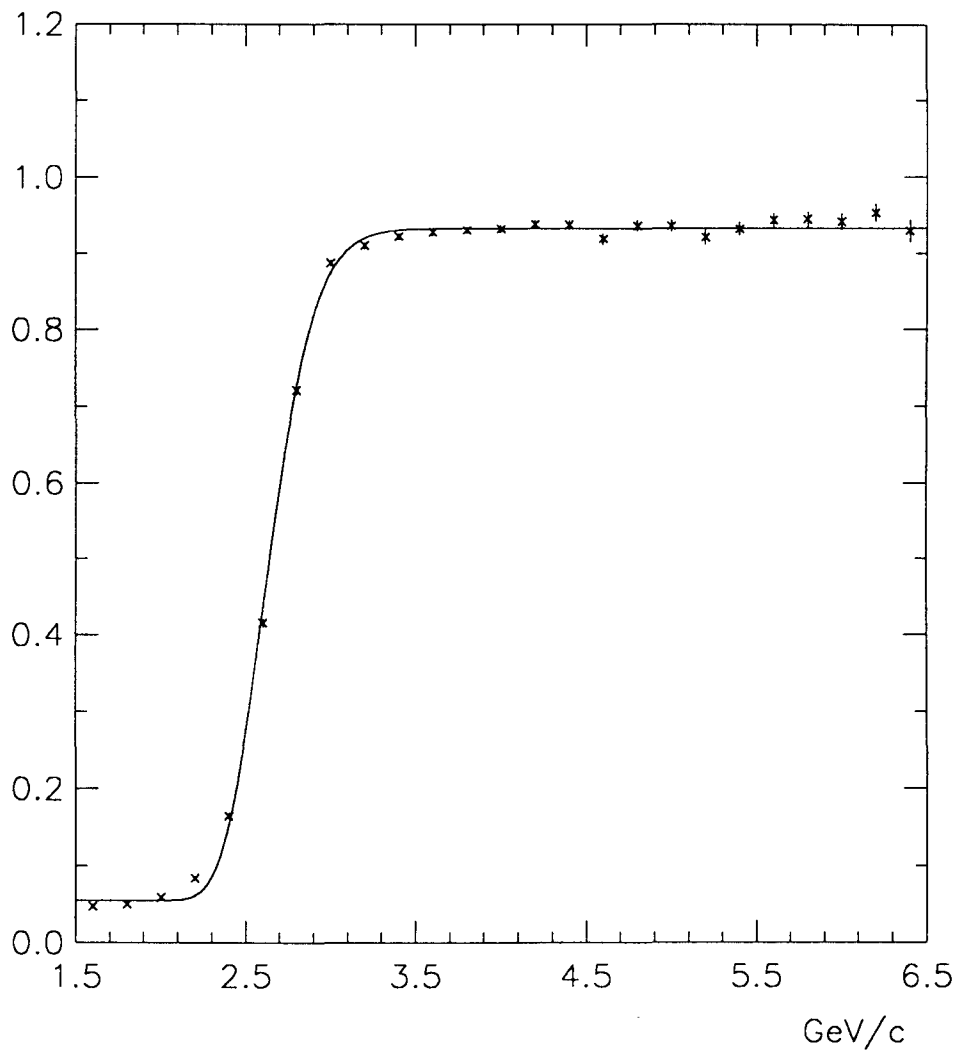
Figure 6.2: Level 2 muon p_t turn-on, efficiency versus p_t [3].

90
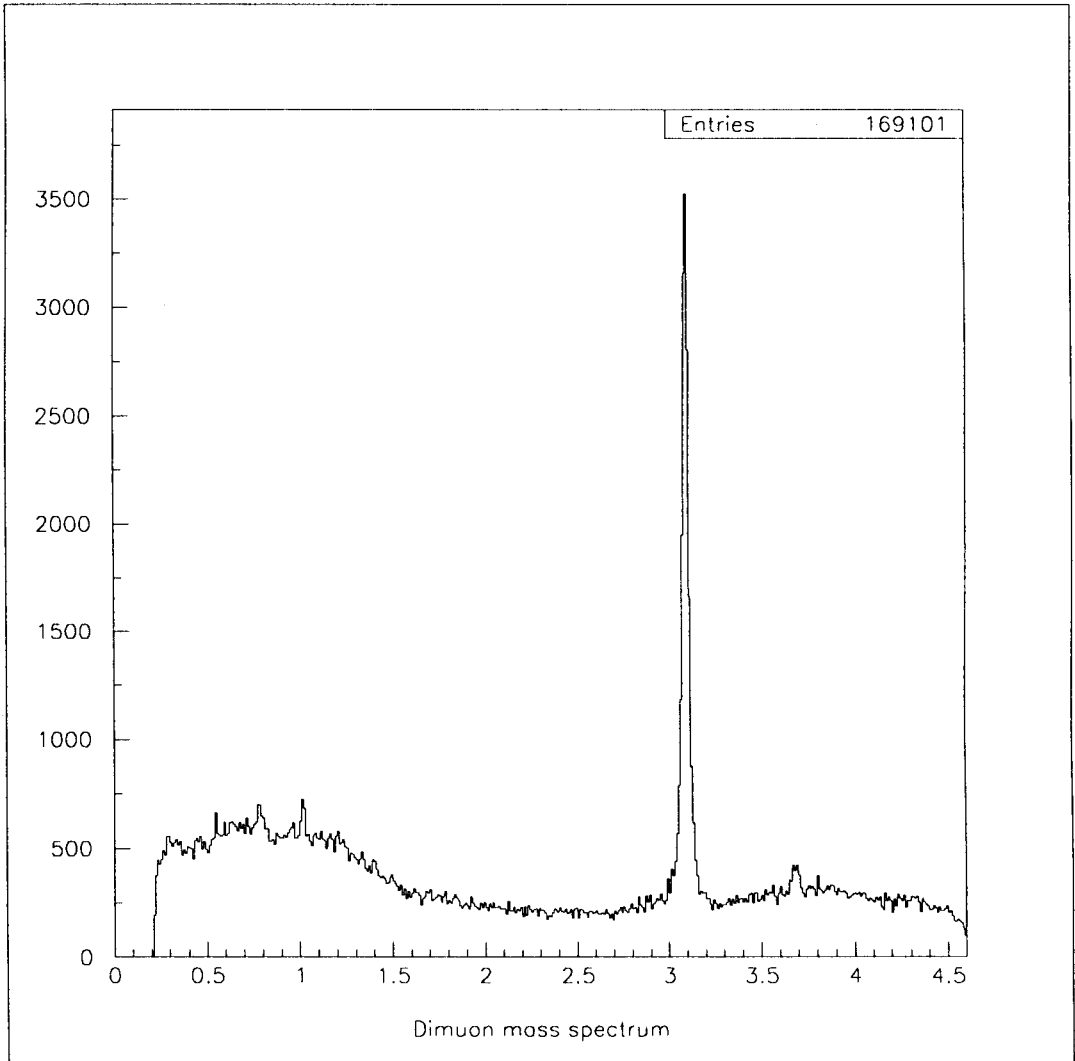
Figure 6.3: The dimuon mass spectrum with SVX muons. See the ω at 0.782 GeV/c^2, the ϕ at 1.020 GeV/c^2, the J/ψ at 3.097 GeV/c^2 and the ψ' at 3.686 GeV/c^2.

Chapter 7

Data Analysis

The set of events with two muons and tracks which pass all the selection criteria forms the foundation for the analysis. As stated in chapter 3, the ratio of branching ratios,

$$\frac{BR(B \rightarrow \mu\mu K)}{BR(B \rightarrow \psi K, \psi \rightarrow \mu\mu)},$$

where K is either $K^{\pm}$ or K^{*0}, is of interest to physicists, as is the overall branching ratio $BR(B \rightarrow \mu\mu K)$. In addition to its theoretical interest, an analysis to determine the ratio of branching ratios has other advantages. Systematic errors in the efficiency, acceptance and luminosity that enter into a calculation of the branching ratio limit cancel in this case. There is a small asymmetry left in the relative efficiency which is calculated using Monte Carlo. Here I show the analysis to find the ratio of branching ratios for each of the decay modes of interest. The resonant branching ratios have been measured with other experiments [74], so to determine the overall branching ratio limit,

I use the world average values [75] in the branching ratio calculation. The branching ratio relates to the experimental results as follows:

$$\frac{BR(B \to \mu\mu K)}{BR(B \to \psi K, \psi \to \mu\mu)} = \frac{N(B \to \mu\mu K)}{N(B \to \psi K, \psi \to \mu\mu)} \times \frac{\epsilon_\psi}{\epsilon_{\mu\mu}}$$

where BR is the branching ratio of the indicated decay, N the number of events seen and ϵ the efficiency of finding the events.

To proceed with the analysis, then, it is crucial to have available a calculation of the relative efficiency of the resonant and the non-resonant dimuon mass regions. After the Monte Carlo calculations, I'll discuss additional cuts, histograms of results, cut optimization, and the calculation of the branching ratio limit.

7.1 Monte Carlo Results

There are two ways to use the RareB Monte Carlo (introduced in chapter 4). The first is to calculate the relative efficiency between the two dimuon mass regions. Since both signals come from B decays, the B production physics is the same for both regions. The non-resonant dimuon mass region allows a slightly higher momentum for the two muons on average than in the resonant case, since the dimuon mass is, on average, higher in the non-resonant case. The amount of phase space left for the $K^\pm$ or K^{*0} is smaller, so their average momentum is slightly lower in the non-resonant region.

The other important function that the RareB Monte Carlo serves is to

give the analysis the factor to extrapolate from the small dimuon mass region studied here to the overall dimuon mass range allowed by phase space concerns. This leaves the calculation of the overall branching ratio limit with some dependence on theory, but that dependence is small.

7.1.1 Relative Efficiency

To calculate relative efficiency, I apply a fast detector parameterization and trigger parameterization (written by F. DeJongh) to RareB Monte Carlo output. The trigger parameterization is based on trigger studies conducted by F. DeJongh and R. Hans [3], and is shown in figures 6.1 and 6.2. The following constraints and cuts are placed on this Monte Carlo output:

Detector Geometry Events in the Monte Carlo and in the detector are produced in all directions. This cut accepts only those events which have decay products which pass through the sensitive portions of the detector.

Trigger Acceptance This cut accepts only those events wherein both muons have a high enough transverse momentum to pass the dimuon trigger. Multiple scattering effects are included.

μ $p_t > (2.0, 2.5)$ **GeV/c** This cut accepts events with muons which pass the momentum cut of 2.0 GeV/c, and where one of the muons is additionally required to have transverse momentum greater than 2.5 GeV/c. Note that this is the same cut as the trigger makes, but the trigger has a slow turn-on.

Meson p_t This cut accepts only events which have a total transverse momentum such that B $p_t > 6.0$ GeV/c, and where the transverse momentum of the sum of the two non-muon tracks satisfies $K^{*,\pm}$ $p_t > 2.0$ GeV/c.

These cuts are also imposed on the data. There are other cuts introduced later, but none of these has an effect on the relative efficiency. The result is a set of dimuon mass spectra, shown in figures 7.1 and 7.2. Figures 7.1a-e and 7.2a-e show the effect on the non-resonant dimuon mass spectrum of each cut applied sequentially in the order above. The muon transverse momentum cut within the trigger has the largest effect on the shape, it makes the large dimuon mass region have a slightly higher efficiency than the small. The transverse momentum cuts on the K and B nearly cancel it. The relative efficiency calculation uses

$$\epsilon_{rel} = \frac{\epsilon_{\mu\mu}}{\epsilon_{\psi}}$$

$$\epsilon_{rel} = \frac{N(B \to \mu\mu K, \text{final})}{N(B \to \mu\mu K, \text{initial})} \times \frac{N(B \to \psi K, \text{initial})}{N(B \to \psi K, \text{final})}$$

where N is the number of events indicated. The calculations are outlined in tables 7.1 and 7.2. The final relative efficiencies are

$$\epsilon_{rel} = 1.03 \pm 0.05 \text{ for } B \to \mu^+ \mu^- K^{\pm}$$

$$\epsilon_{rel} = 0.93 \pm 0.05 \text{ for } B \to \mu^+ \mu^- K^{*0}.$$

Figure 7.1: Sequence of relative efficiency histograms for $B \rightarrow \mu^+\mu^- K^\pm$. (a) Generated distribution, (b) After detector geometrical cut, (c) After trigger cut, (d) After muon p_t cuts, (e) After meson p_t cuts, (f) Overall efficiency as a function of dimuon mass.
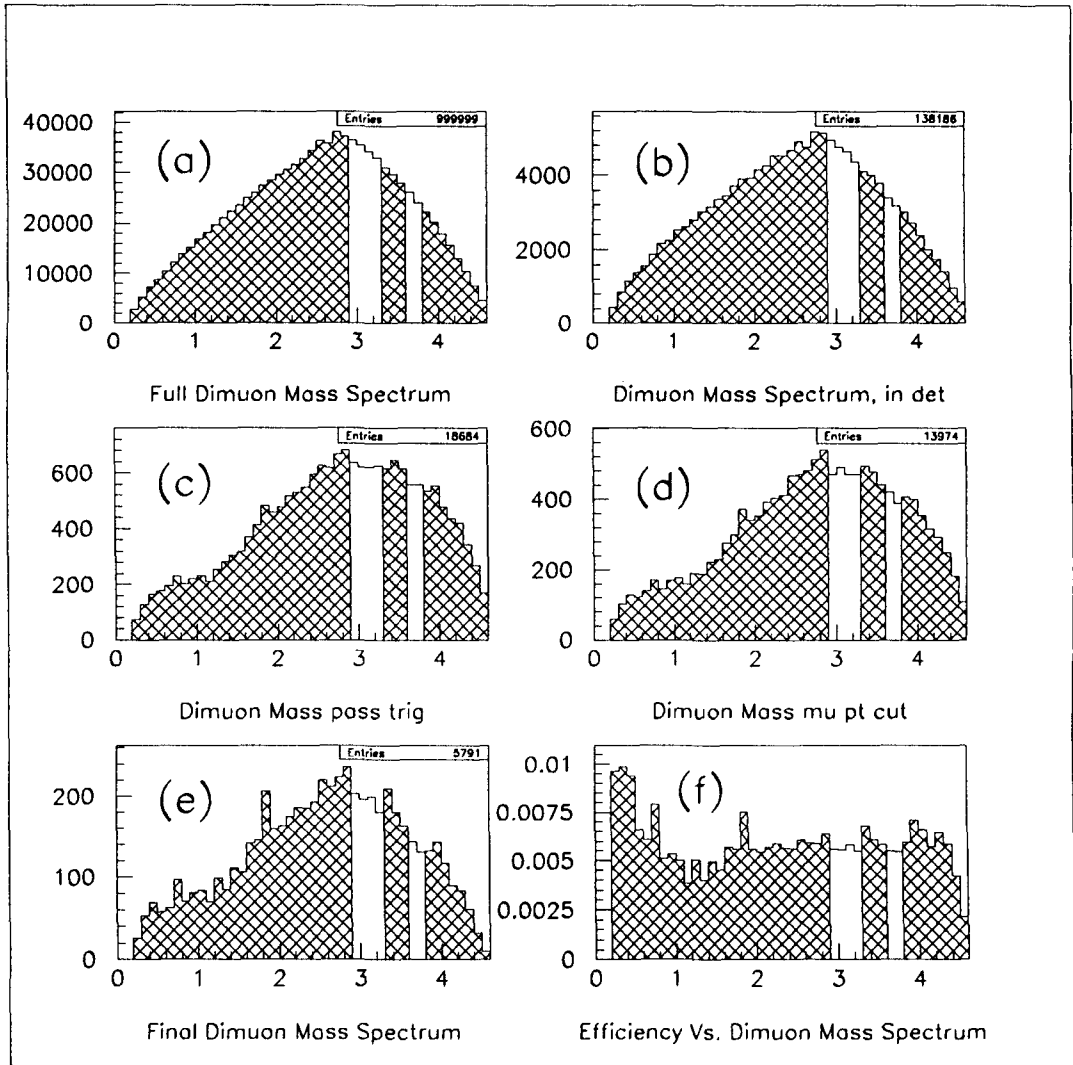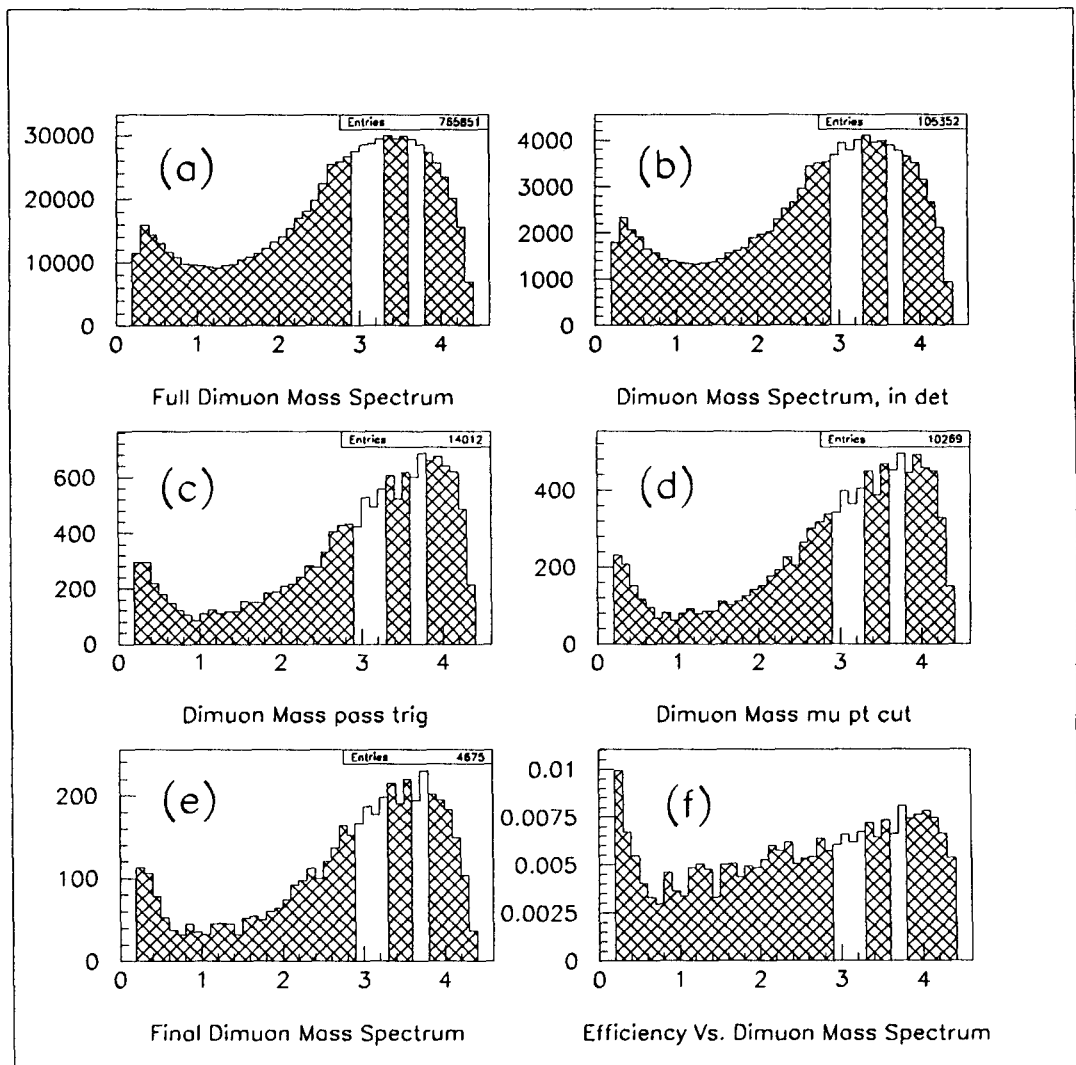
Figure 7.2: Sequence of relative efficiency histograms for $B \rightarrow \mu^+\mu^- K^{*0}$. (a) Generated distribution, (b) After detector geometrical cut, (c) After trigger cut, (d) After muon p_t cuts, (e) After meson p_t cuts, (f) Overall efficiency as a function of dimuon mass.

Cut description	Number of MC events		Relative efficiency
	ψ	$\mu\mu$	
Starting numbers	69,595	811,043	
Detector Geometry	9,373	112,958	1.034 ± 0.011
Trigger Acceptance	1,242	15,065	1.041 ± 0.030
Muon p_t	964	11,255	1.002 ± 0.032
Meson p_t	395	4,739	1.029 ± 0.050

Table 7.1: Relative efficiencies listed by cut for $B \rightarrow \mu^+\mu^- K^\pm$. The ψ column is the number of events in the small dimuon mass region between 3.00 and 3.20 GeV/c^2. The $\mu\mu$ column is the number of events in the hatched region on in the figure. The relative efficiency is the cumulative relative efficiency of all the cuts before it in the table.

Cut description	Number of MC events		Relative efficiency
	ψ	$\mu\mu$	
Starting numbers	57,108	594,104	
Detector Geometry	7,724	82,276	1.024 ± 0.012
Trigger Acceptance	1,020	10,722	1.010 ± 0.032
Muon p_t	762	7,812	0.985 ± 0.036
Meson p_t	364	3,523	0.930 ± 0.049

Table 7.2: Relative efficiencies listed by cut for $B \rightarrow \mu^+\mu^- K^{*0}$. The ψ column is the number of events in the small dimuon mass region between 3.00 and 3.20 GeV/c^2. The $\mu\mu$ column is the number of events in the hatched region on in the figure. The relative efficiency is the cumulative relative efficiency of all the cuts before it in the table.

7.1.2 Extrapolation Factor

The second important result from the RareB Monte Carlo is the factor to extrapolate my results from the non-resonant dimuon mass window to the overall dimuon mass range. To do this, I run the Monte Carlo with the long-distance (resonant ψ and ψ') effects turned off, plot the non-resonant curve of the theoretical differential decay rate for the whole dimuon mass region, count the events which lie in the dimuon mass region of interest, then divide that number by the total number of events generated. No cuts are applied, nor detector parameterization. This calculation is a theory calculation only. In figures 7.1a and 7.2a, the fraction is the hatched region divided by the clear region. The results are

$$0.8110 \pm 0.0009 \quad \text{for} \quad B \to \mu^+ \mu^- K^\pm \text{ and}$$
$$0.7757 \pm 0.0011 \quad \text{for} \quad B \to \mu^+ \mu^- K^{*0}.$$

7.2 Cuts

Briefly, my method is to select events which have a B candidate mass in an acceptable range and compare the B mass spectrum in the case where the muons have a mass in the non-resonant range with that where the muons are from resonant ψ's. In order to claim discovery of the rare non-resonant decay, one would need to produce the evidence of a B peak from $B \to \mu\mu K$ decays. Seeing no evidence of such a peak, I cut on the likelihood that the mass of

the tracks is truly the B mass, compare resonant and non-resonant portions of the dimuon mass spectrum and use these numbers to calculate the lowest limit possible with the data. This section presents a detailed discussion of the proceedure.

The B mass spectra, figures 7.5, 7.6, 7.9, and 7.10 are filled with events which are constrained simultaneously as follows: the tracks are constrained to come from a common vertex, and the direction of this secondary vertex away from the primary vertex in the x-y plane is constrained to follow the direction of the B candidate. This last is called a *pointing* constraint. These events must pass three cuts: the likelihood of the fit just described must be greater than 10%; the fraction of momentum the B carries within a cone of 1.0 in η and ϕ must be greater than 0.6; and the transverse proper decay time ($c\tau$) of the B candidate must be greater than 0.01 cm. Figures 7.5 and 7.9 show the distinctive peak from resonant $B \to \psi K^{\pm}$ and $B \to \psi K^{*0}$ events, respectively. Figures 7.6 and 7.10 contain events with non-resonant dimuons.

To be considered a B signal candidate event, the reconstructed candidate must have a B mass which lies between 5.2287 and 5.3287 GeV/c^2, that is, within $m_B = 5.2787 \pm 0.0500$ GeV/c^2. The sidebands provide a good estimate of the background. They range from 5.13 to 5.23, 5.33 to 5.43, 5.43 to 5.53, and 5.53 to 5.63 GeV/c^2, the hatched regions of the figures. I do not see any excess of non-resonant $B \to \mu\mu K$ events in figures 7.6 or 7.10.

It is reasonable to calculate a branching ratio limit from the information in the B mass spectra. However, to achieve the best limit, I apply another

vertex fit. This fit contains the following constraints: the vertex constraint, the pointing constraint, and a constraint on the mass of the B candidate to the world average B mass. I cut on the quality of that fit, and plot the dimuon mass spectra of these events in figures 7.7 and 7.11. The background in these plots can be estimated from the B sidebands. I constrain the B candidate mass to the the midpoint of each sideband so that a track combination with a mass between 5.13 and 5.23 GeV/c^2 goes to 5.18, and combinations between 5.33 and 5.43 GeV/c^2 go to 5.38 GeV/c^2, etc. See figures 7.8 and 7.12. The number of candidate signal events is consistent with background. Comparing it to the number of resonant events above background gives an upper limit on the branching ratio. This second vertex fit, the additional information that we expect the signal events to come from a B meson with known mass, lowers the limit by 10-20%.

The rest of this section is devoted to a discussion of the cuts.

First fit probability	>	10 %
momentum fraction	>	0.6
$c\tau$	>	100 μm
Second fit probability	>	10 %

7.2.1   Fit Probability

There are four vertex fits in this analysis.

1. vertex fit of the two muons alone to determine their momenta for the cuts on $p_t(\mu)$ and dimuon mass. No pointing constraint or mass constraints.

2. vertex fit with pointing constraint but with no mass constraints,

3. vertex fit with pointing constraint and mass constraint on J/ψ's (to compare to other analyses),

4. vertex fit with pointing constraint and with mass constraint on all tracks, constraining them to the B mass.

The vertex fits return a χ^2 value. It is conventional at CDF to transform this into a fit probability value. The advantage of using this function is that it is independent of the number of degrees of freedom of the fit (which could be done by dividing the χ^2 by the number of degrees of freedom) and condenses the distribution function for badly fit events. I make cuts on both the vertex-only constraint fit probability (first fit probability cut) and the vertex and mass constraint fit probability (second fit probability cut). I cut at 10% in both cases. Though the fit quality goes down slightly with increased momentum of the tracks, the cut doesn't affect the relative efficiency because the momentum dependence is folded into the uncertainty χ^2. Thus the fit probability is independent of momentum. The distribution of signal and sideband events for the fit probability distribution, as well as the effect the cut has on the B mass spectrum are shown in figure 7.3, top.

7.2.2   B Momentum Fraction

The second cut is on the fraction of momentum the B carries within a cone of 1.0 in η and ϕ (η is pseudorapidity of the track and ϕ its angle from the x-

axis). To determine this fraction, I loop over all the other tracks in the event, excluding the tracks involved in the B candidate, to check the difference in R angle ($R = \sqrt{\eta^2 + \phi^2}$), between the track and the reconstructed B momentum. If a track satisfies the inequality

$$\Delta R = \sqrt{(\eta_{tr} - \eta_B)^2 + (\phi_{tr} - \phi_B)^2} < 1.0,$$

then it is inside the cone. I do a 3-D vector sum of the tracks in the cone, excluding the tracks which make up the B candidate, and construct the quantity

$$fr\_mom = \frac{|\vec{p_B}|}{|\vec{p_B}| + \sum_{(tr \notin B)} \hat{n} \cdot \vec{p_{tr}}}, \quad \hat{n} = \frac{\vec{p_B}}{|\vec{p_B}|}.$$

By keeping events with $fr\_mom > 0.6$, this cut rejects events where the muon stubs are *punch-through* of many-track jets, or where the muon is imbedded in such a jet. Though more commonly used, a cone of 0.7 in η-ϕ space is too small to contain the low-energy jets in the events in the sample. The proceedure to calculate the optimal value of this cut will be covered later. Since this is a cut on the physics of the fragmentation of the original b quark, the effect of the cut is the same in the two dimuon mass regions, resonant and non-resonant. The distribution of signal and sideband events for the momentum fraction distribution, as well as the effect the cut has on the B mass spectrum are shown in figure 7.3, middle.

7.2.3 Decay Time

The time the B meson lives is of considerable interest to this analysis. With the measurement of the decay time of the B in the exclusive channels $B \rightarrow \psi K^{\pm,*}$ [76], we have the information we need to do a cut on the lifetime. The SVX detector reads the decay distance in the x-y plane. It yields the primary vertex position to a precision of 40 μm in x and y, as discussed in chapter 6. The uncertainty in the position of the secondary vertex is somewhat broader, since there are fewer tracks in the fit. In figure 7.3, bottom, it is clear that there are a considerable number of prompt events in the central Gaussian peak, and that events with a distinct vertex away from the primary make up the long right-hand tail. These long-lived events are the ones of particular interest to me, so I cut at 100 μm.

The transverse proper decay time is

$$c\tau = \frac{L_{xy} \cdot m(B)}{p_t(B)}$$

where L_{xy} is the distance in the transverse plane which the B travels.

These values are all calculated from vertex constrained quantities. The decay time is independent of the mass of the dimuon system, so the efficiency for accepting events doesn't vary with dimuon mass. The distribution of signal and sideband events for the $c\tau$ distribution, as well as the effect the cut has on the B mass spectrum are shown in figure 7.3, bottom.

104
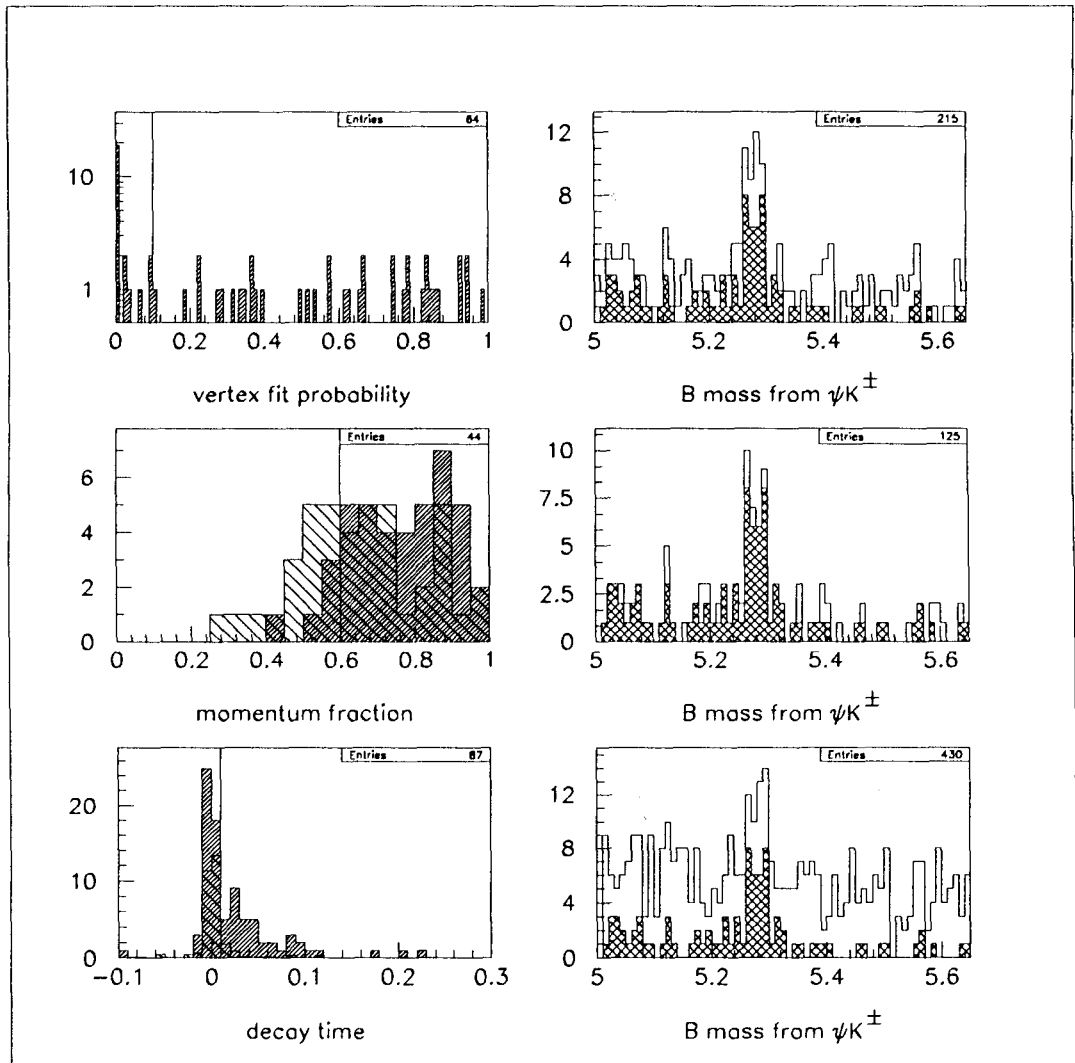
Figure 7.3: The left side has distributions of variables used for cuts on in the $B \rightarrow \mu^+\mu^- K^\pm$ analysis. The narrow hatched region has events from ψ and B peaks, and the wider hatched region has the ψ events from B sidebands. The right side has the effect of the cut on the B mass distribution where the clear histogram has all the cuts applied except the one of interest, and the cross-hatched region has all the cuts applied. *Top:* Fit probability from the vertex and pointing constrained fits. This is the distribution for the first cut on the fit probability. The cut is at 10%. *Middle:* Momentum fraction the B carries in a cone of 1.0 in η-ϕ space. Cut is at 0.6. *Bottom:* Proper decay time in centimeters. Cut is at 0.01 cm.

7.3 Numbers from Histograms

For each decay mode, there is a set of four histograms. The first two are B mass spectra. They have all the cuts imposed except for the second fit probability cut, the cut on the B mass constrained fit probability, which favors mass values at the center of each mass bin. That is, cuts are placed on $c\tau$, momentum fraction, transverse mometum, etc, including the first fit probability cut to construct the B candidate mass spectra, first from ψ resonance events (figures 7.5 and 7.9), then from non-resonant dimuons (figures 7.6 and 7.10).

Using the events in these histograms, I make the additional cut on the second fit probability and plot the dimuon mass spectra. Events with B candidate masses in the peak region are first (in figures 7.7 and 7.11). To estimate the background in that plot it is useful to plot the dimuon mass spectrum of events from the sidebands. The four same-sized sideband regions (from figure 7.5, for example) are in total about four times the size of the peak region, so the last plots, the B sideband dimuon mass plots (in figures 7.8 and 7.12), have about four times the background. The dimuon mass histograms provide the numbers in tables 7.4 and 7.6. Here is a explanation of the quantities in those tables, and how they come from the figures:

$N_{tot}=$ The number of shaded events in the non-resonant dimuon mass region of interest (0.0 to 2.9, 3.3 to 3.6 and 3.8 to 4.6 GeV/c^2), as shown in figures 7.7 and 7.11.

$b_0 =$ The background expected to account for N_{tot} is the number of events in

106

the non-resonant dimuon mass region of interest in figures 7.8 and 7.12, divided by a factor of approximately 4. This factor of approximately 4 comes from a linear fit to the sideband region in the $B \to \mu\mu K$ mass spectrum with all the cuts (not shown). For $B \to \mu^+ \mu^- K^\pm$ this number is 6.146, and for $B \to \mu^+ \mu^- K^{*0}$ it is 3.637. The background estimates are consistent with N_{tot}.

N_ψ = The number of $B \to \psi K$ events is the number of events in the black shaded region of the signal dimuon mass spectrum (figure 7.7 or 7.11) minus the number of events in the black shaded region of B sideband dimuon mass spectrum (figure 7.8 or 7.12) divided by about 4. For $B \to \mu^+ \mu^- K^\pm$ this number is 2.418, and for $B \to \mu^+ \mu^- K^{*0}$ it is 3.003.

These numbers, along with their uncertainties, go into the calculation of the branching ratio limit.

7.4 Cut Optimization

It is important to optimize the cuts to minimize the calculated branching ratio limit, being careful not to optimize directly on the branching ratio limit itself. That sort of optimization would construct a situation where the cuts caused a dip in the spectrum in the signal region. That is, it would preferentially choose a set of cuts which reflected a fluctuation in the number of events to

see. So, for each set of cuts, I construct the quantity

$$opt = \frac{N_\psi^2}{0.002 N_\psi + b_0}$$

where N_ψ is the number of B to ψ K events (above the ψ background) and b_0 is the background estimate. The above definition comes from maximizing the significance of the expected $B \to \mu\mu K$ signal, estimated as 0.002 times the number of events in the resonant $B \to \psi K$ peak, above expected signal plus background. The factor of 0.002 comes from Baillie [33]. It is the ratio of non-resonant to resonant rates expected from theory.

I choose the set of cuts which has the greatest value of this significance variable *opt*. The optimization quantity tracks the inverse of the branching ratio at even reasonably low statistics and avoids the problem of tuning cuts on the signal quantities.

Figure 7.4 shows the optimization variables for $B \to \mu^+ \mu^- K^\pm$ events. Each point represents one set of cuts. The y-axis is the measured branching ratio limit extrapolated to the overall dimuon mass region divided by the branching ratio of $B \to \psi K^\pm$. The x-axis is the optimization variable. Figure 7.4 demonstrates that the optimization variable is more or less inversely proportional to the branching ratio, so that it is reasonable to choose a cut set which has a large value of *opt*, with confidence that it represents a low value of the branching ratio limit. The results here come from the cut set furthest to the right.

Cut	Value
μ Matching χ^2	$< 2\sigma$
μ p_t	$> (2.0, 2.5)$ GeV
ψ mass width	± 0.035 GeV
$K^{*,\pm}$ p_t	> 2.0 GeV
K^* mass width	± 0.100 GeV
B p_t	> 6.0 GeV
B mass width	± 0.05 GeV/c^2
First Fit Probability	$> 10\%$
B Momentum Fraction	> 0.6
Decay Time	> 0.01 cm
Second Fit Probability	$> 10\%$

Table 7.3: Cuts used for the analysis of $B \rightarrow \mu^+ \mu^- K^{*0}$ and $B \rightarrow \mu^+ \mu^- K^{\pm}$.

Figure 7.4: Branching ratio Vs Optimization variable for various sets of cuts.

110

7.5 Branching Ratio Calculation

Once we have the number of events in the region of interest (see Tables 7.4 and 7.6), I calculate the branching ratio as described in [77] which is based on work by O. Helene [78] and G. Zech [79]. In general, the method is to compare the number of non-resonant events with the number of resonant ψ events, using this proportionality:

$$\frac{N(B \to \mu\mu K, \text{at } 90\% \text{ CL})}{N(B \to \psi K, \psi \to \mu\mu)} = \frac{BR(B \to \mu\mu K, \text{at } 90\% \text{ CL})}{BR(B \to \psi K, \psi \to \mu\mu)} \times \epsilon_{rel}$$

where N indicates the number of events of the type specified, BR the branching ratio of those same events, and $\epsilon_{rel} = \frac{\epsilon_\psi}{\epsilon_{\mu\mu}}$ the relative efficiency between finding the resonant events and non-resonant events.

If we had a large number of events in the non-resonant region of interest, Gaussian errors would be appropriate and we could calculate the 90% confidence limits by hand. In this case, however, the number of signal event candidates is small, requiring Poisson statistics to calculate the upper limit on the branching ratio, but the error on the background estimate complicates matters. In the end, I use a renormalized Poisson curve to do the calculation.

If s is the 90% upper confidence limit on the number of events we see, b the number of background events estimated to be in the signal region, and N_{tot} is the total number of events in the signal region (which most likely can be accounted for by background), then the probability of seeing n events given a

111

Poisson with mean at $b + s$ is

$$P(n, b + s) = \frac{1}{n!} e^{-(s+b)} (s + b)^n$$

and

$$\epsilon = \sum_{n=0}^{N_{tot}} P(n, b + s)$$

is the probability that N_{tot} or fewer events are seen for a mean of b+s events. $\epsilon = 1 -$ CL, CL is the confidence level.

When the number of events in the signal region is on the order of the number of background events expected, b should not exceed N_{tot}, and the formula above underestimates the limit. Zech and Helene derive the renormalized Poisson distribution W.

$$W(n) = \frac{P(n, s + b)}{\sum_{n_b=0}^{N_{tot}} P(n_b, b)}$$

The probability that N_{tot} or fewer events are seen for a mean of $b + s$ events is described by

$$\epsilon = \sum_{n=0}^{N_{tot}} W(n)$$

$$\epsilon = \frac{\sum_{n=0}^{N_{tot}} P(N, s + b)}{\sum_{n_b=0}^{N_{tot}} P(n_b, b)}$$

In effect, the calculation finds the mean of a Poisson distribution which would fluctuate down to N_{tot} or below 10% of the time.

Finally, background errors can be included with Gaussian functions like this:

$$\epsilon = \frac{\sum_{n=0}^{N_{tot}} \int G(b) P(N, s+b) db}{\sum_{n_b=0}^{N_{tot}} \int G(b) P(n_b, b) db}$$

where $G(b)$ is a Gaussian distribution on the background estimate.

In my case, since

$$s = N(B \rightarrow \psi K, \psi \rightarrow \mu\mu) \times \frac{BR(B \rightarrow \mu\mu K)}{BR(B \rightarrow \psi K, \psi \rightarrow \mu\mu)} \times \epsilon_{rel}$$

and each of the quantities on the right-hand side of the equation have Gaussian uncertainties associated with them, I define the quantity g

$$g = \frac{N(B \rightarrow \psi K, \psi \rightarrow \mu\mu)}{BR(B \rightarrow \psi K, \psi \rightarrow \mu\mu)} \times \epsilon_{rel}$$

So that

$$s = g \, BR$$

where BR is the branching ratio limit, $BR(B \rightarrow \mu\mu K)$.

I sum the Gaussian uncertainties which figure in g and include them at once in the following formula.

$$\epsilon = \frac{\sum_{n=0}^{N_{tot}} \int G(b) G(g) P(n, g \times BR_{\mu\mu} + b) \, db \, dg}{\sum_{n_b=0}^{N_{tot}} \int G(b) P(n_b, b) db}$$

ϵ is one minus the confidence level, and G is a Gaussian function to model the errors on the values used. I change it to a Poisson sum at low values of the background b. N_{tot} is the total number of events counted in the region of

interest. b is the number of background estimated to be in the signal region, estimated from the sideband plot. The denominator is a renormalization factor for the probability distribution function.

I choose two widely separated values for the branching ratio limit, calculate ϵ for each, and average the values to do a binary search for the limit at the 90% confidence level. Then I divide the resulting branching ratio of interest by the fraction of the area under the theory curve used in the analysis to get the final limits.

7.6 Results

In Tables 7.4 and 7.6 I list numbers I got from the analysis using the full set of cuts. Using these in the method outlined above, I get the final results in tables 7.5 and 7.7.

N($B \rightarrow \mu\mu K$) candidates	=	3
background	=	4.1 ± 0.8
N($B \rightarrow \psi K$)	=	33.6 ± 6.4
BR($B \rightarrow \psi K, \psi \rightarrow \mu\mu$)	=	$6.5 \pm 1.0 \times 10^{-5}$

Table 7.4: Values used to calculate the $B \rightarrow \mu^+\mu^- K^\pm$ branching ratio limit.

$$\frac{\text{BR}(B \to \mu\mu K^\pm, \text{non} - \text{resonant})}{\text{BR}(B \to \psi K^\pm, \psi \to \mu\mu)} \quad < \quad 0.132 \text{ at } 90\% \text{ CL.}$$

$$\frac{\text{BR}(B \to \mu\mu K^\pm)}{\text{BR}(B \to \psi K^\pm, \psi \to \mu\mu)} \quad < \quad 0.163 \text{ at } 90\% \text{ CL.}$$

$$\text{BR}(B \to \mu\mu K^\pm, \text{non} - \text{resonant}) \quad < \quad 0.89 \times 10^{-5} \text{ at } 90\% \text{ CL.}$$

$$\text{BR}(B \to \mu\mu K^\pm) \quad < \quad 1.10 \times 10^{-5} \text{ at } 90\% \text{ CL.}$$

Table 7.5: Branching ratio limits for $B \to \mu^+\mu^- K^\pm$

N($\mu\mu K^*$) candidates	=	8
background	=	10.2 ± 1.7
N($B \to \psi K^*$)	=	39.0 ± 6.8
BR($B \to \psi K^*, \psi \to \mu\mu$)	=	$7.76 \pm 2.41 \times 10^{-5}$

Table 7.6: Values used to calculate the $B \to \mu^+\mu^- K^{*0}$ branching ratio limit.

$$\frac{\text{BR}(B \to \mu\mu K^*, \text{non} - \text{resonant})}{\text{BR}(B \to \psi K^*, \psi \to \mu\mu)} \quad < \quad 0.141 \text{ at } 90\% \text{ CL.}$$

$$\frac{\text{BR}(B \to \mu\mu K^*)}{\text{BR}(B \to \psi K^*, \psi \to \mu\mu)} \quad < \quad 0.181 \text{ at } 90\% \text{ CL.}$$

$$\text{BR}(B \to \mu\mu K^*, \text{non} - \text{resonant}) \quad < \quad 1.27 \times 10^{-5} \text{ at } 90\% \text{ CL.}$$

$$\text{BR}(B \to \mu\mu K^*) \quad < \quad 1.63 \times 10^{-5} \text{ at } 90\% \text{ CL.}$$

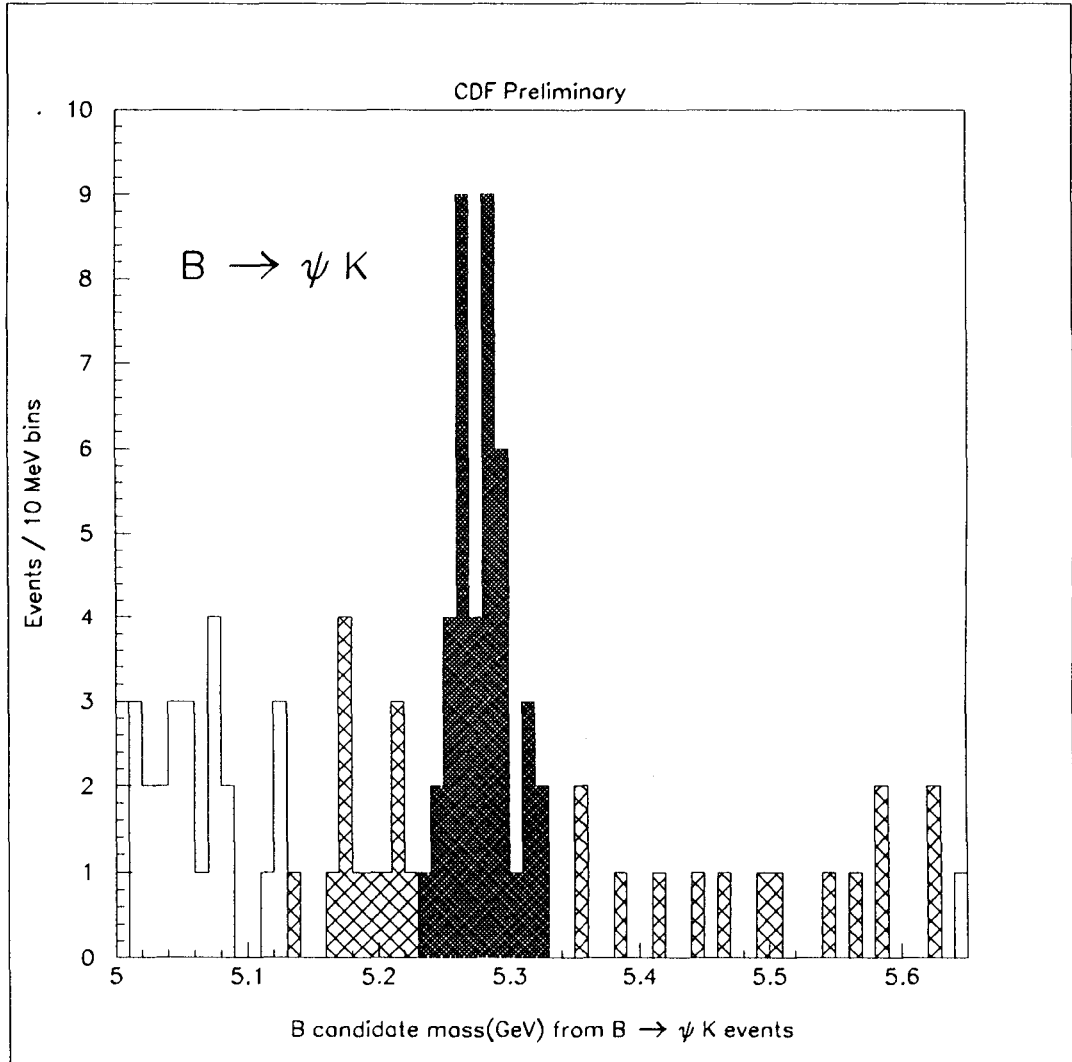Table 7.7: Branching ratio limits for $B \to \mu^+\mu^- K^{*0}$

Figure 7.5: B candidate spectrum from $B \rightarrow \psi K^{\pm}$ decays. All cuts but the last fit probability cut constraining peak and sidebands to the center of same-sized bins.
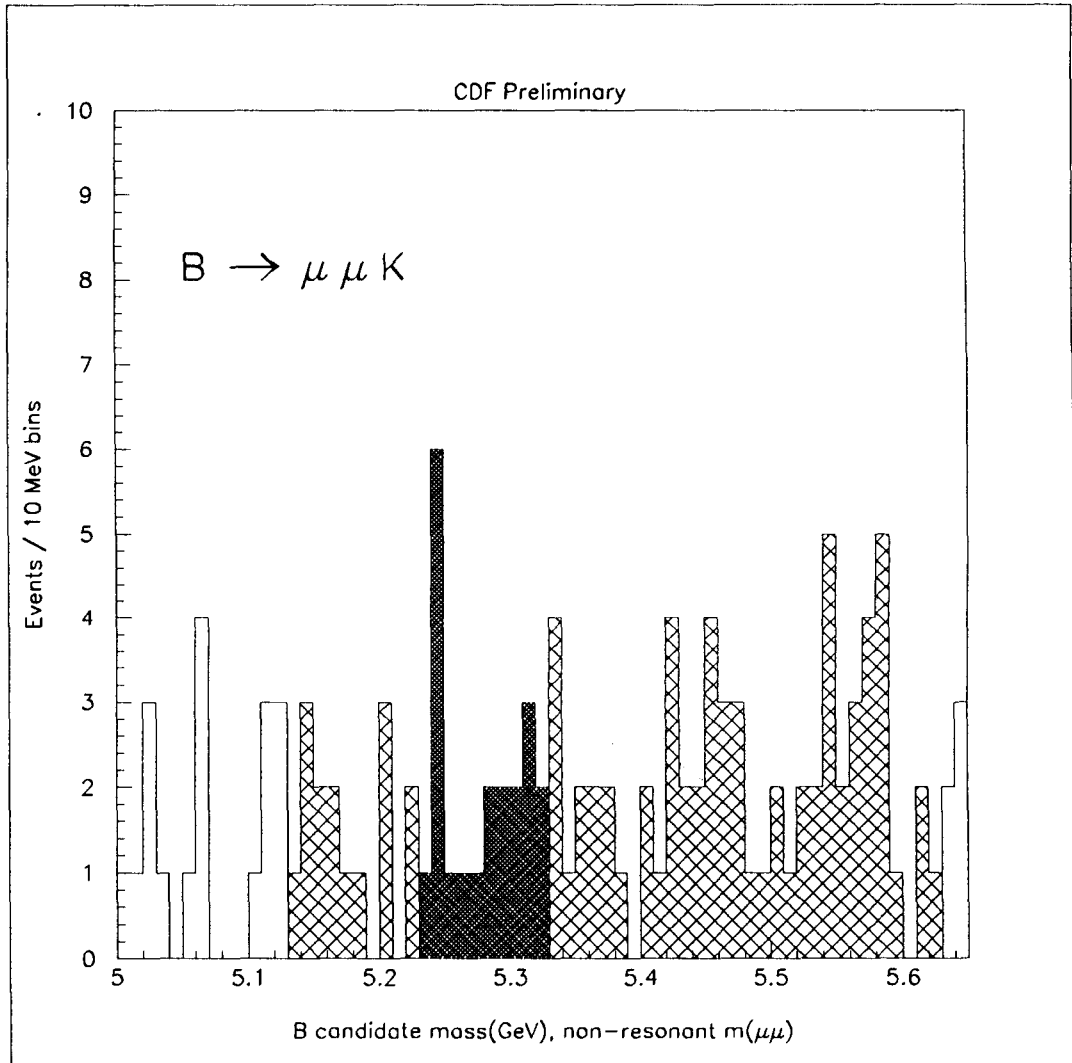
116

Figure 7.6: B candidate spectrum from $B \to \mu^+\mu^- K^\pm$ decays. All cuts but the last fit probability cut constraining peak and sidebands to the center of same-sized bins.
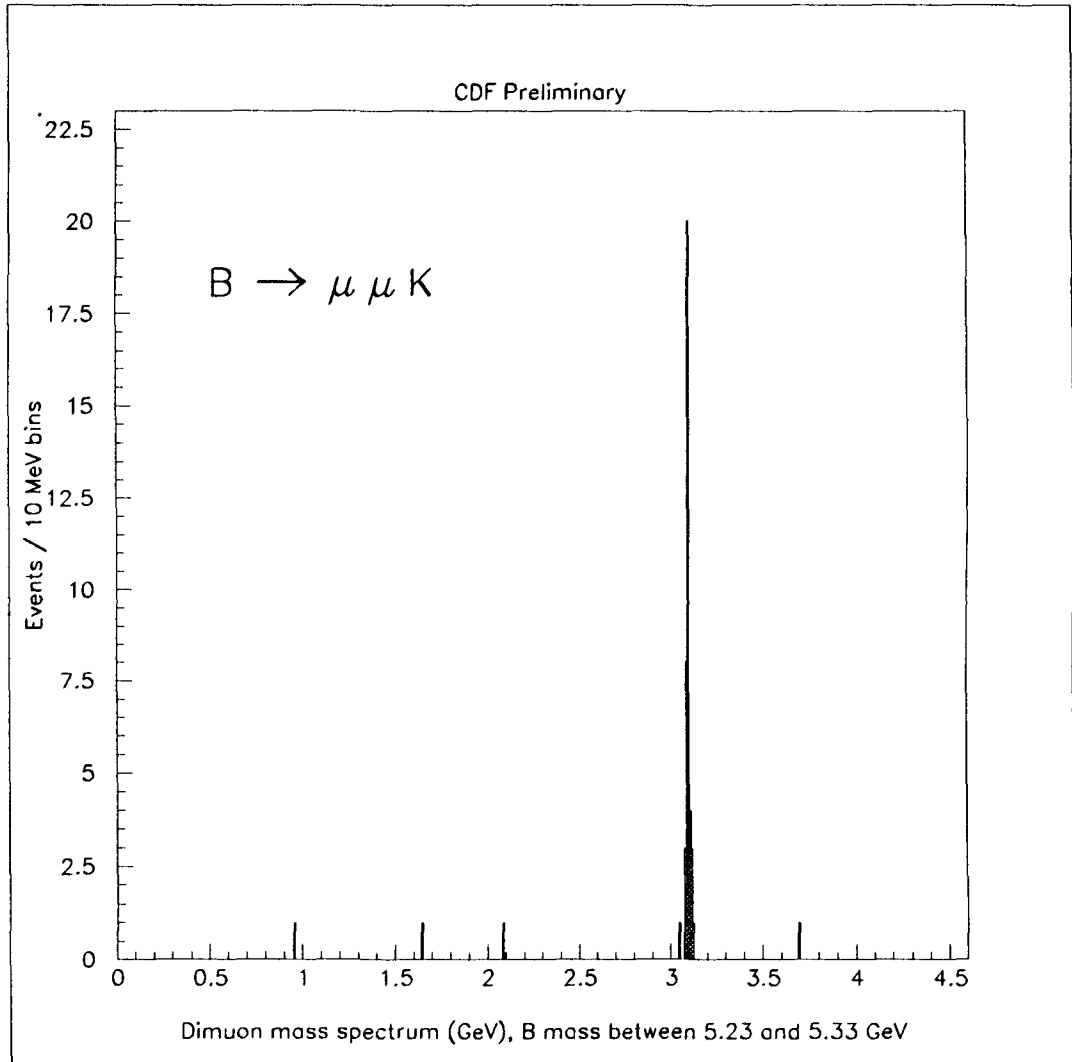
Figure 7.7: Dimuon mass spectrum from B peak events.

Figure 7.8: Dimuon mass spectrum from B sideband events.

Figure 7.9: B candidate spectrum from $B \to \psi K^*$ decays. All cuts but the last fit probability cut constraining peak and sidebands to the center of same-sized bins.

Figure 7.10: B candidate spectrum from $B \to \mu^+ \mu^- K^{*0}$ decays. All cuts but the last fit probability cut constraining peak and sidebands to the center of same-sized bins.

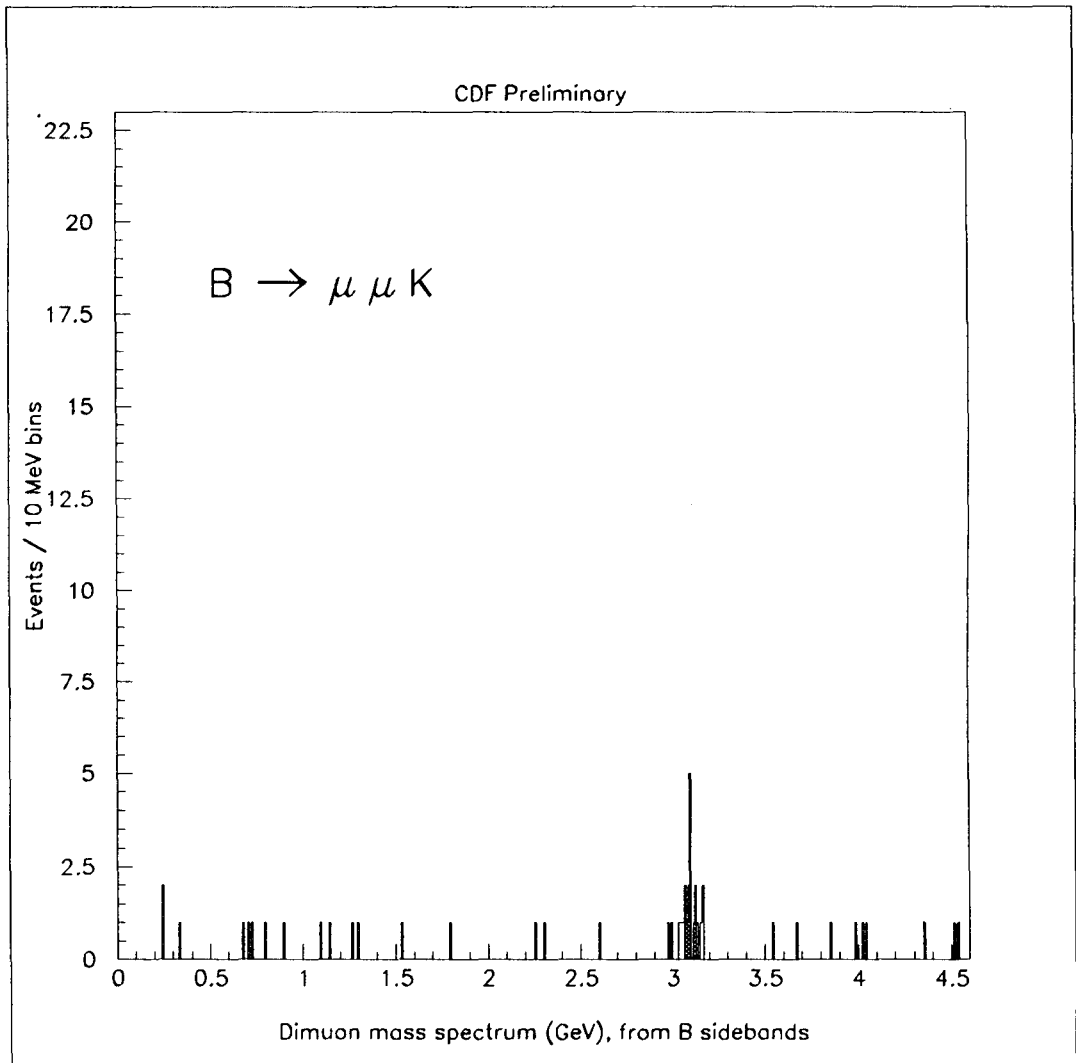Figure 7.11: Dimuon mass spectrum from B peak events.

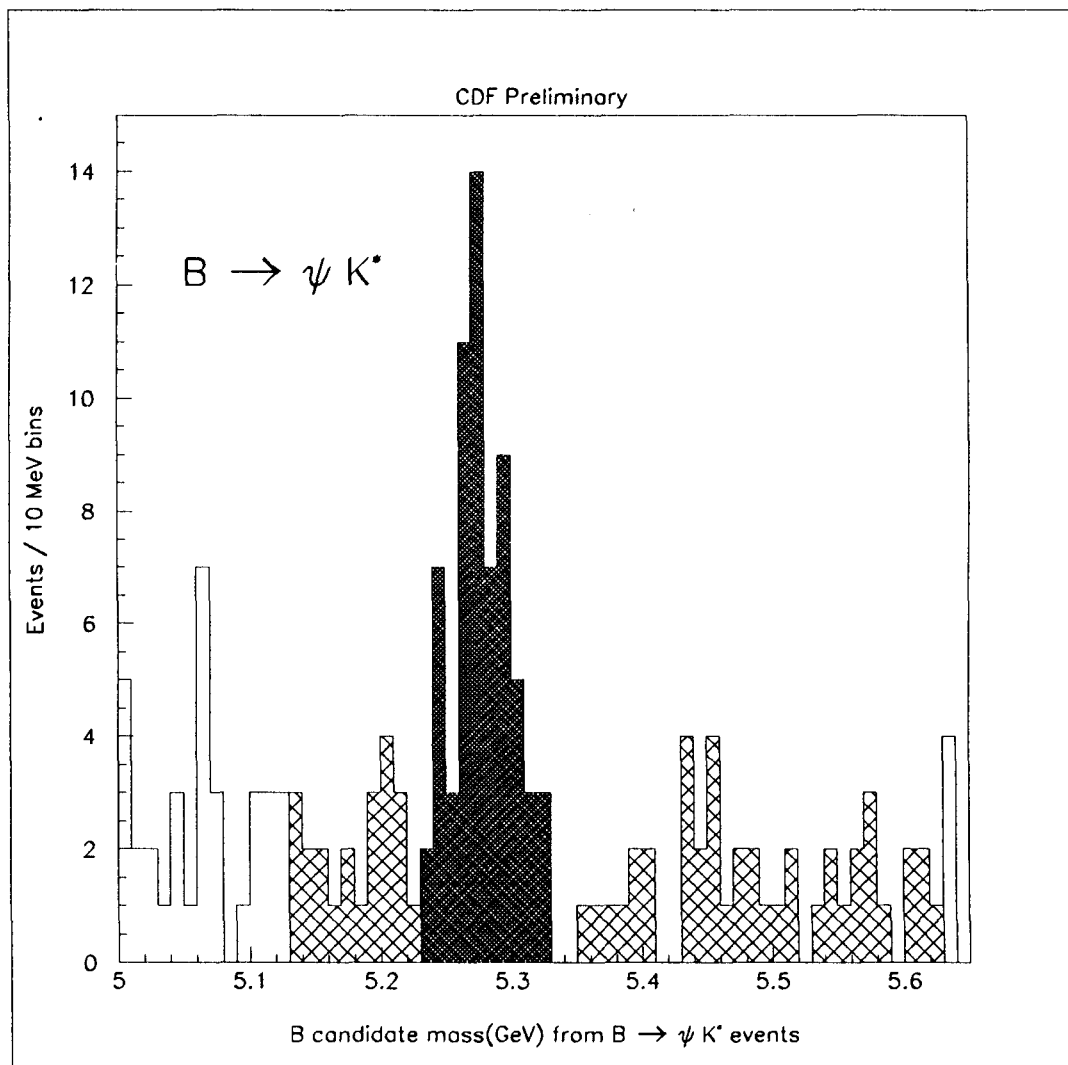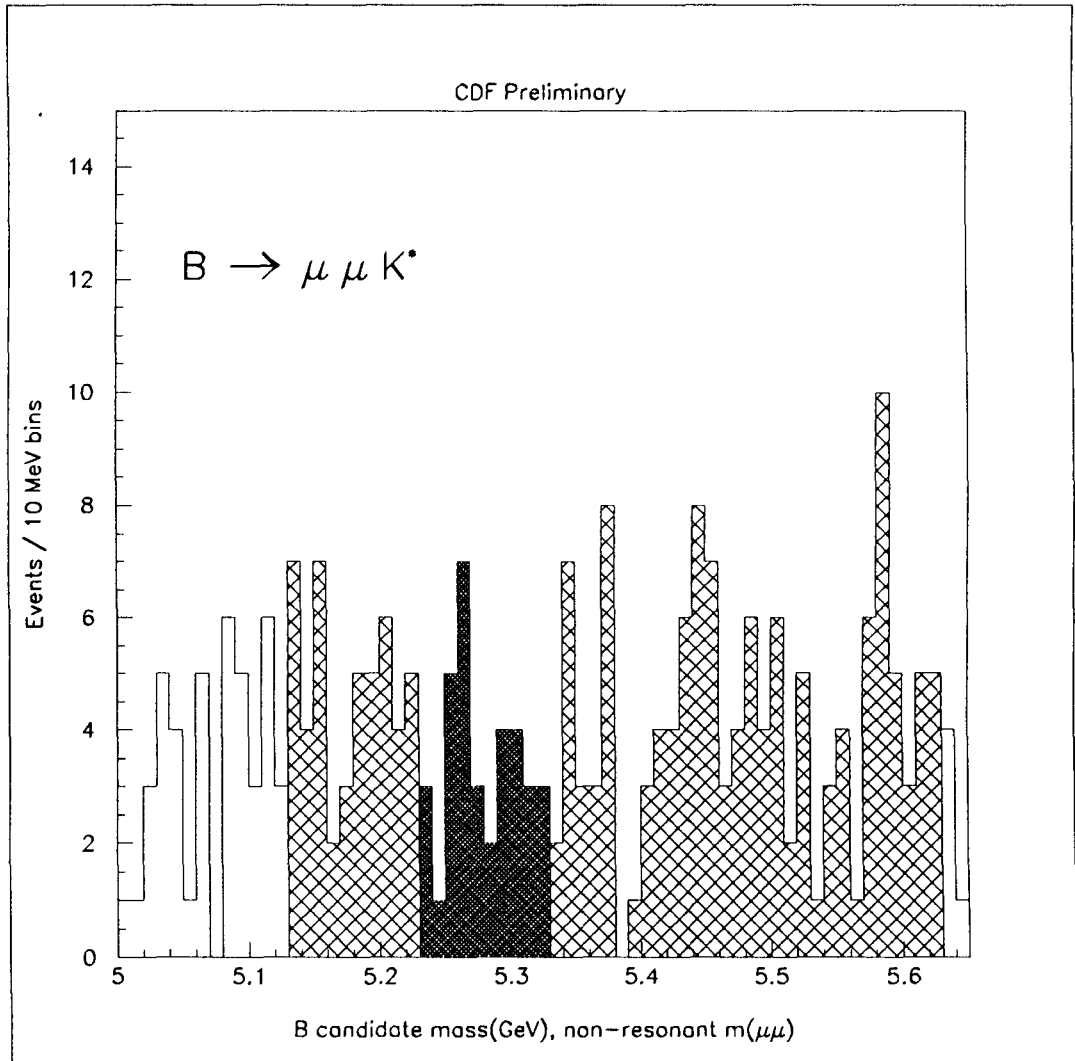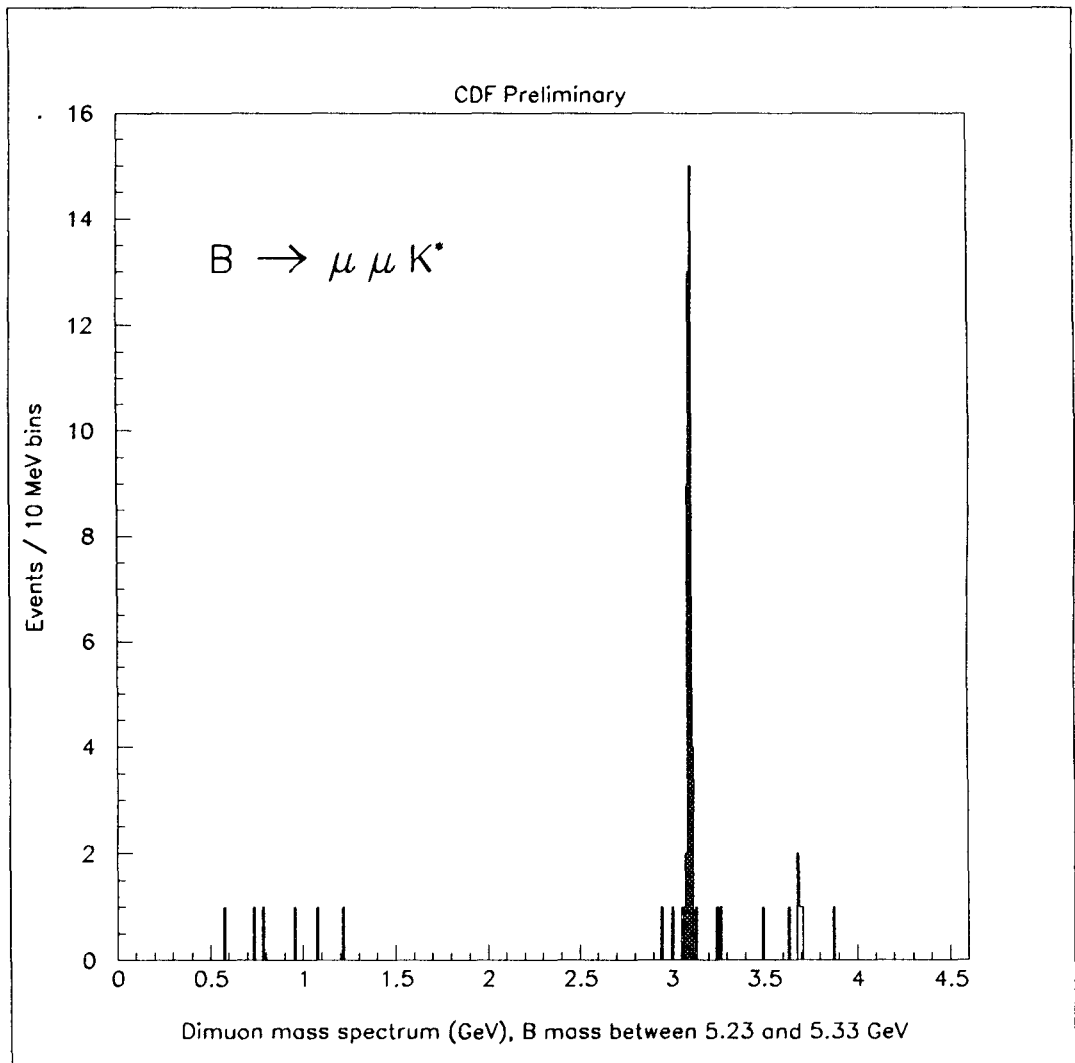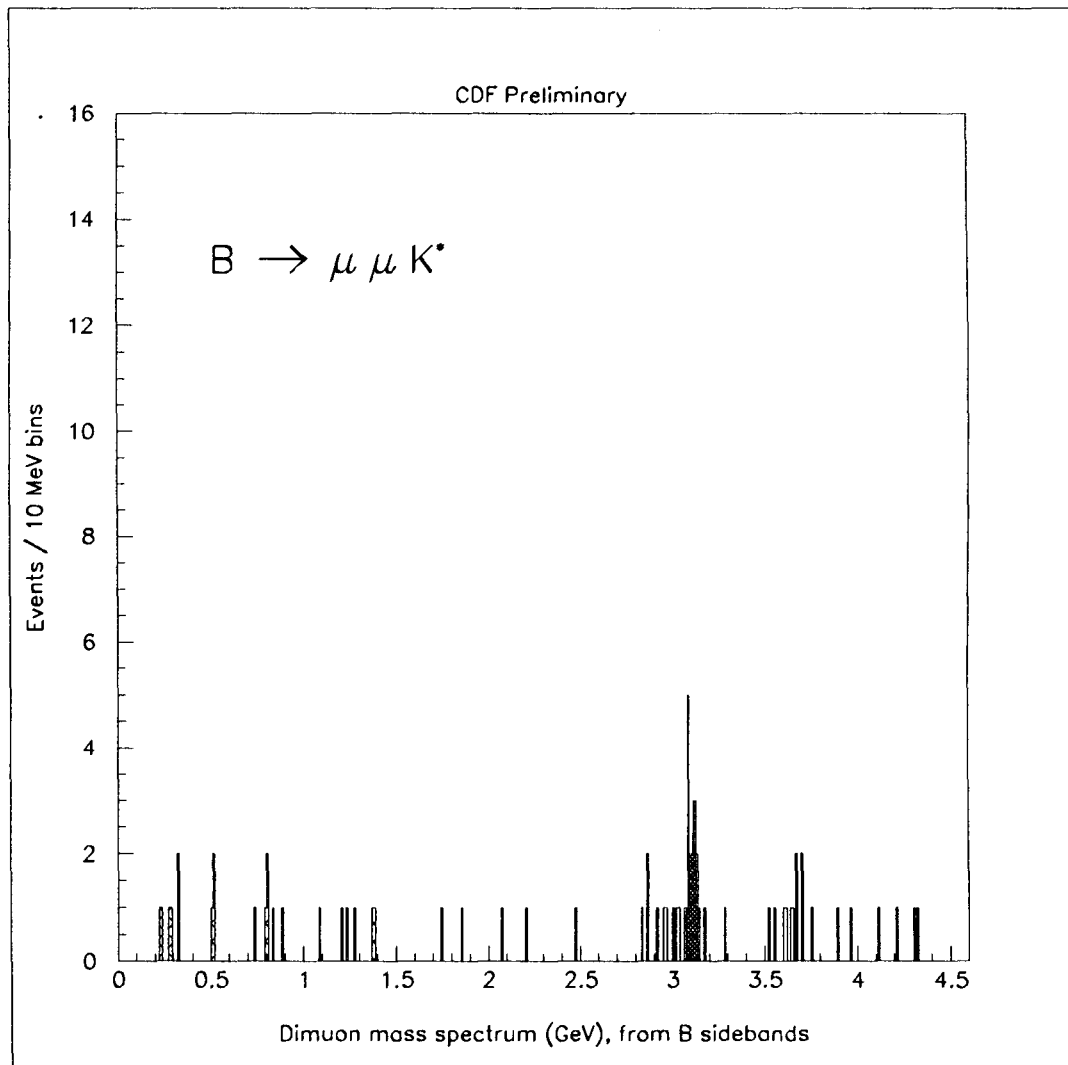Figure 7.12: Dimuon mass spectrum from B sideband events.

Chapter 8

Conclusions

These results are part of a growing body of information on flavor-changing neutral current decays. All decays of this type in the B system are characterized by loop order diagrams in which a b quark decays to leptons and possibly a lighter quark. These decays are a good measure for effects of proposed physics beyond the standard model since extensions (*e. g.* charged Higgs, fourth generation) inflate the expected branching ratios. That the decays aren't seen implies constraints on these models, so physicists developing new models calculate the rates the new models predict for the rare decays. If the rates are too high, the model is unacceptable. Work continues on theoretical calculations of standard model extensions [80].

There is a subtler sort of extension to the standard model that also inflates the expected branching ratios, but only slightly. If gauge boson couplings are not simple, then anomalous couplings increase the predicted rate of decays like these. Low experimental limits restrict the range of these couplings. With its

good muon detection and a considerable number of B's, CDF is competitive with the other major experiments on these limits. The major player in this field is CLEO, but the LEP experiments have begun to play a major role in the field. In the future, there are several B factories which will carry on the work, in addition to new data at CDF. The hunt for these decay modes is slow. This analysis is a sophisticated one; there aren't improvements to be had by finessing them out of the data. More than 100 times more data is required for an unambiguous signal.

8.1   Related decay modes

My measurements compliment those made at other facilities. Recent limits from CLEO II, including the first sighting of the penguin decay $B \rightarrow \gamma K^{*0}$ have inspired a number of papers on constraints to non-standard models. The limit presented here on $B \rightarrow \mu^+ \mu^- K^{*0}$ is more stringent than the 1989 UA1 limit as well as the 1994 CLEO limit.

Mode	Limit	Experiment
$B \to \gamma K^{*0}$	$2.32 \pm 0.67 \times 10^{-4}$	CLEO II [81]
$B \to e^+ e^-$	$< 5.9 \times 10^{-6}$	CLEO II [75]
$B \to e^+ e^- X_s$	$< 2.4 \times 10^{-3}$	CLEO [75]
$B \to e^+ e^- K^{\pm}$	$< 1.2 \times 10^{-5}$	CLEO II [55]
$B \to e^+ e^- K^{*0}$	$< 1.6 \times 10^{-5}$	CLEO II
$B \to \mu^+ \mu^-$	$< 2.0 \times 10^{-6}$	CDF 1A [82]
$B \to \mu^+ \mu^- X_s$	$< 5.0 \times 10^{-5}$	UA1 [49]
$B \to \mu^+ \mu^- K^{\pm}$	$< 0.9 \times 10^{-5}$	CLEO II
$B \to \mu^+ \mu^- K^{*0}$	$< 1.6 \times 10^{-5}$	CDF 1A

Table 8.1: Limits of various rare B decay modes.

8.2 Theoretical constraints

8.2.1 WWZ Vertex

Baillie [33] calculated rates for the decays $B \to \mu^+ \mu^- K^{\pm}$ and $B \to \mu^+ \mu^- K^{*0}$ for the case where there is an anomalous coupling between the W and Z bosons. In figure 3.4 the W in the loop couples to the Z or γ which in turn decays to a muon pair. If the coupling between the W and Z is different from the standard model (there is no reason why it shouldn't be) then there may be two additions to the effective Lagrangian for the decay. The standard model Feynman rule for a simple WWZ vertex, with the momentum defined as in figure 8.1 is

$$-ie \cot \theta_W [(k_+ - k_-)^\mu g^{\nu\lambda} + k_-^\lambda g^{\mu\lambda} - k_+^\lambda g^{\mu\nu}]$$

where k_- is the momentum of the W^-, and the function is evaluated in the Z center of mass frame. Baillie has calculated the Feynman rule for the anoma-

126

lous case and introduces two variables, g_1^Z and g_5^Z. In the standard model $g_1^Z = 1$ and $g_5^Z = 0$.

$$-ie \cot \theta_W \{\Delta g_1^Z [(k_+ - k_-)^\mu g^{\nu\lambda} + k_-^\lambda g^{\mu\lambda} - k_+^\lambda g^{\mu\nu}] + ig_5^Z \epsilon^{\nu\lambda\rho\mu}(k_- - K_+)_\rho\}$$

He calculated the ratio of branching ratios R and R^* as a function of these variables.

$$R^{(*)} = \frac{\Gamma(B \to \mu^+\mu^- K^{(*)}, non - res)}{\Gamma(B \to \mu^+\mu^- K^{(*)}, res)}$$

The resonant ψ region (res) runs from $m(\mu\mu) = 3.08$ to 3.12 GeV/c^2, and the non-resonant region $(non - res)$ runs from 3.12 to 3.66 and from 3.73 to 4.6 GeV/c^2. This ratio has the advantage of removing theoretical uncertainties. To compare my results to Baillie's, I re-calculate the limits on the branching ratios for a region similar to this one, $m(\mu\mu) = 2.8$ to 3.0, 3.3 to 3.6 and 3.8 to 4.6 GeV/c^2, and multiply by a correction factor.

$$R \quad < \quad 0.076 \times 0.938 = 0.71 \text{ at } 90\% \text{ CL}$$

$$R^* \quad < \quad 0.107 \times 1.042 = 0.11.$$

With these results, a look at figures 8.2 through 8.5 puts bounds on Δg_1^Z. These results put no meaningful bounds on Δg_5^Z. The strongest limits are from the decay $B \to \mu^+\mu^- K^\pm$.

$$-2.2 < \Delta g_1^Z < 2.0 \text{ at } 90\% \text{ CL.}$$

127

If there are anomalous couplings between the W and Z bosons, they occur with small enough values of Δg_1^Z that we don't see the decays.

The limits on g_1^Z are broader than those from other decay modes and experiments. Fuess [83] calculates the limit

$$-0.82 < \Delta g_1^Z < 1.00 \text{ at } 95\% \text{ CL}$$

directly from W and Z decays $WW, WZ \rightarrow l\nu jj, lljj$, where j indicates a jet and $\Lambda_{ff} = 1000$. There are no limits on g_5^Z from Fermilab at this time.

New limits from LEP by Dawson and Valencia [84] are

$$-0.08 < \Delta g_1^Z < 0.1 \text{ at } 90\% \text{ CL}.$$

The authors looked at rates of $Z \rightarrow \overline{f}f$, where they use measured exclusive rates, not using $Z \rightarrow \overline{b}b$. In the case of $Z \rightarrow \overline{b}b$, where $m_t = 175$ GeV/c^2, Éboli et al. [85] find

$$-0.32 < \Delta g_1^Z < -0.025 \text{ at } 90\% \text{ CL}$$
$$-1.9 < g_5^Z < -0.14.$$

In the standard model, these couplings are zero, not below zero. More accurate measurements on both couplings from CDF and other experiments would help confirm or deny these unusual deviations. It would be best to plot the couplings together, since there are cancellations between anomalous couplings if more

128

than one is present at a time. In addition, it would be interesting to study the couplings $\Delta\kappa_Z$ and λ_Z in the context of rare B decays.

In principle, rare B decays are sensitive to the $WW\gamma$ vertex inside the loop diagram (figure 3.4 as well as the WWZ vertex just discussed. The theoretical calculations are not available at present to make extraction of limits on these couplings feasible from rare B decays.

8.2.2 Charged Higgs

Several physicists are have calculate the effects of a charged Higgs extension to the standard model, as I mentioned in chapter 3. The charged Higgs bosons couple to the Z, γ and to quarks, so they would replace the W in figure 3.4. The predicted rate of the decay follows m_t/m_H and so decreases with m_H, as well as with $\tan^2\beta = v_2/v_1$. $v_1^2 + v_2^2 = v_{sm}^2$, where v_{sm} is the standard model vacuum expectation value, and v_1 and v_2 are the minimal extension to the standard model case. This ratio of vacuum expectation values characterizes the Higgs decay, but is an undetermined parameter in the theory. The goal is to constrain values of $\tan^2\beta$ with the low limits on the branching ratios.

The first step to transform the limits on $B \rightarrow \mu^+\mu^- K^\pm$ and $B \rightarrow \mu^+\mu^- K^{*0}$ into a limit on $\tan^2\beta$ is to extrapolate the results to a limit on $b \rightarrow \mu\mu s$. In the second column of the following table, the common factor of 10^{-6} has been left out. Here,

$$R = \frac{BR(B \rightarrow \mu^+\mu^- K^\pm + B \rightarrow \mu^+\mu^- K^{*0})}{BR(b \rightarrow \mu^+\mu^- s)}$$

Author	R
Bauer, Stech and Wirbel [41]	10 + 1.6 / 140 = 8.3 %
Dominguez, Paver and Riazuddin [41]	15 + 2.6 / 140 = 12.6 %
Jaus and Wyler [42]	5.0 + 3.0 / 140 = 16.0 %
Isgur and Wise I (Ali and Mannel) [47]	12 + 2.5 / 140 = 10.4 %
Isgur and Wise I (Ali and Mannel) [47]	10 + 1.1 / 140 = 7.9 %

The average value of R is 11%, so the limits from this thesis

$$BR(B \to \mu^+\mu^- K^\pm) \quad < \quad 1.1 \times 10^{-5}$$

$$BR(B \to \mu^+\mu^- K^{*0}) \quad < \quad 1.6 \times 10^{-5}$$

extrapolate to a limit of

$$BR(b \to \mu^+\mu^- s) < 2.4 \times 10^{-4}.$$

This is a weaker limit on the rate than the UA1 limit of

$$BR(b \to \mu^+\mu^- s) < 5.0 \times 10^{-5} \quad [49].$$

Figures 8.6 and 8.7 show the enhancements of the branching ratio as a function of $\tan\beta$ for two models, both evaluated at top quark mass of 150 GeV/c^2. Presumably the limits would be slightly stricter if the theoretical calculations had been performed using a top quark mass of 175 GeV/c^2. If the

Higgs is a charged pair, then it must have values of $\tan\beta$ is above the limits in the table.

Model I, limits on $\tan\beta$:

m_H (GeV)	CDF limit	UA1 limit
50	> 0.22	> 0.40
145	> 0.18	> 0.32
500	> 0.10	> 0.19

Model II, limits on $\tan\beta$:

m_H (GeV)	CDF limit	UA1 limit
50	> 0.20	> 0.34
145	> 0.16	> 0.24
500	-	> 0.14

8.2.3 Fourth Generation

If there were a fourth generation of quarks, then they would enter into the loop of the diagrams in figure 3.4, replacing the top quark as the dominant contributor to the rate. It would be nice to extract limits on the mass of such a particle, but there is a second unknown parameter, the mixing between the

fourth generation t' and the b and s quarks, $V_{t's}^* V_{t'b}$. Two groups of authors have computed decay rates for this extension to the standard model: Hou, Willey and Soni [22], and Deshpande and Trampetić [25]. Both these calculations are old. Hou, Willey and Soni assume the mass of the top quark to be 50 GeV/c^2, while Deshpande and Trampetić assume it is the same as the W mass, 80 GeV/c^2. Deshpande and Trampetić calculate an incomplete set of QCD corrections, correcting only for the photon diagrams. Therefore, the results which follow should be read with those caveats in mind.

Figure 8.9 uses $BR(B \to e^+e^- K^{(\pm, *)})$, so I change my muon results using Deshpande and Trampetić's results

$$\frac{\Gamma(B \to e^+e^- K^{*0})}{\Gamma(B \to \mu^+\mu^- K^{*0})} = 1.23$$

$$\frac{\Gamma(B \to e^+e^- K^{\pm})}{\Gamma(B \to \mu^+\mu^- K^{\pm})} = 1.00.$$

to obtain the limit $BR(B \to e^+e^- K^{*0}) < 1.3 \times 10^{-5}$. This, incidentally, is a better limit than the direct measurement of CLEO, albeit with some theoretical uncertainty in the calculation. See table 8.1

In addition, the results calculated in the previous section are useful. The limits extrapolate to $BR(b \to \mu^+\mu^- s) < 2.4 \times 10^{-4}$. Since this is a weaker limit on the rate than the UA1 limit of $BR(b \to \mu^+\mu^- s) < 5.0 \times 10^{-5}$ [49], I also include those results here. The K-M matrix element product is constrained to be closer to zero than the limits. If the fourth generation t' exists, it must mix only slightly with the other families or else it would be seen decaying.

Hou, Willey and Soni

$m_{t'}$ (GeV)	CDF limit	UA1 limit
150	-	$-0.2 < V_{t's}^* V_{t'b}$
200	-	$-0.12 < V_{t's}^* V_{t'b} < 0.18$
250	-	$-0.08 < V_{t's}^* V_{t'b} < 0.12$
300	$-0.18 < V_{t's}^* V_{t'b}$	$-0.06 < V_{t's}^* V_{t'b} < 0.09$
400	$-0.10 < V_{t's}^* V_{t'b} < 0.12$	$-0.02 < V_{t's}^* V_{t'b} < 0.05$
500	$-0.05 < V_{t's}^* V_{t'b} < 0.08$	$-0.01 < V_{t's}^* V_{t'b} < 0.04$

Deshpande and Trampetić (QCD corrected)

$m_{t'}$ (GeV)	CDF limit	UA1 limit
150	-	$-0.16 < V_{t's}^* V_{t'b} < 0.18$
250	$-0.18 < V_{t's}^* V_{t'b} < 0.20$	$-0.06 < V_{t's}^* V_{t'b} < 0.08$
500	$-0.06 < V_{t's}^* V_{t'b} < 0.06$	$-0.02 < V_{t's}^* V_{t'b} < 0.02$

Deshpande and Trampetić (QCD corrected, CDF limits)

$m_{l'}$ (GeV)	$B \to \mu^+ \mu^- K^{\pm}$ limit	$B \to \mu^+ \mu^- K^{*0}$ limit
150	-	-
250	$-0.17 < V_{t's}^* V_{t'b} < 0.20$	$-0.14 < V_{t's}^* V_{t'b} < 0.16$
500	$-0.05 < V_{t's}^* V_{t'b} < 0.05$	$-0.04 < V_{t's}^* V_{t'b} < 0.04$

8.3 Future Prospects

CDF will quadruple the number of B mesons available to do analyses like this one in the next year. Four more times the data (number of B's will go from 2×10^6 to 8×10^6) means the limits are likely to go down by a factor of two (limit goes down by the $\sqrt{N}$). The results are an order of magnitude away from evidence of the decays in the framework of the standard model, so there isn't much promise of discovery from CDF in the next few years.

CLEO continues to run $e^+ e^-$ collisions for competitive results (3×10^7 B pairs per year). Still, there isn't much hope of seeing these decay channels until some of the new experiments come on line. Procario predicts [86] that the new B factories, BaBar, Belle (KEK) and Hera B, won't be able to produce the number of B's needed before the year 2000, but that after that time there should be enough statistics accumulated to look for rare B decays. The LHC is our greatest hope for a large number of B's. Even that machine will need to push p_t thresholds on B physics high to avoid saturating the trigger with

B physics when they want to study top quark physics. Fortunately, the CMS detector is designed so that the uncertainty on the measurement of the vertex position in x, y, z should be 15 microns [87]. This is better than the precision of CDF's vertex resolution, which lends support to doing a similar analysis at LHC.

This topic promises to be a lively one for the next few decades. It is unfortunate that it will take so long to find the decay as the standard model predicts it. It is always possible, however, that non-standard model physics will cause the rate to be higher and precipitate discovery sooner than we think.
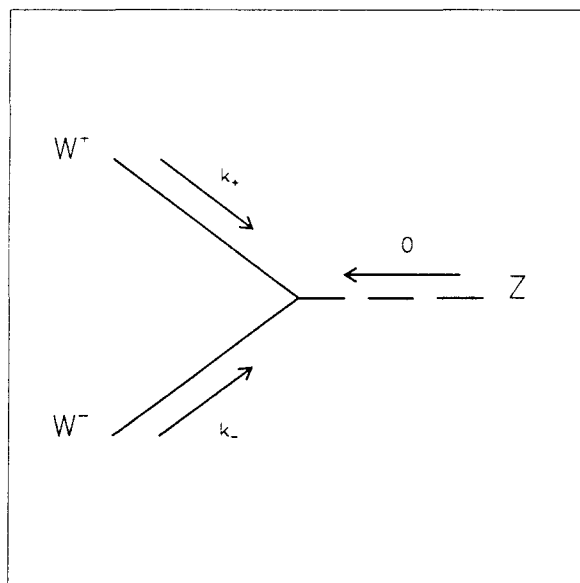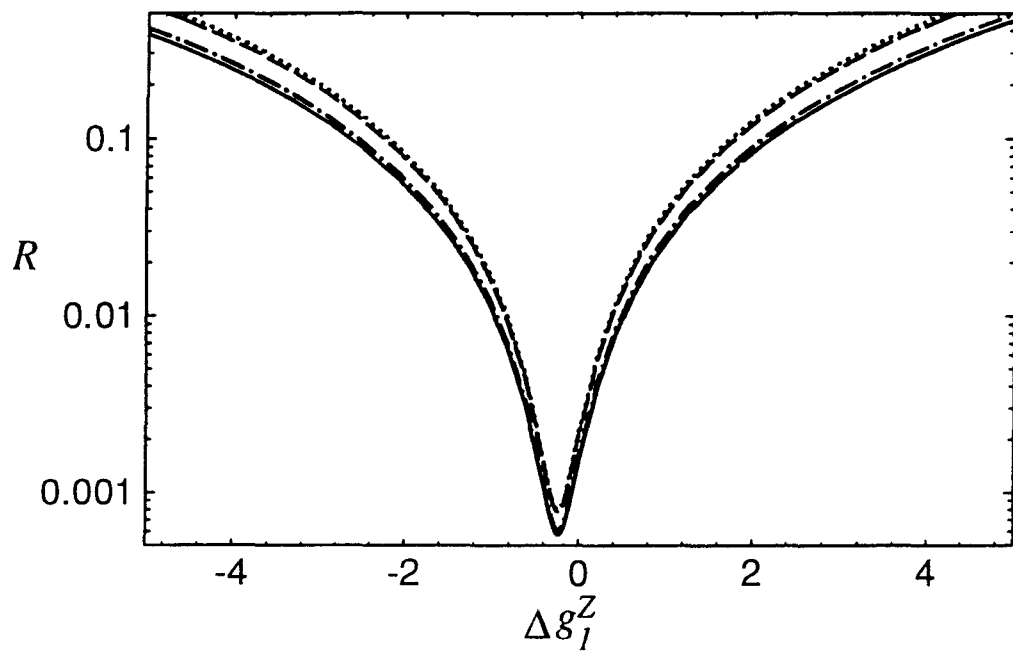

Figure 8.1: WWZ vertex.

Figure 8.2: Plot of the quantity R versus Δg_1^Z for various parameterizations of the Isgur-Wise function.
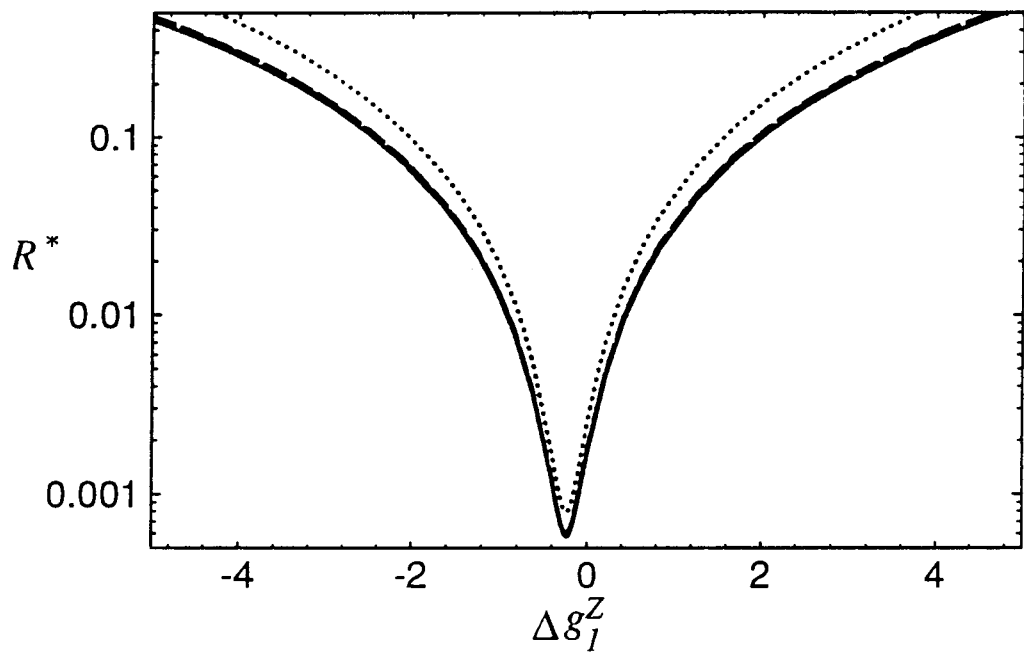
Figure 8.3: Plot of the quantity R^* versus Δg_1^Z for various parameterizations of the Isgur-Wise function.

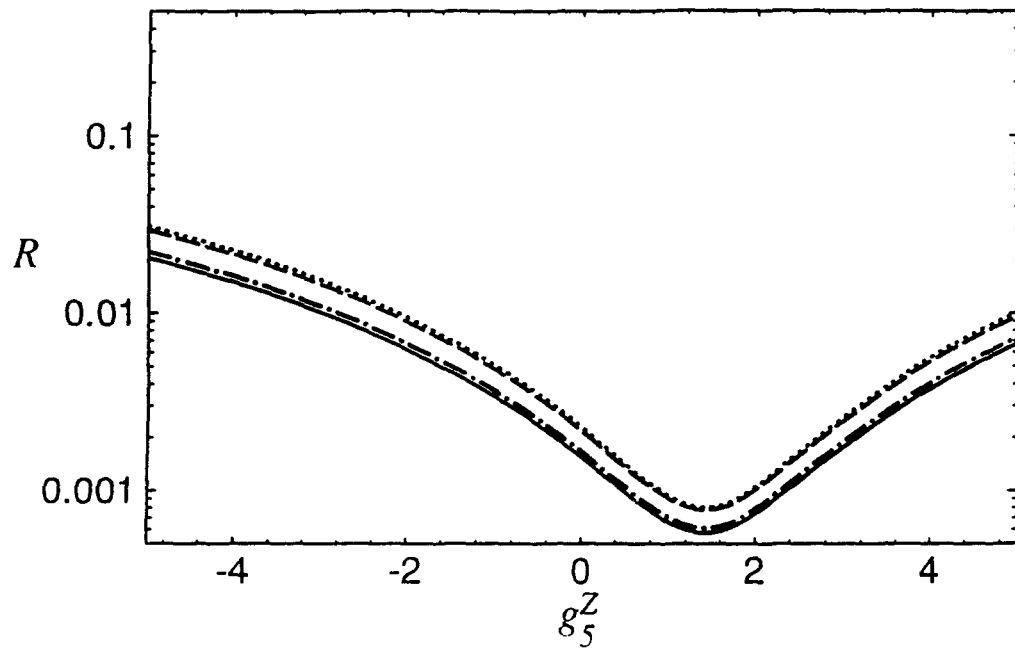Figure 8.4: Plot of the quantity R versus g_5^Z for various parameterizations of the Isgur-Wise function.
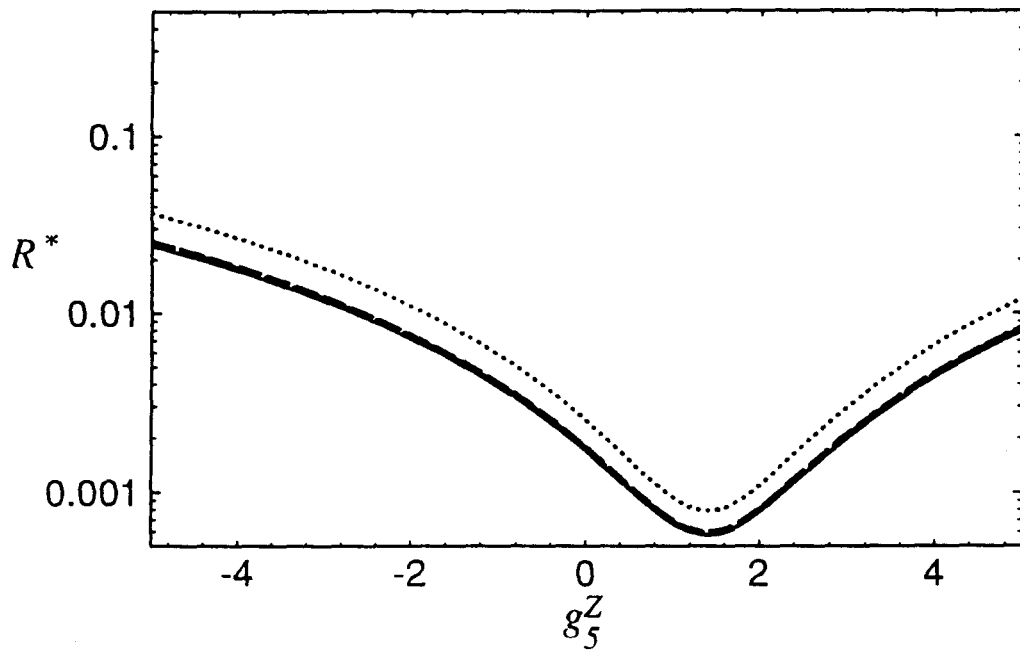
Figure 8.5: Plot of the quantity R^* versus g_5^Z for various parameterizations of the Isgur-Wise function.
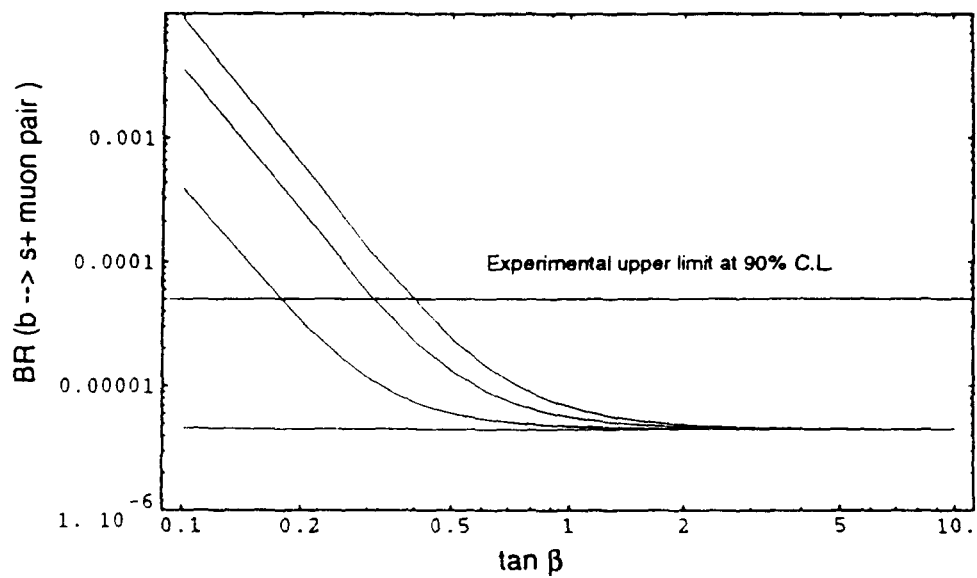
Figure 8.6: Branching ratios of $b \to \mu^+ \mu^- s$ as a function of $\tan \beta$ in Model I, for Higgs mass of 50, 145 and 500 GeV respectively from the top of the figure. Mass of the top quark is assumed to be 150 GeV.

Figure 8.7: Branching ratios of $b \to \mu^+\mu^- s$ as a function of $\tan\beta$ in Model II, for Higgs mass of 50, 145 and 500 GeV respectively from the top of the figure. Mass of the top quark is assumed to be 150 GeV.
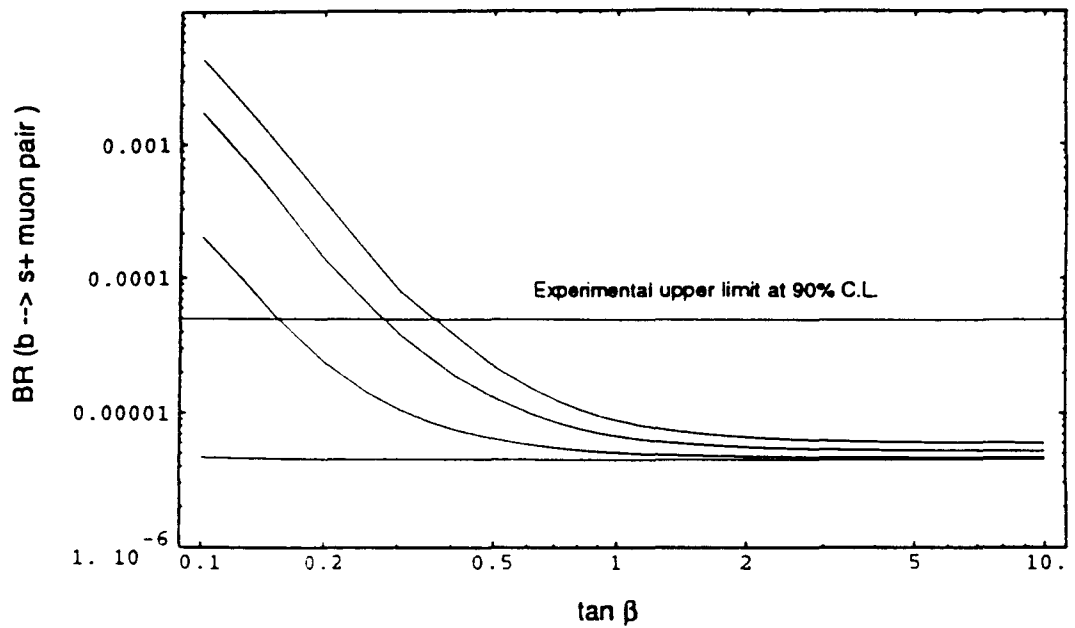
Figure 8.8: Branching ratios of $b \rightarrow \mu^+\mu^- s$ as a function of K-M mixing $V_{t's}^* V_{t'b}$, for t' masses of 150, 200, 250, 300, 400 and 500 GeV/c^2, respectively from the bottom of the figure. Mass of the top quark is assumed to be 50 GeV/c^2.
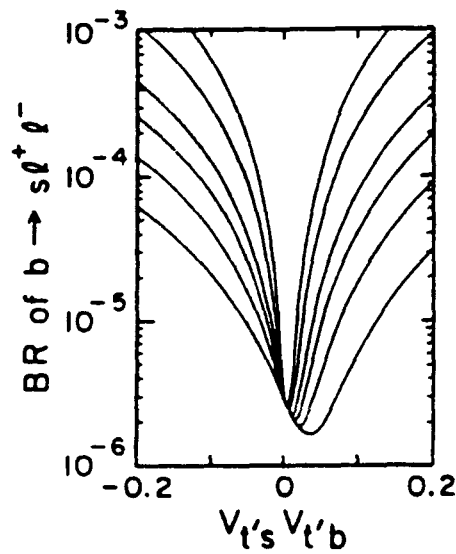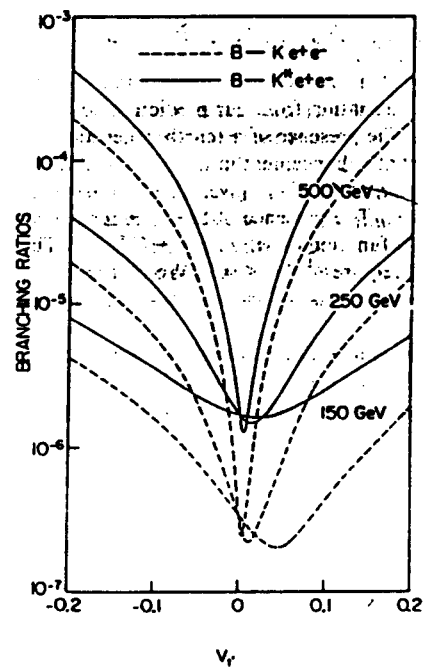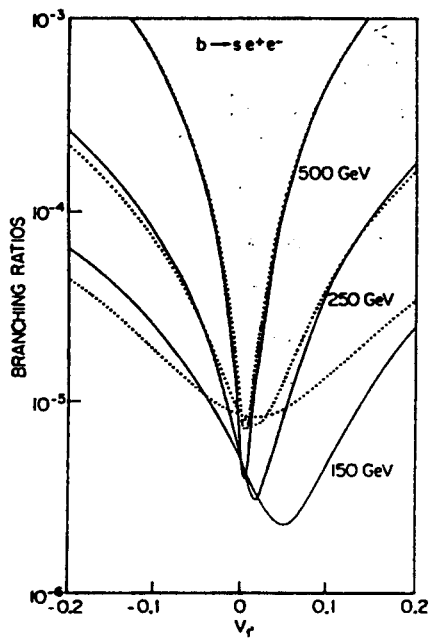
Figure 8.9: Branching ratios of $b \to \mu^+\mu^- s$ as a function of K-M mixing $V_{t's}^* V_{t'b}$, for t' masses of 150, 250 and 500 GeV/c^2, respectively from the bottom of the figure. Mass of the top quark is assumed to be 80 GeV/c^2.

Bibliography

[1] H. Wenzel. Fitting the beam position with the SVX. Technical Report CDF/ANAL/SEC_VTX/CDFR/1924, Fermilab, (1993).

[2] G. Ascoli *et al.*, The CDF Collaboration. A leveling system for the CDF central muon chambers. *Nucl. Instr. Meth.*, A 268:41–45, (1988).

[3] F. DeJongh and R. Hans. Level 1 and Level 2 low p_t central muon trigger efficiencies for run 1A. Technical Report CDF/ANAL/TRIGGER/-CDFR/1999, CDF Note, (1993).

[4] K. Kleinknecht. *Detectors for Particle Radiation.* Cambridge University Press, The Pitt Building, Trumpington Street, Cambridge CB2 1RP, (1986).

[5] D. Griffiths. *Introduction to Elementary Particles.* Harper & Row Publishers, Inc., 10 East 53rd Street, New York, NY 10022-5299, (1987).

[6] T. Inami and C. S. Lim. Effects of superheavy quarks and leptons in low-energy weak processes $K_L \rightarrow \mu\bar{\mu}, K^+ \rightarrow \pi^+\nu\bar{\nu}$ and $K^0 \leftrightarrow \overline{K^0}$. *Progress of Theoretical Physics*, 65:297–314, (1981). Errata, p 1772, same volume.

[7] S. W. Herb *et al.* Observation of a dimuon resonance at 9.5 GeV in 400-GeV proton-nucleus collision. *Phys. Rev. Lett.*, 39:252–255, (1977).

[8] S. Behrends *et al.* Observation of exclusive decay modes of b-flavored mesons. *Phys. Rev. Lett.*, 50:881–884, (1983).

[9] G. L. Kane and M. E. Peskin. A constraint from B decay on models with no t quark. *Nucl. Phys.*, B 195:29–38, (1982).

[10] B. A. Campbell and P. J. O'Donnell. Mass of the top quark and induced decay and mixing of neutral B mesons. *Phys. Rev. D*, 25:1989–1992, (1982).

144

[11] S. L. Glashow, J. Iliopoulos, and L. Maiani. Weak interactions with lepton-hadron symmetry. *Phys. Rev. D*, 2:1285–1292, (1970).

[12] B. Grządkowski and P. Krawczyk. Higgs particle effects in flavour changing transitions. *Z. Phys. C*, 18:43–45, (1983).

[13] A. Chen *et al.*, the CLEO Collaboration. Ruling out exotic models of b quark decay. *Phys. Lett.*, 122 B:317–321, (1983).

[14] B. Adeva *et al.*, the CLEO Collaboration. Search for top quark and a test of models without top quark up to 38.54 GeV at PETRA. *Phys. Rev. Lett.*, 50:799–802, (1983).

[15] W. Bartel *et al.*, the CLEO Collaboration. A search for flavour-changing neutral currents in b decay at PETRA. *Phys. Lett.*, 132 B:241–245, (1983).

[16] P. Avery *et al.*, the CLEO Collaboration. Upper limit on flavor-changing neutral-current decays of the b quark. *Phys. Rev. Lett.*, 53:1309–1313, (1984).

[17] P. J. O'Donnell. Rare decays of the B meson. *Phys. Lett. B*, 175:369–372, (1986).

[18] N. G. Deshpande, G. Eilam, A. Soni and G. L. Kane. $B \rightarrow Kl^+l^-$ and other rare B-meson decays. *Phys. Rev. Lett.*, 57:1106–1109, (1986).

[19] G. Eilam, J. L. Hewett and T. G. Rizzo. $B \rightarrow Kl^+l^-$ with four generations: Rates and CP violation. *Phys. Rev. D*, 34:2773–2777, (1986).

[20] P. Avery *et al.*, The CLEO Collaboration. Limits on rare exclusive decays of B mesons. *Phys. Lett. B*, 183:429–433, (1987).

[21] A. Bean *et al.*, the CLEO Collaboration. Improved upper limit on flavor-changing neutral-current decays of the b quark. *Phys. Rev. D*, 35:3533–3536, (1987).

[22] W.-S. Hou, R. S. Willey and A. Soni. Implications of a heavy top quark and a fourth generation on the decays $B \rightarrow Kl^+l^-, K\nu\bar{\nu}$. *Phys. Rev. Lett.*, 58:1608–1611, (1987).

[23] W.-S. Hou and R. S. Willey. Effects of the Charged Higgs Bosons on the Processes $b \rightarrow s\gamma$, $b \rightarrow sg^*$ and $b \rightarrow sl^+l^-$. *Phys. Lett. B*, 202:591–595, (1988).

[24] W. -S. Hou and R. S. Willey. Effects of extended Higgs sector on loop-induced B decays. *Nucl. Phys. B*, 326:54–72, (1989).

[25] N. G. Deshpande and J. Trampetić. Improved estimates for processes $b \rightarrow s l^+ l^-, B \rightarrow K l^+ l^-$, and $B \rightarrow K^* l^+ l^-$. *Phys. Rev. Lett.*, 60:2583–2586, (1988).

[26] N. G. Deshpande, P. Lo, J. Trampetić, G. Eilam and P. Singer. Prediction of $B \rightarrow K^* \gamma$ as a test of the standard model. *Phys. Rev. Lett.*, 59:183–185, (1987).

[27] M. Bauer, B. Stech and M. Wirbel. Exclusive non-leptonic decays of D^-, D_s^- and B-mesons. *Z. Phys. C*, 34:103–115, (1987).

[28] B. Grinstein, M. B. Wise and N. Isgur. Weak mixing angles from semileptonic decays in the quark model. *Phys. Rev. Lett.*, 56:298–301, (1986).

[29] B. Grinstein, M. J. Savage and M. B. Wise. $B \rightarrow X_s e^+ e^-$ in the six-quark model. *Nucl. Phys. B*, 319:271–290, (1989).

[30] R. Grigjanis, P. J. O'Donnell, M. Sutherland and H. Navelet. QCD radiative corrections to $B \rightarrow X_s e^+ e^-$ processes. *Phys. Lett. B*, 223:239–244, (1989).

[31] R. Grigjanis, P. J. O'Donnell, M. Sutherland and H. Navelet. QCD radiative corrections to charmless B decays. *Phys. Lett. B*, 224:209–212, (1989).

[32] C. S. Lim, T. Morozumi and A. I. Sanda. A prediction for $d\Gamma(b \rightarrow s l \bar{l})/dq^2$ including the long-distance effects. *Phys. Lett. B*, 218:343–347, (1989).

[33] G. Baillie. $b \rightarrow s \mu^+ \mu^-$ decays at hadron colliders. *Z. Phys. C*, 61:667–674, (1994). Also UCLA/93/TEP/26, e-print archive: hep-ph 9307369.

[34] A. I. Vainshtein, V. I. Zakharov, L. B. Okun and M. A. Shifman. On the $K^+ \rightarrow \pi^+ e^+ e^-$ decay. *Sov. J. Nucl. Phys.*, 24:427–451, (1976). (ITEP-98-1975).

[35] N. G. Deshpande, J. Trampetić and K. Panose. Resonance background to the decays $b \rightarrow s l^+ l^-$, $B \rightarrow K^* l^+ l^-$, and $B \rightarrow K l^+ l^-$. *Phys. Rev. D*, 39:1461–1463, (1989).

[36] P. J. O'Donnell and H. K. K. Tung. Resonance contributions to the decay $b \rightarrow s l^+ l^-$. *Phys. Rev. D*, 43:R2067–R2069, (1991).

[37] A. Ali, T. Mannel and T. Morozumi. Forward-backward asymmetry of dilepton angular distribution in the decay $b \to sl^+l^-$. *Phys. Lett. B*, 273:505–512, (1991).

[38] P. Avery *et al.*, the CLEO Collaboration. A search for exclusive penguin decays of B mesons. *Phys. Lett. B*, 223:470–475, (1989).

[39] A. J. Weir *et al.*, The Mark II Collaboration. Upper limits on $D^\pm$ and $B^\pm$ decays to two leptons plus $\pi^\pm$ or $K^{\pm*}$. *SLAC-PUB-4999*, (1989). Submitted to Phys. Rev. D.

[40] H. Albrecht *et al.*, The ARGUS Collaboration. Search for $b \to sX^+X^-$ in exclusive decays of B mesons. *ISSN 0418-9833*, DESY 89-166, (1989).

[41] C. A. Dominguez, N. Paver and Riazuddin. Exclusive $b \to s$ rare decays of beauty. *Z. Phys. C.*, 48:55–63, (1990).

[42] W. Jaus and D. Wyler. Rare decays $B \to K l\bar{l}$ and $B \to K^* l\bar{l}$. *Phys. Rev. D*, 41:3405–3413, (1990).

[43] W. Jaus. Semileptonic decays of B and D mesons in the light-front formalism. *Phys. Rev. D*, 41:3394–3404, (1990).

[44] N. Isgur and M. B. Wise. Weak decays of heavy mesons in the static quark approximation. *Phys. Lett. B*, 232:113–117, (1989).

[45] N. Isgur and M. B. Wise. Weak transition form factors between heavy mesons. *Phys. Lett. B*, 237:527–530, (1990).

[46] N. Isgur and M. B. Wise. Relationship between form factors in semileptonic $\overline{B}$ and D decays and exclusive rare $\overline{B}$-meson decays. Technical Report UTPT-90-02, CALT-68-1625, Department of Physics, University of Toronto, Canada; and California Institute of Technology, Pasadena, California, USA, (1990).

[47] A. Ali and T. Mannel. Exclusive rare B-decays in the heavy quark limit. *Phys. Lett. B*, 264:447–454, (1991). Erratum, Phys. Lett. B 274:526 (1992).

[48] B. Baillie. Private communication.

[49] C. Albajar *et al.*, The UA1 Collaboration. A search for rare B meson decays at the CERN $Sp\bar{p}S$ collider. *Phys. Lett. B*, 262:163–170, (1991).

[50] K. Ankoviak. *A Search for Rare Beauty Meson Decays at the CERN Sp$\bar{p}$S Collider.* PhD thesis, University of California, Los Angeles, (1991).

[51] M. Sher and Y. Yuan. Rare B decays, rare τ decays and grand unification. *Phys. Rev. D*, 44:1461–1472, (1991).

[52] N. G. Deshpande, K. Panose and J. Trampetić. The decay $b \rightarrow sl^+l^-$ and the enlarged Higgs sector. *Phys. Lett. B*, 308:322–326, (1993).

[53] M. B. Çakir. Angular distribution and helicity dependence in $B \rightarrow K^{(*)}l^+l^-$. *Phys. Rev. D*, 46:2961, (1992).

[54] M. Gourdin. Polarization effects in the decay $B \rightarrow \mu^+\mu^-K^\pm$. *Phys. Lett. B*, 316:578–582, (1993).

[55] Balest *et al.*, CLEO Collaboration. Search for $B \rightarrow Kl^+l^-$ and $B \rightarrow K^*l^+l^-$ decays. Technical Report CLEO CONF 94-4, CLEO Report, (1994). ICHEP94 Ref. GSL0389.

[56] P. Nason, S. Dawson and R. K. Ellis. The one particle inclusive differential cross section for heavy quark production in hadronic collisions. *Nucl. Phys.*, B 327:49–92, (1989).

[57] C. Peterson *et al.* Scaling violations in inclusive e^+e^- annihilation spectra. *Phys. Rev. D*, 27:105, (1983).

[58] R. Hughes *et al.* A Monte Carlo for studying B meson production and decay. Technical Report CDF/ANAL/HEAVY_FLAVOR/GROUP/1626, Fermilab, (1991).

[59] F. Abe *et al.*, The CDF Collaboration. The CDF detector: An overview. *Nucl. Instr. Meth.*, A 271:387–403, (1988). and references therein.

[60] B. Barnett *et al.*, The CDF Collaboration. Progress in the construction of the CDF silicon vertex detector. *Nucl. Inst. and Meth.*, A315:125, (1992).

[61] B. T. Huffman. Private communication.

[62] F. Bedeschi *et al.*. the CDF Collaboration. Design and construction of the CDF central tracking chamber. *Nucl. Instr. Meth.*, A 268:50–74, (1988).

[63] L. Balka *et al.*, The CDF Collaboration. The CDF central electromagnetic calorimeter. *Nucl. Instr. Meth.*, A 267:272–279, (1988).

[64] S. Bertolucci *et al.*, The CDF Collaboration. The CDF central and end-wall hadron calorimeter. *Nucl. Instr. Meth.*, A 267:301–314, (1988).

[65] Y. Fukui *et al.*, The CDF Collaboration. CDF end plug electromagnetic calorimeter using conductive plastic proportional tubes. *Nucl. Instr. Meth.*, A 267:280–300, (1988).

[66] G. Brandenburg *et al.*, The CDF Collaboration. An electromagnetic calorimeter for the small angle regions of the collider detector at fermilab. *Nucl. Instr. Meth.*, A 267:257–271, (1988).

[67] S. Cihangir *et al.*, The CDF Collaboration. The CDF forward/backward hadron calorimeter. *Nucl. Instr. Meth.*, A267:249–256, (1988).

[68] G. Ascoli *et al.*, The CDF Collaboration. CDF central muon detector. *Nucl. Instr. Meth.*, A 268:33–40, (1988).

[69] K. Byrum *et al.*, The CDF Collaboration. The CDF forward muon system. *Nucl. Instr. Meth.*, A 268:46–49, (1988).

[70] D. Amidei *et al.*, The CDF Collaboration. A two level fastbus based trigger system for CDF. *Nucl. Instr. Meth.*, A 269:51–62, (1999).

[71] G. Ascoli *et al.*, The CDF Collaboration. CDF central muon Level-1 trigger electronics. *Nucl. Instr. Meth.*, A 269:63–67, (1988).

[72] G. Foster *et al.*, The CDF Collaboration. A fast hardward track-finder for the CDF central tracking chamber. *Nucl. Instr. Meth.*, A 269:93–100, (1988).

[73] P. Derwent, C. Grosso-Pilcher, S. Belforte and J. Marriner. Sigma_BBC updates. Technical Report CDF/PHYS/CDF/CDFR/2535, Fermilab, (1994). See also CDF note number 2361.

[74] Browder, K. Honscheid and S. Playfer. Rare B decays. Technical Report 93/1261, CLNS, (1994).

[75] Particle Data Group. Review of particle properties. *Phys. Rev. D*, 50, (1994).

[76] F. Abe *et al.*, The CDF Collaboration. Measurement of the B^+ and B^0 meson lifetimes. *Phys. Rev. Lett.*, (1994).

149

[77] C. Anway-Wiese. Calculating branching ratio limits when comparing related decay modes. Technical Report CDF/ANAL/BOTTOM/CDFR/-2496, Fermilab, (1994).

[78] O. Helene. Upper limit of peak area. *Nucl. Inst. and Meth.*, 212:319–322, (1982).

[79] G. Zech. Upper limits in experiments with backgound or measurement errors. *Nucl. Instr. Meth.*, A 277:608, (1989).

[80] G. Burdman. Testing the standard model in $B \rightarrow K^{(*)}l^+l^-$. Technical Report FERMILAB-Pub-95/113-T, Fermilab, (1995).

[81] Barish *et al.*, CLEO Collaboration. First measurement of the inclusive rate for the radiative penguin decay $b \rightarrow s\gamma$. Technical Report CLEO CONF 94-1, CLEO Report, (1994). ICHEP94 Ref. GSL0392.

[82] Abe *et al.*, The CDF Collaboration. Search for rare B decays at CDF. *Submitted to Phys. Rev. Lett.*, (1995).

[83] T. Fuess. WW and WZ production at the Tevatron. In *International Symposium on Vector Boson Self-Interactions*, (1995).

[84] S. Dawson and G. Valencia. Bounds on anomalous gauge boson couplings from partial Z widths at LEP. *Nucl. Phys. B*, 439:3–22, (1995).

[85] O. J. P. Éboli, S. M. Lietti, M. C. Gonzalez-Garcia, S. F. Novaes. ϵ_b constraints on self-couplings of vector bosons. *Phys. Lett. B*, 339:119–126, (1994).

[86] M. Procario. B physics prospects beyond 2000. In *Pbarp Workshop, FNAL*, (1995).

[87] T. Muller. Physics prospects with CMS at the LHC. In *Pbarp Workshop, FNAL*, (1995).